APPLICATION OF COMPUTATIONAL FLUID DYNAMICS TO INDOOR ROOM AIRFLOW

By

MICHAEL RAMEY

Bachelor of Science

Oklahoma Christian University of Science and Arts

Oklahoma City, Oklahoma

1991

Submitted to the Faculty of the
Graduate College of the
Oklahoma State University
in partial fulfillment of
the requirements for
the Degree of
MASTER OF SCIENCE
December, 1994

APPLICATION OF COMPUTATIONAL FLUID DYNAMICS

TO INDOOR ROOM AIRFLOW

Thesis Approved:

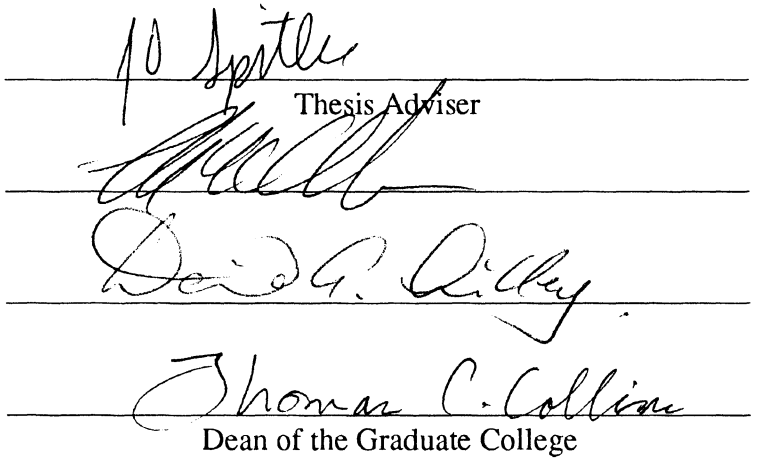

Thesis Adviser

Dean of the Graduate College

ACKNOWLEDGMENTS

I wish to thank my advisor, Dr. Jeff Spitler, for his supervision and guidance. My sincere appreciation also extends to the other members of my committee, Dr. Chambers and Dr. Lilley. Their comments were important to this project, and I am thankful for their help.

I am grateful to Jim Weathers for his insight and advice on this project.

I would like to thank my father, mother, sister and entire family for their continued support and encouragement. My completion of this degree is a success for them as much as it is for me.

Thank you to many other friends, classmates, and professors who have encouraged me along the way and provided helpful advice.

I would especially like to thank my wife, Lisa, for her encouragement at times of difficulty, and for her love and patience over the past few years. Her support has been invaluable, and I will be eternally grateful.

TABLE OF CONTENTS

LIST OF TABLES

LIST OF FIGURES

NOMENCLATURE

A_{in}	Area of Inlet
A_{out}	Area of Outlet
ACH	Air Changes Per Hour
C_1, C_2, C_μ	Constant Coefficients in k-ε Model
C_p	Specific Heat
D	Mass Divergence
E_{abs}	Absolute Error
F_1, F_2, F_μ, E	Empirical Functions in k-ε Model
g	Gravity
GEN	Global Error Number
H	Room Height
h_c	Convection Coefficient
I_u^2	Turbulence Intensity of the X-Velocity
J	Jet Momentum Number
k	Turbulent Kinetic Energy
kin	Turbulent Kinetic Energy at Inlet
P	Pressure
q''_c	Convective Heat Flux
R_y	Local Reynolds number
R_T	Turbulent Reynolds number
T	Temperature

T_O, T_r	Reference Temperatures
T_S	Surface Temperature
t	Time
U, V, W	Velocity Components in X, Y, & Z Directions
$\overline{U}$	Mean Velocity Component
U_{in}	Inlet Velocity
U_{out}	Outlet Velocity
U_n	Normal Velocity
U_t	Tangential Velocity
u'	Turbulent Velocity Fluctuation

α	Thermal Diffusivity
$\overline{\alpha}$	Donor Cell Coefficient
β	Thermal Expansion Coefficient
$\overline{\beta}$	Pressure Divisor
Δx_i, Δy_j, Δz_k	Distance Between Scalar Quantities
Δxc_i, Δyc_j, Δzc_k	Width of MAC Cells
Δt	Time Step
δ_{ij}	Kronecker Delta
ε	Turbulent Energy Dissipation Rate
ε_{in}	Turbulent Energy Dissipation Rate at Inlet
Γ_x, Γ_y, Γ_z	Turbulent Functions
Π	Turbulent Term in k and ε Equations

Θ	Turbulent Function in k and ε Equations
ρ	Density
μ	Dynamic Viscosity
ν	Kinematic Viscosity
ν_t	Turbulent Viscosity

1.0 INTRODUCTION

1.1 Overview

The simulation of room air flow has the potential to improve thermal comfort, indoor air quality, and the design of heating, ventilating, and air-conditioning systems. Information concerning the thermal condition of a room is helpful to the designer of a heating or cooling system, and can be provided by a computational analysis of air velocity and temperature in a room. Specific thermal information such as convection coefficients and temperatures throughout the model, especially at the outlet, are helpful to experimental researchers and designers. This thesis explores the possibility of predicting room surface convection coefficients and temperatures throughout the domain by using various temperature wall boundary conditions in a three dimensional, transient, turbulent, buoyant, computational fluid dynamics program.

Other goals of this project are to improve upon the previous modeling efforts through utilization of a variable grid model and improve confidence in the results by using transient visualization tools in the post-processing stages of analysis.

1.2 Literature Review

Airflow modeling and its application have progressed significantly in many areas within the last twenty years. Many researchers have contributed to the specific application of room airflow modeling, while a great many more have developed turbulent two equation models for analyzing a specific type of fluid flow such as boundary layer flow, channel flow, etc. This section will cover computational room airflow research and the development of the k-ε model. The literature review is organized by author.

Because of the extensive amount of work which has been published on the CFD modeling of room airflow, a summary table is provided at the end of the literature review section which includes the designation of driving force, process studied, flow regime, dimension, methodology and grid information. Pertinent information will be given in the text, and Table 1.3 has been added to provide a quick summary and comparison of relevant work.

1.2.1 CFD Technical Background

This section presents the general CFD methodologies used in this study, and should help clarify some of the modeling terminology used later. Most of the technical background is also included in Weathers' [1992] thesis. This section focuses on the differences between the three models used in this study which are a laminar model, a turbulent k-ε model with wall functions, and a turbulent k-ε low-Reynolds number model.

1.2.1.1 Laminar Model

If the flow is assumed not to be turbulent, or if one wishes to obtain a general idea of a turbulent flow, then a laminar model can be implemented. Laminar models are the most basic CFD models, and are much simpler than any of the turbulent models. In some cases it makes sense to use a laminar model to save computational effort and gain basic information even though the flow is believed to be turbulent.

The main equations which need to be solved in a CFD model are conservation of mass and momentum. The conservation of mass, or continuity, equation is:

$$\frac{\partial U_i}{\partial x_i} = 0 \tag{1.1}$$

The laminar, constant density, momentum equation based on the conservation of momentum in Eulerian form is:

$$\frac{\partial U_i}{\partial t} + U_i \frac{\partial U_j}{\partial x_j} = -\frac{\partial P}{\rho \partial x_i} + \nu \nabla^2 U_i + g_i \tag{1.2}$$

This is the Navier Stokes equation which together with the continuity equation provides a means for calculating the values of the three velocity components.

The conservation of energy equation for laminar flow can be written in Eulerian form as:

$$\frac{\partial T}{\partial t} + \frac{\partial}{\partial x_i}(U_i T) = \alpha(\nabla^2 T) \tag{1.3}$$

More about the previous equations will be presented later.

1.2.1.2 Turbulent Model

Turbulence modeling is much more complex than laminar modeling. One basic reason for the additional complexity is that when mean values plus turbulent fluctuations are substituted for velocities, Reynolds stresses result which lead directly to the well known closure problem of turbulence modeling. One good in-depth explanation of the closure problem is given by Hinze [1987]. What mathematically occurs is that one can derive an equation which describes the behavior of a velocity correlation, but in doing so one also creates a velocity correlation of a higher order. No matter how many equations one derives there will always be one too many dependent variables for a closed solution to be possible. Thus, the closure problem.

Because of the closure problem, many different types of models have been developed in order to obtain a turbulent solution. Most of the turbulent models in use today are included in one of the following categories of models: zero equation model, one equation model or two equation model. These models get their names based on the number of additional partial differential equations which are solved. Two equation models include the most popular turbulence models in use today and the models used in this study. Rodi [1980] describes the different classes of models and also provides information about the Reynolds stresses which illustrates the closure problem.

One type of two equation model is the k-ε model. k is the turbulent kinetic energy, and ε is the turbulent dissipation rate. The turbulent models used in this study are both versions of the k-ε model. The first type of turbulent k-ε model used is the standard k-ε model with wall functions which was introduced by Launder and Spalding in 1974. This model will be referred to throughout this thesis as the wall function model. The second turbulent model used in this study is the low-Reynolds number k-ε model developed by Lam and Bremhorst [1981].

The following basic equations are written in Eulerian form and are valid for both the turbulent wall function model and the turbulent low-Reynolds number model.

The turbulent continuity equation can be written as:

$$\frac{\partial \overline{U_i}}{\partial x_i} + \frac{\partial u_i'}{\partial x_i} = 0 \qquad (1.4)$$

where $\overline{U_i}$ = Mean velocity components
u_i' = Velocity component fluctuations

After velocity substitutions, time averaging, and assuming negligible viscous stresses, the turbulent conservation of momentum is:

$$\frac{\partial \overline{U_i}}{\partial t} + \overline{U_i}\frac{\partial \overline{U_j}}{\partial x_j} = -\frac{\partial P}{\rho \partial x_i} + \frac{\partial}{\partial x_j}\left[\nu_t\left(\frac{\partial \overline{U_i}}{\partial x_j} + \frac{\partial \overline{U_j}}{\partial x_i}\right) - \frac{2}{3}k\delta_{ij}\right] + g_i \qquad (1.5)$$

where ν_t is the turbulent viscosity which is defined by:

$$\nu_t = C_\mu F_\mu \frac{k^2}{\varepsilon} \tag{1.6}$$

where C_μ = constant coefficient and is usually considered to be 0.09
F_μ = 1.0 (except when using the low-Reynolds model)
ε = turbulent energy dissipation.
δ_{ij} = Kronecker delta defined by: $\delta_{ij} = 1$ for $i = j$
$\delta_{ij} = 0$ for $i \neq j$

k = turbulent kinetic energy, defined as: $k = \frac{1}{2}\overline{u_i u_i}$

The turbulent kinetic energy equation is:

$$\frac{\partial k}{\partial t} + \frac{\partial}{\partial x_j}(U_j k) = \frac{\partial}{\partial x_j}\left[\frac{\nu_t}{\sigma_k}\frac{\partial k}{\partial x_j}\right] + \nu_t \frac{\partial U_i}{\partial x_j}\left[\frac{\partial U_i}{\partial x_j} + \frac{\partial U_j}{\partial x_i}\right] - \varepsilon \tag{1.7}$$

The turbulent dissipation equation is:

$$\frac{\partial \varepsilon}{\partial t} + \frac{\partial}{\partial x_j}(U_j \varepsilon) = \frac{\partial}{\partial x_j}\left[\frac{\nu_t}{\sigma_\varepsilon}\frac{\partial \varepsilon}{\partial x_j}\right] + \frac{\nu_t C_1 F_1 \varepsilon}{k}\frac{\partial U_i}{\partial x_j}\left[\frac{\partial U_i}{\partial x_j} + \frac{\partial U_j}{\partial x_i}\right] - C_2 F_2 \frac{\varepsilon^2}{k} + E \tag{1.8}$$

The basic differences between the two turbulent models are how the functions are applied and the wall boundary conditions used. The turbulent functions, designated as F_μ, F_1, and F_2, are all equal to 1.0 when the wall function model is used. When using

the wall function model or the low-Reynolds number model, E is 0.0. The empirical functions for the low-Reynolds number model are:

$$F_\mu = \left(1 - e^{-(A_\mu R_y)}\right)^2 * \left(1 + \frac{A_t}{R_T}\right) \tag{1.9}$$

$$F_1 = 1 + \left(\frac{0.05}{F_\mu}\right)^3 \tag{1.10}$$

$$F_2 = 1 - e^{(-(R_T^2))} \tag{1.11}$$

where A_μ = A constant (0.0165)

A_t = A constant (20.5)

$R_y = \frac{\sqrt{k y_n}}{\nu}$ = Local Reynolds number

y_n = the normal distance to the wall (m).

$R_T = \frac{k^2}{\nu \varepsilon}$ = Turbulent Reynolds number

The differences in wall boundary conditions used in the two turbulent k-ε models are outlined in Table 1.1.

TABLE 1.1

k-ε WALL BOUNDARY CONDITIONS

	Wall Function Model	Low-Reynolds Number Model
Tangential Wall Velocity:	$\left.\frac{\partial U}{\partial x_n}\right\|_{wall} = \frac{m U_t}{y_n}$	Slip or No-Slip
Dissipation at the Wall:	$\varepsilon = \frac{(C_\mu^{0.5} k)^{1.5}}{\kappa y_n}$	$\varepsilon = \frac{2\nu k}{y_n^2}$

1.2.2 Nielsen

One of the first researchers to use 2-D turbulence modeling to predict air movement and heat transfer in buildings was Nielsen. By 1974, Nielsen had used k-ε modeling to simulate air movement in a room. Nielsen et al. [1978] demonstrated that room airflow predictions were sufficient for design purposes through comparison with experimental values. But, additional research was required for general modeling. At that time, Nielsen's modeling could not handle the flow through rooms with small inlets or relatively long rooms where flow instabilities may be expected.

In 1980, Gosman, Nielsen, Restivo, and Whitelaw used a three-dimensional model to study velocities, pressures, turbulent kinetic energy, and the dissipation rate. They studied different geometries with their k-ε model and found that the turbulent kinetic energy and dissipation length scale varied between 0.1 and 0.3. They stated that an algebraic approximation might replace the differential equations in order to reduce computer usage. Three-dimensional information about the flow patterns of rooms with small inlet regions was provided. They incorporated wall jet assumptions at the inlet to eliminate the need for a denser grid in that region. They also claimed that their value of the maximum velocity was accurate to within 5 percent.

1.2.3 Awbi

Significant numerical research in the areas of wall jets and room ventilation systems has been performed by Awbi. The k-ε turbulence model was used to solve 2-dimensional ventilation problems [Awbi, 1989a].

To evaluate ceiling diffusers, velocity profiles and temperature distributions from the 2-D program were compared to measured values from an experimental room which was designed especially for evaluating the performance of ceiling diffusers. Good agreement between experimental and numerical results existed except for near the floor. With the 3-D program, results were obtained for experiments with obstacles interrupting a wall jet. Awbi found that the obstacles enhance jet diffusion. In some instances the jet reattaches, but as the height of the obstacle was increased, so was the chance for complete separation.

The turbulent kinetic energy and dissipation at the inlet are calculated by:

$$k_{in} = \frac{3}{2} I_u^2 U_{jet}^2 \tag{1.12}$$

$$\varepsilon = \frac{k_{in}^{1.5}}{\lambda H} \tag{1.13}$$

where $I_u^2 =$ turbulence intensity of the x-velocity

$\lambda =$ a constant (≈ 0.005)

$H =$ room height or $\sqrt{\text{inlet area}}$ (m)

Also, for buoyancy-dominated flows, improved wall functions are needed [Awbi, 1989a].

CFD techniques were shown to be a useful tool with practical applications by Awolesi, Awbi, Seymour and Hiley [1991]. They studied ventilation and contamination problems in an industrial workshop, conducted measurements and performed computational analysis on the air movement. Further analysis is necessary to provide an evaluation of Awolesi's solution to the ventilation problem.

In addition to industrial workshops, numerical simulations were performed on the air movement in offices, classrooms and clean rooms [Awbi, 1991]. Awbi concentrated on human comfort.

In 1989 Awbi noted that more work was needed before CFD programs could be used as design tools. Awbi also stated in 1991 that considerable progress was still needed to improve computational modeling in terms of grid coverage, stability algorithms and boundary conditions.

1.2.4 Chen

In 1990 Chen applied the k-ε model developed by Lam and Bremhorst to cavity flow. Most of his work dealt with the prediction of velocity and temperature distributions in an enclosure with natural convection flow. It was concluded that when one wishes to calculate dynamic indoor air movement near a wall, the low Reynolds number k-ε model will produce a more accurate velocity profile. He also found that more realistic convective heat transfer results occur from the walls to the room when one uses the low Reynolds number model.

The Boussinesq approximation could be used because the temperature difference in the room was relatively small. The Boussinesq approximation for buoyancy was implemented by adding the following term to the momentum equations.

$$\beta (T - T_0) g_i \tag{1.14}$$

And, source terms were also added to the turbulent kinetic energy equation,

$$S_k = \frac{\beta \nu_t \partial (T - T_o)}{\sigma_h \partial x_i} g_i \qquad (1.15)$$

where h is enthalpy, and the dissipation source term is as follows.

$$S_\varepsilon = \frac{1.44\varepsilon}{k} S_k \qquad (1.16)$$

Chen validated the low Reynolds number turbulence model through comparison with experimental cavity flow data and showed that the high Reynolds number model with wall functions did a poor job of predicting the near-wall velocity profile.

Because the distance from the wall to the first grid point in most room simulations is greater than the thickness of the boundary layer, Chen claimed that the high Reynolds number k-ε model is not suitable for the room airflow application for heat transfer analysis. This is because the convective heat transfer coefficients from the high Reynolds number model are inaccurate [Chen, et al., 1990b]. The high Reynolds number model uses experimental approximations and does not determine the wall heat transfer in the inner layer of the boundary layer which makes it impossible to obtain the heat loss and heat gain through the boundaries computationally.

In addition to computational analysis of cavity flows, Chen and van der Kooi have performed combined energy analysis, indoor airflow, and air quality research. The ACCURACY program was developed to aid in this type of combined research. Chen

and van der Kooi have used ACCURACY to analyze displacement ventilation systems [1990a].

Chen and Jiang [1992a] state that with simple thermal and flow boundary conditions, the standard k-ε model may correctly predict room airflow. They also point out that most standard k-ε models use semi-empirical wall function formulas when predicting the heat transfer on a solid surface. But for room airflow, the wall function method is not suitable. The low-Reynolds number k-ε models are also difficult to use properly because too many grid points are required in the near-wall region [Chen and Jiang, 1992a].

Thermal comfort and indoor air quality have been analyzed with a low Reynolds number k-ε model while varying the location and type of diffuser [Chen, Moser, Suter, 1992c]. Their study has shown that both the diffuser type and location have an impact on thermal comfort and indoor air quality. Therefore, if computational airflow simulations become more accurate and dependable, then air quality and thermal comfort can be better analyzed and improved.

1.2.5 Murakami

Many aspects of computational room airflow have been investigated by Murakami. Three dimensional simulations of ventilated rooms were performed [Murakami, et al., 1987] with "fairly good agreement" between computational and empirical results. According to Murakami, one of the most appropriate uses for the k-ε model is modeling airflow in clean rooms where the number of air changes per hour are very high and turbulent flow will most certainly occur. Murakami, et al. used the wall function method in their analysis. Dimensionless physical quantities were obtained which corresponded to

experimental values "quite well". Murakami concluded that the k-ε model can appropriately be used to model airflow in clean rooms. It was also pointed out that the computational results have been compared to empirical mean velocity data. Their turbulence model was only reliable for turbulent flows, and should not be applied out of context.

Murakami's simulation of clean rooms continued. In 1989, Murakami, Kato, and Suyama released results of research which dealt with turbulent diffusion fields and how they are affected by variations in the inlet and outlet. The geometry of the inlet openings and the location, size and number of outlets were varied. Techniques for modeling the boundary conditions at the wall from the log-law and the power law were recognized, outlined, and implemented. Three types of log-law techniques and a power law type boundary condition were studied and produced similar results. Therefore the power law type of boundary condition is preferred because of simplicity [Murakami et al., 1989c]. More about the power law boundary condition is given in section 2.4.1.1 of this report.

Murakami and Kato used the k-ε model to predict three-dimensional turbulent recirculating flows in ventilated rooms. In addressing problems of the k-ε model, Murakami and Kato suggested more complex turbulence modeling to handle the effect of buoyancy and boundary fitted coordinates to simulate complicated room geometries.

Murakami, Kato and Ishida have published details on how to simulate complex geometries with the k-ε model [1989d]. Their method of using generalized curvilinear coordinates is necessary for complex geometries because a normal, rectangular Cartesian grid does not sufficiently match the boundaries. Their grid system fits a curve to the boundary and alters the distance between nodes. The grid can then be transformed from generalized curvilinear coordinates to a rectangular grid.

1.2.6 Haghighat

Room configurations with interior partitions present a different set of problems for the field of CFD. Haghighat, Jiang, and Wang [1989] have explored the airflow patterns, natural convection, and contaminant dispersion of two-zone enclosures.

An open doorway in an interior partition was varied in height, size and location, and its effect on airflow and temperature were studied. Results have shown that the convective heat transfer rate is not sensitive to partition location, while room airflow patterns are sensitive to both door height and location [Haghighat, et al., 1989].

In additional experiments, the inlet and outlet locations along with door positions were varied. The most prominent results from these experiments show that the door location controls the direction and magnitude of air movement in the downstream zone.

Haghighat et al. mainly used the SIMPLE and PHOENICS codes to solve the finite difference equations and predict two and three-dimensional heat and mass transfer in building airflow. They note that at the wall, the turbulent viscosity no longer dominates over the viscous effects. Much like Murakami's approach, wall functions which use an equation for the momentum flux due to shear stress and an equation for the heat flux at solid surfaces were utilized in Haghighat's analysis. A grid sensitivity analysis revealed the most practical density of nodes to use. They used a 10x10x16 system for natural convection analysis of an enclosure with dimensions of 10m x 4m x 3m. But for forced convection, a smaller grid is recommended because of the more complicated boundary conditions [Haghighat, et al., 1992].

1.2.7 Spitler

Air movement and convective heat transfer in buildings were researched by Spitler [1990]. A full scale experimental facility, 2.74 x 2.74 x 4.57m, with the ability to change the inlet location, hold the room surfaces at a constant temperature and vary the flow rate between 2 and 100 air changes per hour was used to obtain experimental room airflow measurements. The experimental results from this facility were used to validate the CFD models of Williams, Baker, and Kelso [1994], Weathers [1993], and has also been used for comparison to this project's results.

The facility allowed for two inlet configurations. The first configuration was a sidewall inlet with dimensions of 0.4 m. x 0.9 m. A radial ceiling diffuser 0.4 m. x 0.4 m. was the other option. The outlet of the facility was 0.4 m. x 0.9 m. and was located in the lower corner of a sidewall. (see Figure 1.1).

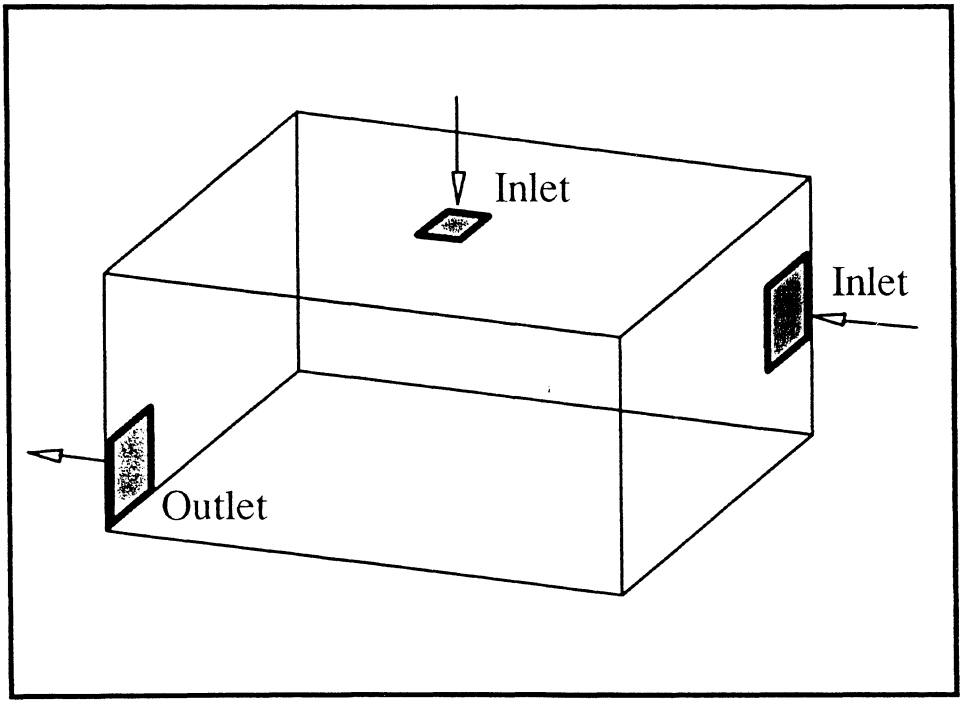

Figure 1.1 Experimental Facility

Sixteen omnidirectional air velocity transducers and type T thermocouples were attached to a trolley system on rails which enabled the facility user to obtain velocity and temperature measurements at desired locations. For each experiment, values were determined approximately 1 ft. apart throughout the entire volume of the room.

In order to control the surfaces of the facility isothermally, 53 individually controlled panels covered the interior room surfaces. Each panel could be operated in a low or a high power mode and was heated with nickel chromium resistance wire. This technique allows the heat flux of the panels to be determined, which lead to an experimentally determined film coefficient from the following equation [Spitler, et al., 1991a, 1991b].

$$h = \frac{q''_c}{(T_s - T_r)} \tag{1.17}$$

where q''_c = convective heat flux (W/m^2)

T_S = surface temperature ($^\circ$ C)

T_r = reference temperature ($^\circ$ C)

The room outlet temperature, bulk air temperature, air temperature adjacent to a surface, and local air temperature as a function of height were all investigated for use as possible reference temperatures, but the room outlet temperature was used [Spitler, et al., 1991b].

1.2.8 Weathers

A comparative study of room airflow, which provides the basis on which the present research is being conducted, was performed by Weathers [1992]. This project uses Spitler's experimental data for CFD verification just as Weathers' research did. Weathers analyzed a laminar model, k-ε model with wall functions, and the Lam-Bremhorst version of low-Reynolds k-ε model. For each of these three models, he performed simulations at four different airflow rates, 15, 30, 50, and 100 air changes per hour (ACH).

In order to match Spitler's experimental data better, Weathers used measured inlet velocity profiles in his computational models. More information about the inlet profiles used in Weathers' study and in the present study is available in section 2.4.2 and in Table 2.2.

Weathers investigated grid independence with five different uniform grids which ranged from "very course", 10 x 6 x 6, to "ultra fine", 46 x 30 x 30. He concluded that a "very fine", 40 x 24 x 24 grid produced sufficient accuracy.

The wall boundary conditions were varied and the free slip wall boundary condition was found to match the experimental data better than the no slip condition. Weathers' free slip boundary condition recommendation makes sense because the uniform grid used in the computational analysis, 40 x 24 x 24, does not include grid points close enough to the walls. The uniform grid used by Weathers had 24 cells in the z-direction within the 2.75 (m) distance which made each full cell 11.46 cm. wide. Because the Marker-and-Cell method [Harlow and Welch, 1965] was used, the tangential velocity vectors in the cells closest to the wall occur half a cell away from the wall at the cell face. For

diagrams and a more detailed explanation of the Marker-and Cell method, see section 2.2. Weathers' tangential wall velocities were 5.73 cm. away from the wall.

In order for a no slip condition to be necessary, the grid should be small enough so that the grid points closest to the wall are included in the boundary layer. If one is interested in boundary layer information, then one should use as small a grid as possible, because as the distance between the first node and the wall decreases, the accuracy of the computational model should increase. If the grid chosen does not contain nodes inside the boundary layer, then boundary layer and slip information is unattainable and the free slip boundary condition is the logical and appropriate choice.

A problem in a majority of prior computational room airflow experiments is that the comparison to experimental results is rather vague and subjective. In order to quantitatively evaluate his computational results, Weathers defined a global error number as:

$$GEN = \frac{\overline{E}_{abs}}{V_{max}} \tag{1.18}$$

where $\overline{E}_{abs}$ = average absolute error $\left(\frac{1}{n}\sum_{i=1}^{n} E_{abs\,i}\right)$

V_{max} = maximum velocity magnitude from experimental data.

E_{abs} = |numerical velocity magnitude - experimental velocity magnitude|

The global error number compares the computational results to the entire experimental domain. Table 1.2 is presented below which summarizes Weathers' reported global error numbers for each of the 12 computational cases he performed.

TABLE 1.2

WEATHERS' REPORTED GLOBAL ERROR NUMBERS
[Weathers, 1992]

Model	15 ACH	30 ACH	50 ACH	100 ACH
Laminar	0.0498	0.0570	0.0767	0.0796
Turbulent- Wall Functions	0.0505	0.0560	0.0683	0.0743
Turbulent- Low-Reynolds	0.0358	0.0449	0.0554	0.0596

Based on the GEN analysis, the low-Reynolds number k-ε model was determined to match the experimental data closer than the other computational models.

Weathers provides information on the low-Reynolds number k-ε models, constants and functions which are used in the turbulent analysis by Launder-Sharma, Chien, and Lam-Bremhorst. Many researchers have their own opinion about what turbulent constants and functions should be used. This accounts for many of the modifications which have been made to the basic k-ε model.

1.2.9 Baker

Code validation is a legitimate concern when dealing with nearly any type of computational analysis. The CFD methodology for room airflow is no different. Baker and Kelso [1990] have attempted to define code validation issues.

Kelso, Wilkening, Schaub, and Baker [1992] have modeled commercial, kitchen exhaust hoods using finite element analysis because experimental analysis would be difficult and costly. The concluded that their 2-D model must be extended to three dimensions and more detail in filter modeling and hood configurations should be implemented.

Baker, Williams and Kelso published a three-part article in 1994 which outline CFD methods, introduce a finite element method and use Spitler's experimental indoor room airflow data to compare to their CFD models. Therefore, some of the geometries investigated are identical to the geometry in the present study. Part I discusses CFD techniques, basic equations, and issues of modeling. Finite-volume and finite-element semi-discrete spatial constructions were examined.

Part II details the continuity constraint finite element method CFD algorithm. Computational results for benchmark problems were presented for validation. Two-dimensional and three-dimensional natural convection cavities and step-wall diffusers were simulated using the continuity constraint method (CCM), which is a pressure relaxation method.

In the third article of the series, Spitler's full-scale experimental room data is utilized for comparison at 15 and 30 air changes per hour (ACH). The non uniform 3-D CFD grids were generated with the INGRID mesh generator. The levels of turbulence were varied and the 3-D flow effects were studied. Williams, Baker and Kelso conclude that Spitler's 15 ACH data appears to be a low-turbulence-level room air experiment. The 30 ACH CFD velocity magnitude results did not match the experimental results as well as the 15 ACH velocity magnitude results. They also concluded that the computed flows were determined to be strongly three-dimensional and complex.

1.2.10 Sakamoto

In order to test the practicality of computationally predicting 3-D turbulent flow in a ventilated room, Sakamoto and Matsuo [1980] experimented with the Deardorff's model of turbulence [Deardorff, 1970] and the k-ε model. The room was a 2 x 2 x 2m cube with a square ceiling inlet and a square exhaust outlet at one of the walls and was modeled with an 18 x 18 x 18 grid. The results from the two models were nearly identical, and compared well to experimental mean velocity data which was taken with an ultrasonic anemometer with a 10 cm. probe span. Because Deardorff's model requires more computer usage, Sakamoto recommended the k-ε model.

1.2.11 Kurabuchi

Kurabuchi has performed indoor air movement and heat transfer simulation using the k-ε model and the large eddy simulation (LES) method while utilizing the Marker-and-Cell grid method [Harlow and Welch, 1965]. Large eddy simulation advantages are noted, but computational complexities have limited the use of the LES method. Experiments were performed for a laboratory with two open windows on one wall, an open doorway on the opposing wall, and a mechanical ventilation device, or fume hood on the sidewall [Kurabuchi 1987].

1.2.12 Li

A 3-D numerical code has been developed by Li which uses a k-ε model with the Boussinesq approximation and a two-band radiation model. This finite difference code simulates turbulent air flows in single and multi-rooms and solves the transient-state conservation equation for mass, momentum, and thermal energy. Non-uniform grids and local refinements are possible with the code. The effects of wall insulation and radiation for partially divided rectangular enclosures were studied [Li, et al., 1991a].

Experiments involving forced convection, natural convection and radiation were performed to evaluate the code. Refined grids were found to improve the accuracy of velocities and temperature predictions. Fine grids and a proper distribution of grid points are both needed to achieve accurate computational results. Like Chen [Chen, et al., 1990b], Li also concludes that the high-Reynolds number model with wall functions is not practical for indoor room airflow because it does not determine the wall heat transfer in the inner layer of the boundary layer. Most HVAC engineers are interested in obtaining the heat loss and heat gain through the boundaries [Li, et al., 1991b].

1.2.13 Alamdari

The need for computational fluid analysis is outlined and critiqued by Alamdari. Alamdari found that CFD models were capable of simulating complicated room airflow and heat transfer problems, but require a significant amount of computer time and are difficult to use [Alamdari 1991a]. Airflow and thermal analysis of the headquarters for Hoare, Lea and Partners, which are naturally-ventilated two-story buildings, helped the owners make heating and cooling decisions [Alamdari, et al., 1991b].

1.2.14 Setrakian

Because the range of applications for computational fluid programs varies greatly, a customized CFD room airflow program has important advantages. Setrakian and Morgan [1991a] describe these advantages while presenting airflow results from their "ARIA" program for a room with a single inlet, dual outlets, and interior obstacles.

ESP, a building energy simulation code, provides boundary condition information for the ARIA airflow simulation program. This approach was taken to increase the level of accuracy and confidence in the boundary conditions input to the CFD analysis. Further developments suggested by Setrakian [1991b] include the merging of the two programs so that the CFD program could automatically receive thermal information at every time step.

1.2.15 Yau

Computational fluid dynamics has also been applied to large spaces in buildings. Yau and Whittle [1991] modeled summer and winter operation of an airport terminal building to improve thermal comfort and air quality. They implemented curvilinear coordinates in order to model the curved ceiling of the airport terminal building. A scaled down model of the building was used to obtain experimental results. Smoke movements in the model helped to establish flow patterns at different temperatures, flow rates, and angles of trajectory relative to the roof. This smoke testing was then used to compare with the computational results Yau and Whittle concluded that CFD is a valuable tool in the design process.

1.2.16 Schaelin

Schaelin, van der Maas and Moser [1992] have simulated the coupling of indoor airflow to outdoor flow through large openings. The effect of wind on their configuration was studied in two and three dimensions, and their numerical data agreed well with analytical models which are well supported by experiments.

1.2.17 Schachenmann

In order to check room air currents, experimental measurements and numerical calculations were made for a 6.75 x 4.50 x 2.97 m room with mobile interior partitions. Instead of defining a fine grid at the inlet, Schachenmann et al. used an "equivalent boundary surfaces" technique. The radiation heat exchange is being added to the CFD program used for the [Schachenmann, et al., 1990] results.

1.2.18 Tsutsumi

3-D k-ε and large eddy simulation computational methods were used to obtain data for comparison to naturally ventilated room airflow. The experimental model was designed to measure air speed caused by natural cross-ventilation through large openings. Because the experimental measurement of wind through a building is rare, Tsutsumi's research is relatively unique. The k-ε model results were found to match the experimental values closer than the LES results [Tsutsumi, et al., 1988].

1.2.19 Vazquez

The effect of air inlet location on the ventilation patterns inside an auditorium was studied by Vazquez, Samano, and Yianneskis [1991]. The flow patterns and temperature fields were greatly impacted by the inlet location. An optimum inlet location, based on thermal comfort, was obtained for the auditorium [Vazquez, et al., 1991].

1.2.20 Yamazaki

According to Yamazaki, Komatsu and Otsubo, when modeling air conditioned flow into a room, the buoyant force has an important role in determining air temperature and flow distribution. Flow patterns, semi-open rooms, and large interior spaces can be modeled with a computational program and the results can be helpful in the design of an air conditioning system [Yamazaki 1987].

1.2.21 Barozzi

Many researchers have verified CFD results with experimental results from a scaled down model. Barozzi et al. [1991] used a 1/12th scale model to compare to numerical results for a bioclimatic building based on solar-driven ventilation. This study investigated the thermosyphon principle. The computational field was solved in two dimensions, and favorable agreement existed between CFD and experimental results.

1.2.22 Literature Review Summary & Table

The following summary table, 1.3, has been included to give the reader a comparative description of the numerical methods covered in this review. The table presents the driving force, the process studied, the flow regime, the number of dimensions, the solution methodology, and information about the grid.

TABLE 1.3

SUMMARY OF LITERATURE REVIEW

	Driving Force	**Process Studied**	**Flow Regime**	**Dim.**	**Methodology**	**Grid**
Author, Year	F- forced N- natural B- both	C- conv h. t. A- airflow B- both	L- lam. T- turb. B- both	2-D 3-D Both	FD-finite diff LES-lrg eddy simulation WF-wall funct LR-low-Re #	U - uniform NU- non-uniform BF - body-fitted CC - curvilinear coords
Alamdari, 1991a	B	B	B	3-D	FD	NU, BF
Alamdari, 1991b	N	B	T	3-D	FD	NU
Awbi, 1989a	F	B	T	B	FD, WF	NU, 20x20x11
Awbi, 1991	F	B	T	3-D	FD, WF	NU, 40x24x20
Awolesi, 1991	F	A	T	3-D	FD, WF	NU, 45x52x33
Baker, 1990	B	B	T	B	WF, LR	U, NU
Barozzi, 1991	N	C	L	2-D	FD	NU, 56x96
Chen, 1990a	N	B	T	3-D	FD, LR	NU
Chen, 1990b	B	B	T	B	FD, LR	NU, 53x53
Chen, 1992a	F	A	T	2-D	LES, LR	NU
Chen, 1992c	F	A	T	3-D	FD, LR	NU
Gosman, 1980	F	A	T	3-D	FD, k-ε	U, 13x15x8
Haghighat, 1989	B	C	T	3-D	FD, k-ε	NU, 16x10x10
Haghighat, 1992	B	B	B	B	FD, WF	NU, 10x10x16
Kelso, 1992	F	A	B	2-D	Finite element	NU, 50x50
Kurabuchi, 1987	N	B	T	B	FD, LES	U, 30x20x15

TABLE 1.3 (cont.)

Author, Year	Driving Force F- forced N- natural B- both	Process Studied C- conv h. t. A- airflow B- both	Flow Regime L- lam. T- turb. B- both	Dim. 2-D 3-D Both	Methodology FD-finite diff LES-lrg eddy simulation WF-wall funct LR-low-Re #	Grid U - uniform NU- non-uniform BF - body-fitted CC - curvilinear coords
Li, 1991a	B	A	T	2-D	FD, k-ε	NU
Li, 1991b	B	B	T	3-D	FD, k-ε	NU
Murakami, 1987	F	A	T	3-D	FD, k-ε	NU
Murakami, 1989b	F	A	T	3-D	FD, k-ε	NU
Murakami, 1989c	F	A	T	3-D	FD, k-ε	NU, 46x46x17
Murakami, 1989d	B	A	T	3-D	FD, k-ε	CC
Nielsen, 1978	F	A	T	2-D	Stream function	20x20
Sakamoto, 1980	F	A	T	3-D	FD, LES	U, 18x18x18
Schachenmann, 1990	B	B	B	3-D	FD, k-ε	U, NU
Schaelin, 1992	N	B	B	B	FD, k-ε	NU
Setrakian, 1991a	F	B	B	3-D	FD, k-ε	NU
Setrakian, 1991b	B	A	B	3-D	FD, k-ε	NU
Tsutsumi, 1988	N	A	T	3-D	FD, LES	U, 5x5x5
Weathers, 1993	F	A	B	3-D	FD, WF, LR	U, 40x24x24
Yamazaki, 1987	B	B	T	3-D	FD, k-ε	NU
Yau, 1991	F	A	B	B	FD, k-ε	CC

1.3 Objectives

The objectives of this project include the production of a variable grid 3D transient turbulent buoyant code for the simulation of room airflow. Results of constant and variable grid models will be compared to experimental results and to previous computational results.

Improved visualization is necessary in order to add insight about the behavior of the transient simulations. Two and three dimensional visualization tools will be used in conjunction with model results to assure convergence and allow easier error detection.

The feasibility of predicting room surface convection coefficients will also be evaluated in this project. Wall temperature boundary conditions will be varied. Outlet temperatures and predicted convection coefficients will be monitored.

2.0 SOLUTION METHODOLOGY

The research for this project was performed with a finite difference FORTRAN program which uses 3-D Cartesian coordinates and calculates the velocity, temperature, pressure, contaminant distribution, turbulent kinetic energy, and turbulent dissipation. The program provides variable grid spacing and a choice of post processing options to the user. This program is based on the GEneral 3-Dimensional Flow (GE3DF) laminar, constant density code written by D. G. Lilley (1991). The GE3DF code was modified by J. W. Weathers in 1992 to handle turbulent, buoyant flows. Both of these predecessor programs use the Marker-and-Cell method [Harlow and Welch, 1965] which will be discussed in more detail later in this report.

2.1 Solution Procedure

Details of the approach used to solve for the velocities and scalar quantities are included in this section. First the geometry, grid spacing, initial conditions, some boundary specifications, physical properties, and other necessary information are read into the program. The program calculates additional geometric and numerical parameters such as the volume flow rate, the number of air changes per hour (ACH), and the areas of the inlet and outlet. After initial values and boundary conditions are imposed, time advanced velocity components, temperature, mixture fraction, turbulent energy and turbulent dissipation values are calculated for the entire 3-D domain. Boundary conditions are updated after the determination of time advanced values.

Next, the continuity equation is satisfied using the change in pressure as a correction factor for the time advanced velocity components. After continuity is satisfied, residual

terms for the velocities and mixture fraction are calculated based on the amount of change in the values from the previous time step.

At this point in the solution process, a check for convergence is performed. If the values have not converged, then another time step must be performed. So, the time advanced values are shifted to the old memory locations, and time is advanced one step. Then, new time advanced values can be calculated. This process continues until convergence has been achieved.

Figure 2.1 is a flowchart which summarizes the solution methodology of the finite difference code used in this study.

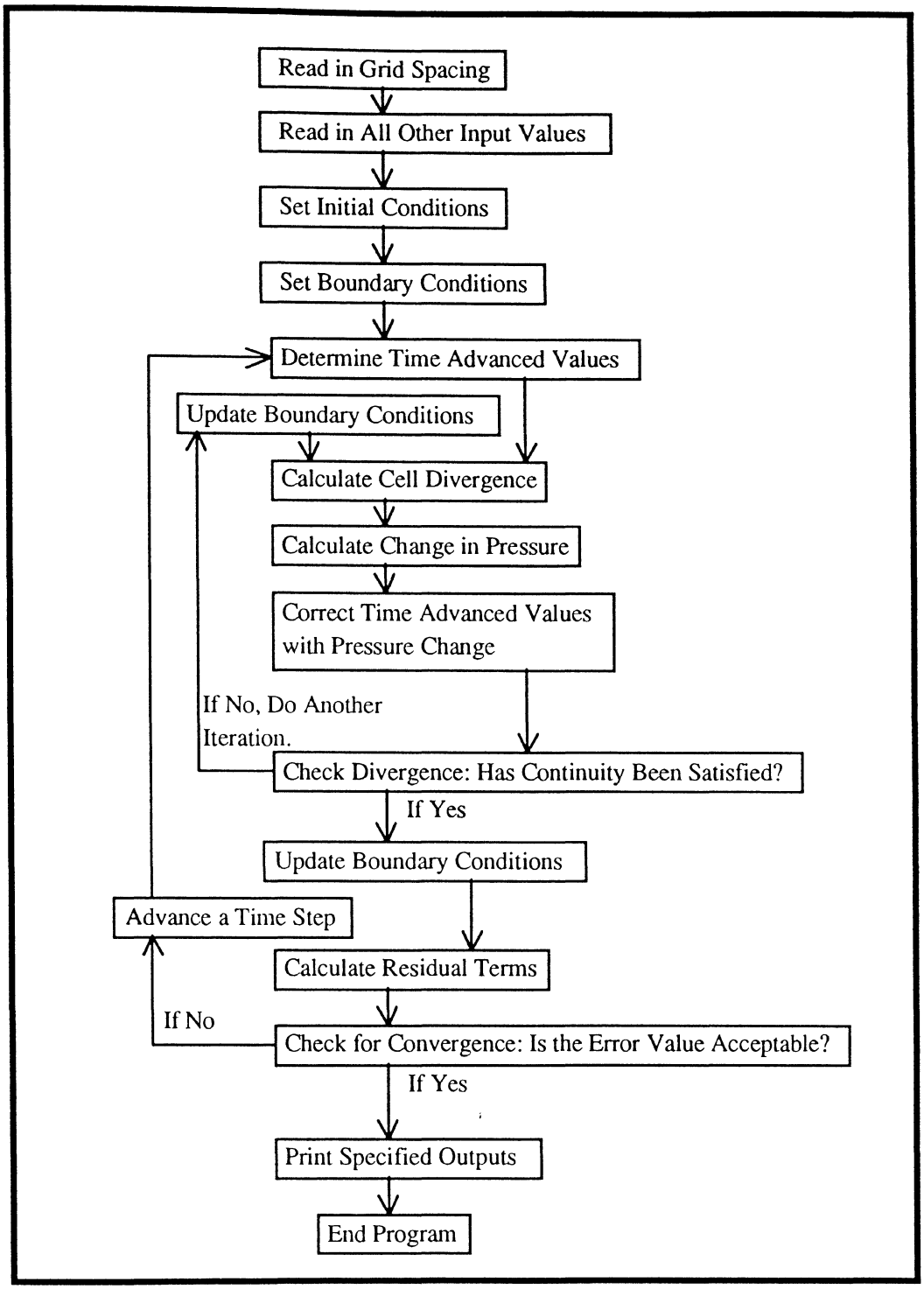

Figure 2.1 Solution Methodology Flow Chart

2.2 Marker-and-Cell Method

The Marker-and-Cell, (MAC), method was developed by Harlow and Welch [1965], and it forms the basis for the finite difference computational fluid dynamics techniques implemented in this research. The MAC method has been used by Lilley [1988] and Weathers [1992], whose work forms the basis of this project, and has also been utilized by other room airflow researchers such as Murakami [1987] and Awbi [1989a].

The Marker-and-Cell method defines all scalar quantities at the center of the cell, but the velocity vectors are defined at the center of the appropriate cell face as shown with the 3-dimensional Figure 2.2 and in 2-dimensions in Figure 2.3.

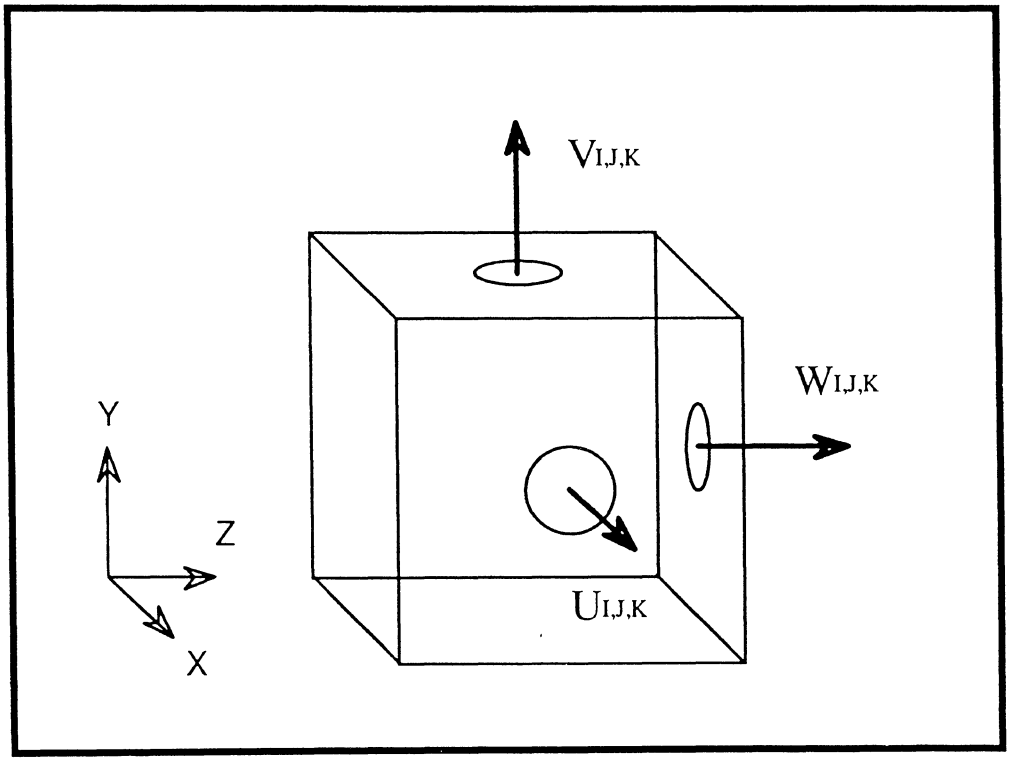

Figure 2.2a Three-Dimensional View of MAC Velocities

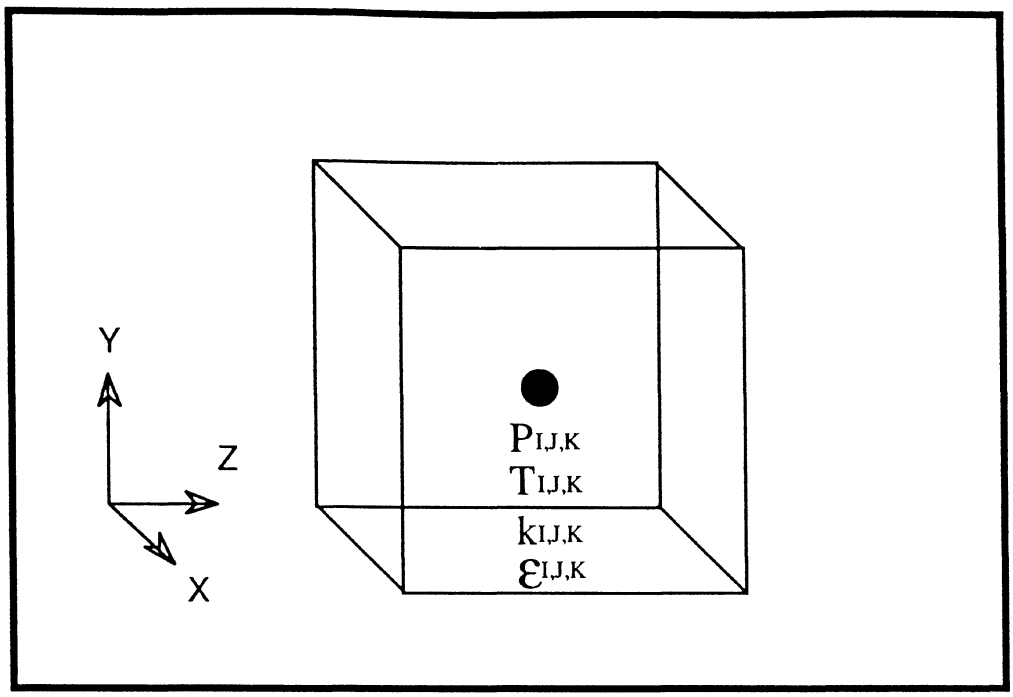

Figure 2.2b Three-Dimensional View of MAC Scalar Quantities

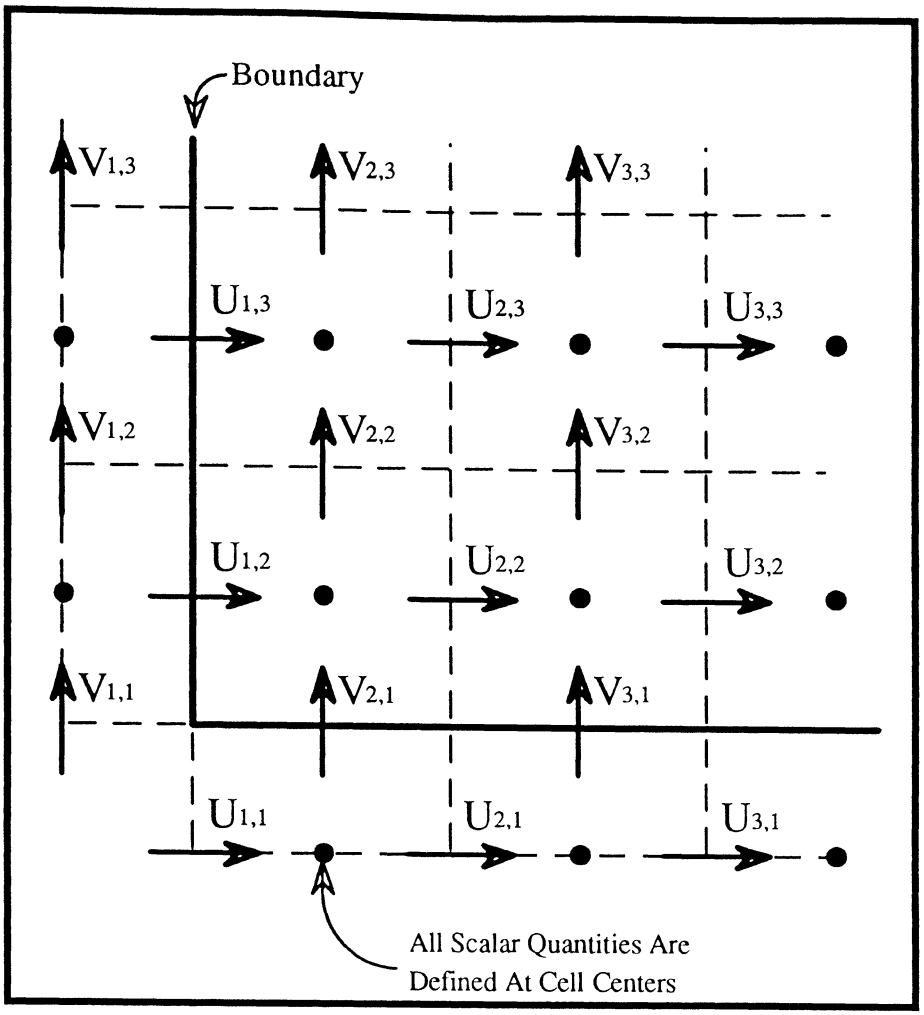

Figure 2.3 Two-Dimensional View of MAC Cell Layout

In Figure 2.3, the w velocity component is not shown because it exists outside the plane of the page. Notice that the velocities are defined half a cell from the location of the scalar quantities, and that the velocity magnitudes represent the speed of the fluid moving across that particular boundary or cell face.

2.3 Finite Difference Methodology

The basic equations for laminar and turbulent numerical fluid dynamics and the finite difference equations which stem from the basic equations are contained within this section. The equations presented here apply to a constant density room airflow with Cartesian coordinates and variable grid spacing. For constant grid space equations, and additional discussion, see Weathers [1992].

As mentioned in previous sections, the program used to model room airflow for this research uses a transient finite difference model to solve a laminar or turbulent flow field. Buoyancy can be implemented in the constant density solution process by using a coefficient of thermal expansion to model the changes in density due to temperature differences. The turbulent models are solved using the k-ε model. The main equations necessary in this type of turbulence model are continuity, momentum, scalar equations, and of course, the k and ε equations. The discussion which follows states the equation, any changes for turbulence modeling, and the finite difference form of the equation. According to Rodi [1980], the mean flow quantities are of practical interest while specific information about the turbulent fluctuations is less useful. This is also true for the specific application to room airflow, and it should be kept in mind that accurate prediction of mean values are the main concern in this analysis.

2.3.1 Continuity Equation

Conservation of mass for a constant density situation can be written as

$$\frac{\partial U_i}{\partial x_i} = 0 \tag{2.1}$$

Whereas a turbulent form of the continuity equation is:

$$\frac{\partial \overline{U_i}}{\partial x_i} + \frac{\partial u_i'}{\partial x_i} = 0 \tag{2.2}$$

The first term of equation (2.2) represents the change in mean velocity with position, and the second term represents the gradient of turbulent velocity fluctuations. Because the turbulent mean velocity and turbulent velocity fluctuations must both satisfy continuity, and this project deals with mean values, the second term of equation (2.2) can be subtracted out to yield the continuity equation used in this project.

$$\frac{\partial \overline{U_i}}{\partial x_i} = 0 \tag{2.3}$$

This approach to the continuity equation is especially convenient from the perspective of code writing because it means that the turbulent velocity fluctuations in the continuity equation can be ignored. This makes the form of equation (2.3) like equation (2.1) and therefore the solution procedures for turbulent and laminar continuity equations are able to be performed identically. The difference is that if the solution method is turbulent, then the velocities involved are always mean values.

Equation (2.1) in Cartesian form is:

$$\frac{\partial U}{\partial x} + \frac{\partial V}{\partial y} + \frac{\partial W}{\partial z} = 0 \tag{2.4}$$

With the physical significance of the continuity equation and the Marker-and-Cell method of section 2.2 in mind, it is easy to see the transition to a finite difference equation. Each of the three terms of equation (2.4) can be written in finite difference terms by stating that the derivative of a velocity with respect to position is the difference between the velocity out of the cell minus the velocity in to the cell divided by the distance between the cell faces, and velocity vectors.

The finite difference form of the continuity equation is:

$$\frac{U_{i,j,k} - U_{i-1,j,k}}{\Delta x_{\alpha i}} + \frac{V_{i,j,k} - V_{i,j-1,k}}{\Delta y_{\alpha j}} + \frac{W_{i,j,k} - W_{i,j,k-1}}{\Delta z_{\alpha k}} = 0 \qquad (2.5)$$

Where $\Delta x_{\alpha i}$, $\Delta y_{\alpha j}$, and $\Delta z_{\alpha k}$ are the distances between the appropriate velocity vectors.

2.3.2 Momentum Equations

The constant density momentum, or Navier Stokes, equations are given in Eulerian form in the following equation.

$$\frac{\partial U_i}{\partial t} + U_i \frac{\partial U_j}{\partial x_j} = -\frac{\partial P}{\rho \partial x_i} + \nu \nabla^2 U_i + g_i \qquad (2.6)$$

The equation used for turbulence modeling is different and is shown in the following equation. The bars over the velocities denote mean velocity values.

$$\frac{\partial \overline{U_i}}{\partial t} + \overline{U_i}\frac{\partial \overline{U_j}}{\partial x_j} = -\frac{\partial P}{\rho \partial x_i} + \frac{\partial}{\partial x_j}\left[\nu_t\left(\frac{\partial \overline{U_i}}{\partial x_j} + \frac{\partial \overline{U_j}}{\partial x_i}\right) - \frac{2}{3}k\delta_{ij}\right] + g_i \quad (2.7)$$

Equation (2.7) above is obtained as a result of substituting the velocity components with the mean values and fluctuations and then taking the time average. Another important step in the derivation is the assumption that the viscous stresses are negligible.

The finite difference equations calculate a new velocity value based on the old values of velocities and pressures on the right hand side of the equation. Not that the P's in the finite difference equations represent the ratio of the pressure to the density, and not just the pressure as in the previous equations. A constant density finite difference form of equation (2.6) explicitly solved for the time advanced laminar U value is:

$$U_{i,j,k}^{new} = U_{i,j,k}^{old} + \Delta t\left[\frac{P_{i,j,k} - P_{i+1,j,k}}{\Delta x_i} + g_x + VISX - FUX - FUY - FUZ\right] \quad (2.8)$$

Where the viscous fluxes are included in the VISX term, and the convective fluxes are denoted by the FUX, FUY, and FUZ terms. The viscous flux term in expanded finite difference form is given below.

$$VISX = \nu\left[\left(\frac{U_{i+1,j,k} - U_{i,j,k}}{\Delta x_{ci+1}} - \frac{U_{i,j,k} - U_{i-1,j,k}}{\Delta x_{ci}}\right)\Big/\Delta x_i\right. \quad (2.9)$$

$$+\left(\frac{U_{i,j+1,k} - U_{i,j,k}}{\Delta y_j} - \frac{U_{i,j,k} - U_{i,j-1,k}}{\Delta y_{j-1}}\right)\Big/\Delta y_{cj}$$

$$\left.+\left(\frac{U_{i,j,k+1} - U_{i,j,k}}{\Delta z_k} - \frac{U_{i,j,k} - U_{i,j,k-1}}{\Delta z_{k-1}}\right)\Big/\Delta z_{ck}\right]$$

Where Δx_{ci+1} represents both the distance between $U_{i+1,j,k}$ and $U_{i,j,k}$ and the width of cell i+1 in the x direction. The Δx_i term represents the distance between the midpoints of cells i and i+1 in the x direction. The reason for the designation of separate distances is because the above finite difference equation has been written for a variable grid spacing. As previously mentioned, Weathers [1992] describes the equivalent constant grid spaced equations.

The convective flux terms are as follows.

$$FUX = \frac{1}{4}\{[(U_{i,j,k}+U_{i+1,j,k})^2 + \overline{\alpha}\ |U_{i,j,k}+U_{i+1,j,k}|*(U_{i,j,k}-U_{i+1,j,k})]/\Delta x_{ci+1} \quad (2.10)$$
$$-[(U_{i-1,j,k}+U_{i,j,k})^2 + \overline{\alpha}\ |U_{i-1,j,k}+U_{i,j,k}|*(U_{i-1,j,k}-U_{i,j,k})]/\Delta x_{ci}\}$$

$$FUY = \frac{1}{4}\{[(V_{i,j,k}+V_{i+1,j,k})*(U_{i,j,k}+U_{i,j+1,k}) + \overline{\alpha}\,|V_{i,j,k}+V_{i+1,j,k}|*(U_{i,j,k}-U_{i,j+1,k})]/\Delta y_j \quad (2.11)$$
$$-[(V_{i,j-1,k}+V_{i+1,j-1,k})*(U_{i,j-1,k}+U_{i,j,k}) + \overline{\alpha}\,|V_{i,j-1,k}+V_{i+1,j-1,k}|*(U_{i,j-1,k}-U_{i,j,k})]/\Delta y_{j-1}\}$$

$$FUZ = \frac{1}{4}\{[(W_{i,j,k}+W_{i+1,j,k})*(U_{i,j,k}+U_{i,j,k+1}) + \overline{\alpha}\ |W_{i,j,k}+W_{i+1,j,k}|*(U_{i,j,k}-U_{i,j,k+1})]/\Delta z_k \quad (2.12)$$
$$-[(W_{i,j,k-1}+W_{i+1,j,k-1})*(U_{i,j,k-1}+U_{i,j,k}) + \overline{\alpha}\ |W_{i,j,k-1}+W_{i+1,j,k-1}|*(U_{i,j,k-1}-U_{i,j,k})]/\Delta z_{k-1}\}$$

Where $\overline{\alpha}$ is a coefficient which determines the amount of upstream or donor cell differencing, and should be based on the time step, grid spacing and velocity. More specifically, $\overline{\alpha}$ should be about 1.5 times larger than the maximum value of

$$\left|\frac{U\Delta t}{\Delta x}\right|, \left|\frac{V\Delta t}{\Delta y}\right|, \text{or } \left|\frac{W\Delta t}{\Delta z}\right|$$

according to Hirt, Nichols, and Romero [1975].

Equations (2.10)-(2.12) are the convective flux terms used to obtain the time advanced U velocity. The velocity equations for the other two components, viscous flux equations, and convective flux equations are similar to the U velocity equations and are included in the Appendix.

The finite difference representation for equation (2.7) is solved for the turbulent time advanced value just as the laminar equation (2.8).

$$U_{i,j,k}^{new} = U_{i,j,k}^{old} + \Delta t\left[\frac{P_{i,j,k} - P_{i+1,j,k}}{\Delta x_i} + g_x + GAMMAX - FUX - FUY - FUZ\right] \qquad (2.13)$$

The equation for GAMMAX is as follows.

$$\Gamma_x = \nu_t\left[2\frac{\partial^2 U}{\partial x^2} + \frac{\partial^2 U}{\partial y^2} + \frac{\partial^2 U}{\partial z^2} + \frac{\partial^2 V}{\partial x \partial y} + \frac{\partial^2 W}{\partial x \partial z}\right] + 2\frac{\partial \nu_t}{\partial x}\left[\frac{\partial U}{\partial x}\right] \qquad (2.14)$$

$$+\frac{\partial \nu_t}{\partial y}\left[\frac{\partial U}{\partial y} + \frac{\partial V}{\partial x}\right] + \frac{\partial \nu_t}{\partial z}\left[\frac{\partial U}{\partial z} + \frac{\partial W}{\partial x}\right] - \frac{2}{3}\frac{\partial k}{\partial x}$$

2.3.3 Scalar Equations

The equation structure for scalar quantities such as temperature, mixture fraction, turbulent kinetic energy, and turbulent dissipation is very similar to the previously outlined momentum equations. The turbulent kinetic energy equation and the turbulent energy dissipation equation will be discussed in detail in the next sections. The temperature equation is presented here. The finite difference program used in this study is capable of performing concentration analysis, but the mixture concentration results are not included in this analysis. Because the form of the mixture concentration equation is identical to the temperature equation, and mixture concentration results are not involved in this study, the mixture concentration equation will be presented in the Appendix.

$$\frac{\partial T}{\partial t} + \frac{\partial}{\partial x_i}\left(U_i T\right) = \alpha\left(\nabla^2 T\right) \tag{2.15}$$

Equation (2.15) is the heat transport equation used throughout the three dimensional domain for laminar and turbulent solution procedures.

The heat transport finite difference equation and the other scalar finite difference equations are derived in the same manner as the velocity component time advanced finite difference equations. The time advanced finite difference form of the heat transport equation is:

$$T_{i,j,k}^{new} = T_{i,j,k}^{old} + \Delta t\left[\,VIST - FTX - FTY - FTZ\,\right] \tag{2.16}$$

where

$$VIST = \alpha \left[\left(\frac{T_{i+1,j,k} - T_{i,j,k}}{\Delta x_i} - \frac{T_{i,j,k} - T_{i-1,j,k}}{\Delta x_{i-1}} \right) \Big/ \Delta x_{ci} \right. \tag{2.17}$$

$$+ \left(\frac{T_{i,j+1,k} - T_{i,j,k}}{\Delta y_j} - \frac{T_{i,j,k} - T_{i,j-1,k}}{\Delta y_{j-1}} \right) \Big/ \Delta y_{cj}$$

$$\left. + \left(\frac{T_{i,j,k+1} - T_{i,j,k}}{\Delta z_k} - \frac{T_{i,j,k} - T_{i,j,k-1}}{\Delta z_{k-1}} \right) \Big/ \Delta z_{ck} \right]$$

In equation (2.16), α is the thermal diffusivity of air.

The convective flux terms are:

$$FTX = \frac{1}{2} \{ [U_{i,j,k}(T_{i,j,k}+T_{i+1,j,k}) + \overline{\alpha}\ |U_{i,j,k}|*(T_{i,j,k}-T_{i+1,j,k})]/\Delta x_i \tag{2.18}$$

$$-[(U_{i-1,j,k}(T_{i-1,j,k}+T_{i,j,k}) + \overline{\alpha}\ |U_{i-1,j,k}|*(T_{i-1,j,k}-T_{i,j,k})]/\Delta x_{i-1} \}$$

$$FTY = \frac{1}{2} \{ [V_{i,j,k}(T_{i,j,k}+T_{i,j+1,k}) + \overline{\alpha}\ |V_{i,j,k}|*(T_{i,j,k}-T_{i,j+1,k})]/\Delta y_j \tag{2.19}$$

$$-[(V_{i,j-1,k}(T_{i,j-1,k}+T_{i,j,k}) + \overline{\alpha}\ |V_{i,j-1,k}|*(T_{i,j-1,k}-T_{i,j,k})]/\Delta y_{j-1} \}$$

$$FTZ = \frac{1}{2} \{ [W_{i,j,k}(T_{i,j,k}+T_{i,j,k+1}) + \overline{\alpha}\ |W_{i,j,k}|*(T_{i,j,k}-T_{i,j,k+1})]/\Delta z_k \tag{2.20}$$

$$-[(W_{i,j,k-1}(T_{i,j,k-1}+T_{i,j,k}) + \overline{\alpha}\ |W_{i,j,k-1}|*(T_{i,j,k-1}-T_{i,j,k})]/\Delta z_{k-1} \}$$

2.3.4 Turbulent Kinetic Energy Equation

For additional turbulence theory which is not included in this report, one should examine Hinze [1987], and for a through discussion of turbulence k-ε modeling consult Rodi [1980]. For an overview of turbulence theory, turbulent k-ε modeling, and more about how they apply to this project, see Weathers [1992]. All of these references discuss the nature of turbulence, turbulent properties, and the closure problem encountered in modeling. The turbulence model used in this research is a two-equation, k-ε model with the option of using wall functions or a low-Reynolds number algorithm. It should be noted that the k-ε model is not the best predictor of turbulent flow, and it has its limitations. For the scope of this project the k-ε model has been chosen, but future studies will probably want to use a more detailed, complex model.

The turbulent kinetic energy equation is given below.

$$\frac{\partial k}{\partial t} + \frac{\partial}{\partial x_j}(U_j k) = \frac{\partial}{\partial x_j}\left[\frac{\nu_t \partial k}{\sigma_k \partial x_j}\right] + \nu_t \frac{\partial U_i}{\partial x_j}\left[\frac{\partial U_i}{\partial x_j} + \frac{\partial U_j}{\partial x_i}\right] - \varepsilon \qquad (2.21)$$

where σ_k is an empirical constant, and is usually set equal to 1.0.

For this study, terms Θ and Π are defined as:

$$\Theta(k) = \frac{\partial}{\partial x_j}\left[\frac{\nu_t \partial k}{\sigma_k \partial x_j}\right] \qquad (2.22)$$

$$\Pi = \frac{\partial U_i}{\partial x_j}\left[\frac{\partial U_i}{\partial x_j} + \frac{\partial U_j}{\partial x_i}\right] \qquad (2.23)$$

Previous equations (2.22) and (2.23) can be substituted into equation (2.21) for simplification.

The finite difference equation for the turbulent kinetic energy time advanced values is:

$$k_{i,j,k}^{new} = k_{i,j,k}^{old} + \Delta t\left[THETAK + \nu_t \cdot PI - FKX - FKY - FKZ - \varepsilon \right] \qquad (2.24)$$

The finite difference terms for the convective fluxes, Θ, and Π are in the Appendix.

2.3.5 Turbulent Dissipation Equation

The ε equation, using the Θ function and Π term, can be written as follows.

$$\frac{\partial \varepsilon}{\partial t} + \frac{\partial}{\partial x_j}(U_j \varepsilon) = \Theta(\varepsilon) + \frac{\nu_t C_1 F_1 \varepsilon}{k}\Pi - C_2 F_2 \frac{\varepsilon^2}{k} + E \qquad (2.25)$$

And the time advanced finite difference equation, which is again similar in form to all the other time advanced equations, is given below. Also, the flux terms can be found in the Appendix.

$$\varepsilon_{i,j,k}^{new} = \varepsilon_{i,j,k}^{old} + \Delta t\left[THETAE + \frac{\nu_t C_1 F_1 \varepsilon}{k} PI - C_2 F_2 \frac{\varepsilon^2}{k} - FEX - FEY - FEZ + E \right] \qquad (2.26)$$

2.4 Boundary Conditions

The value of the three velocity components, temperature, kinetic energy, and dissipation at the boundaries must be specified with some degree of accuracy in order to achieve an accurate solution. This section discusses the boundary conditions used at the solid walls, at the inlet and at the outlet. Of course for the laminar case, the turbulent kinetic energy and the turbulent dissipation do not need to be specified because they do not affect a laminar solution.

2.4.1 Wall Boundary Conditions

The boundary conditions at the walls have evolved along with turbulence modeling. Wall boundary conditions are also an area of CFD methodology which causes much discussion among researchers. The main difference between different types of two-equation turbulence models is often the way in which the boundary conditions are imposed at the wall. Many researchers have used k-ε turbulence models with both a wall function method and a low-Reynolds number model. These are generally recognized as the two main types of k-ε models.

The code used in this study has the capacity to obtain solutions through a laminar, turbulent wall function, or a low-Reynolds number algorithm. With that in mind, the boundary conditions involved in the wall function and low-Reynolds number model are noted here. More details about each of these turbulent solution methods will be presented in a later section.

All walls in the room are non-porous. Therefore the normal velocity, U_n, is always equal to zero. The classical no slip and free slip conditions can be imposed as follows.

No Slip: $U_t = 0$

Free Slip: $$\frac{\partial U_t}{\partial x_n} = 0$$

where U_t = velocity of the fluid tangential to the wall

So, when the no slip condition is in effect, the fluid near the wall does not "slip". While the free slip, or slip, condition is in effect, the fluid is free to move along the wall. Usually, in CFD modeling, the no slip boundary condition is imposed when nodes exist inside the boundary layer, but if the grid size is larger than the boundary layer thickness, then the slip condition should yield better results.

2.4.1.1 Wall Function Boundary Conditions

Because of problems in early CFD modeling, many variations of the k-ε model were devised. Launder and Spalding [1974] devised a model which produced dependable results at a significant distance away from the wall. In order to extend their model to include the wall region, they developed wall functions. Since the wall function was first introduced, there have been many changes by researchers with different applications. The wall functions used in this project come from Murakami [1989a,b, & 1990]. It should be noted that when the wall function method is used, the previously mentioned slip and no-slip conditions are replaced by the following equation.

$$\left.\frac{\partial U}{\partial x_n}\right|_{wall} = \frac{m U_t}{y_n} \tag{2.27}$$

where m = a constant (usually 1/7)
y_n = the normal distance from the boundary to the first velocity vector defined inside the boundary
U_t = the value of the first tangential velocity vector inside the boundary

The wall function boundary conditions are used only with the turbulent wall function k-ε model. The laminar and turbulent low-Reynolds number k-ε models use either the slip or no slip conditions.

According to [Murakami, et. al., 1989a,b] the value of the dissipation at the boundary when wall functions are used can be defined as

$$\varepsilon = \frac{(C_\mu^{0.5} k)^{1.5}}{\kappa y_n} \tag{2.28}$$

The turbulent kinetic energy wall boundary condition can be imposed as:

$$\frac{\partial k}{\partial x_n} = 0 \tag{2.29}$$

2.4.1.2 Low-Reynolds Number Boundary Conditions

A different type of k-ε turbulence model which does not use wall functions is the low-Reynolds number model. The low-Reynolds number model, as its name suggests, is

generally not valid for high Reynolds number flows. According to Lam and Bremhorst [1981] the boundary condition at the wall for the turbulent dissipation when using the low-Reynolds number model can be imposed as:

$$\frac{\partial \varepsilon}{\partial x_n} = 0 \tag{2.30}$$

It should be noted that, when using the low-Reynolds number k-ε model, the turbulent kinetic energy wall boundary condition is the same as the boundary condition imposed in the wall function k-ε analysis.

When one uses the turbulent low-Reynolds number model, either the slip or no slip conditions are used, as mentioned earlier. If the no slip condition is used, then fundamentally this means that the user expects to predict the flow within the boundary layer. In order to predict the behavior of the boundary layer flow, one must know the thickness of the boundary layer and implement a grid with nodes close enough to the wall to be included inside the boundary layer. Conversely, if one uses the slip boundary condition, then the boundary layer information is not obtained or predicted because the size of the cell at the wall is larger than the thickness of the boundary layer. In this study and in Weathers' thesis, the slip boundary condition is used in the low-Reynolds number model simulations.

2.4.1.3 Wall Temperature Boundary Conditions

The temperature boundary conditions were varied for different cases because one of the objectives of this study is to investigate the feasibility of predicting the outlet temperature and/or the convection coefficient. Three different temperature boundary conditions were used in this analysis. The first type of boundary condition simply sets the temperature of the node just outside the boundary equal to the wall temperature, 30°C. In Figure 2.4, $T_1 = 30°C$.

The second type of boundary condition is slightly more complex than the first boundary condition. Ideally, the wall temperature would be set to 30°C in order to match the experimental experiments. Therefore, this boundary condition sets the temperature of the node just outside the boundary based on the temperature of the temperature just inside the boundary such that the temperature at the wall is maintained at a specified constant value. The equation for this boundary condition is as follows.

$$T_1 = 2*T_{wall} - T_2 \tag{2.31}$$

where T_{wall} = Temperature of the boundary
T_1 = Temperature of the node just outside the boundary
T_2 = Temperature of the node just inside the boundary

Figure 2.4 shows the location of T_1, T_2 and T_{wall}. Equation (2.31) was developed because scalar quantities in this program are not defined at the boundaries, but at one half cell outside and inside of the boundary, as discussed earlier. Therefore, even though T_{wall} is a constant value which is specified, it is up to the previous equation and the values of T_1 and T_2 to maintain a linear temperature gradient across the boundary and the effective wall temperature at a constant value.

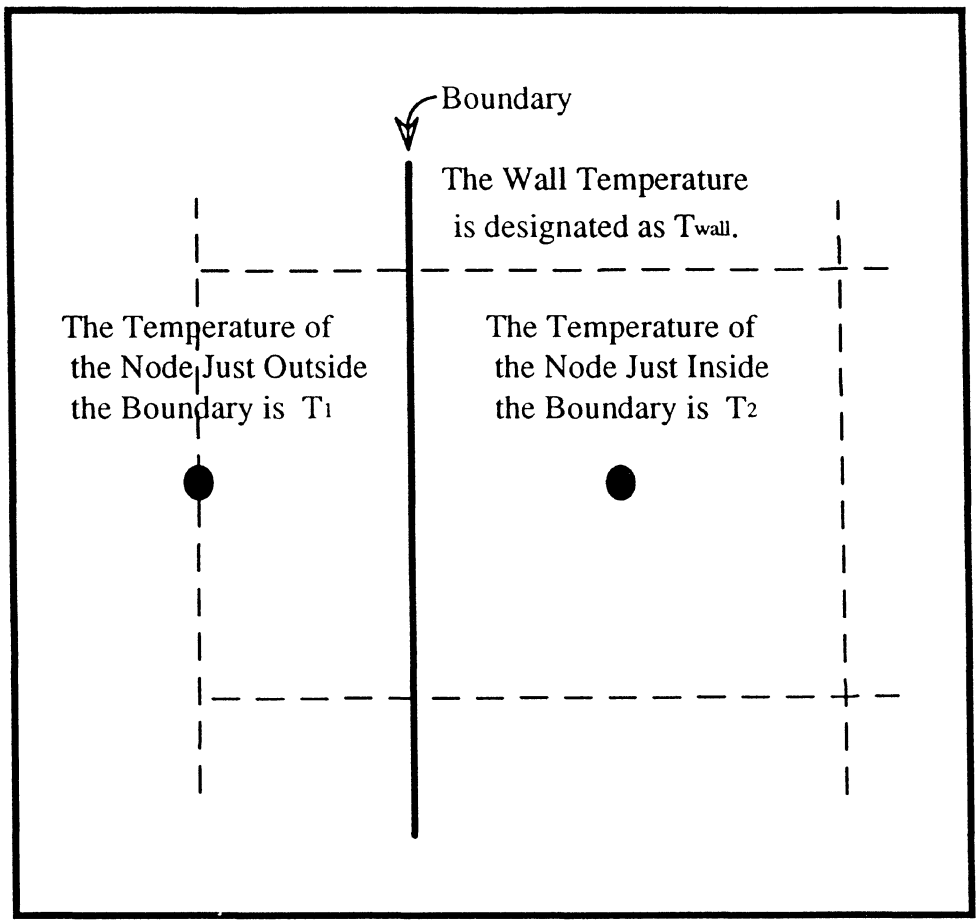

Figure 2.4 Temperature Designations and Locations

The third type of temperature boundary condition used at the wall is based on a heat balance of the boundary:

$$k\frac{\partial T}{\partial x_i} = h_c(T_{ref} - T_{wall}) \tag{2.32}$$

where k = Thermal conductivity

h_c = Experimental convection coefficient

T_{ref} = Reference temperature (see Spitler 1990)

For this study, the reference temperature is defined as the temperature at the outlet. The heat conduction through the wall is equal to the heat convection away from the wall. This heat balance with convection involved utilizes a known heat transfer coefficient. Therefore, this type of boundary condition requires prior knowledge of the convection coefficient and cannot be used to predict the convection coefficient.

The experimental values of the convection coefficients from Spitler [1990] were used in conjunction with this boundary condition. A separate convection coefficient is used for the floor, ceiling, and the four walls. The equations which yield the experimental convection coefficients for a wall inlet situation are taken from page 133 of Spitler's 1990 doctoral thesis and are given below.

For $0.002 < J < 0.011$

Walls: $h = 0.6 + 63.1\ J^{0.4}$ (2.33)

Ceiling: $h = -0.4 + 43.2\ J^{0.4}$ (2.34)

Floor: $h = 2.5 + 32.1\ J^{0.4}$ (2.35)

where J is the jet momentum number which can be calculated as follows:

$$J = ACH * U_{in} / g \quad (2.36)$$

ACH = the number of air changes per hour

The values for the convection coefficients used in this analysis are given in the following table.

TABLE 2.1

CONVECTION COEFFICIENT EXPERIMENTAL VALUES

ACH:	15	50	100
Walls:	2.448 (W/m^2 °C)	6.249 (W/m^2 °C)	10.018 (W/m^2 °C)
Ceiling:	3.440 (W/m^2 °C)	5.374 (W/m^2 °C)	7.291 (W/m^2 °C)
Floors:	1.225 (W/m^2 °C)	3.828 (W/m^2 °C)	6.408 (W/m^2 °C)

2.4.2 Inlet Boundary Conditions

Inlet boundary conditions for a room airflow model are also important in obtaining an accurate solution as demonstrated by Weathers [1992]. First, he used uniform velocity profiles which set the u velocity component at every inlet cell equal to a constant value. Later he studied the experimental data and found that the experimental inlet jet was not uniform. Using the experimental data as a guide, he approximated inlet velocity profiles and used them as inputs into the CFD program rather than the uniform velocity profiles. He found that the approximated inlet profiles produced results which matched the experimental data better than the uniform velocity profiles. The uniform and approximated velocity profiles for the normal velocity are summarized in the following table where h is the height of the inlet.

TABLE 2.2

INLET BOUNDARY CONDITION FOR U-NORMAL
[Weathers, 1992]

Flow Rate (ACH)	Uniform Profile (m/s)	Inlet Approximation (m/s)
15	0.345	0.690 $(0 < y < h/2)$ 0.000 $(h/2 < y < h)$
50	1.150	$1.1 + \frac{8y}{5h}$ $(0 < y < h/4)$ 1.5 $(h/4 < y < 3h/4)$ $2.7 - \frac{8y}{5h}$ $(3h/4 < y < h)$
100	2.300	$2.35 + \frac{8y}{5h}$ $(0 < y < h/4)$ 2.75 $(h/4 < y < 3h/4)$ $3.95 - \frac{8y}{5h}$ $(3h/4 < y < h)$

For a graphical representation of the inlet profile information of Table 2.2, see Weathers [1992]. The tangential velocity at the inlet is zero. The inlet temperature is specified, and equations (1.12) & (1.13) which have been taken from Awbi [1989] are used to obtain a value for k and ε at the inlet.

As mentioned earlier, the inlet for this project is 0.4 m. wide by 0.9 m. high. It is located on the sidewall approximately halfway between the ceiling and the floor (see Figure 1.1). Across the inlet there are 8 nodes in the y direction and 4 nodes in the z direction.

2.4.3 Outlet Boundary Conditions

Compared to the boundary conditions imposed at the walls and the inlet, the outlet boundary conditions are relatively simple. The equation used to calculate the normal u-velocity at the outlet is:

$$U_n = U_{in} \frac{A_{in}}{A_{out}} \tag{2.37}$$

When the areas of the inlet and outlet are both equal, the inlet velocity and outlet velocity are both equal. It should be noted that there are a few cases in this study when a variable grid is used and it is not possible to use an inlet area that is exactly equal to the outlet area. Again, the tangential velocity at the outlet is zero, just like the inlet condition.

The temperature, turbulent kinetic energy and turbulent dissipation of the fictitious nodes just outside the boundary at the outlet are each set equal to the appropriate values just inside the boundary. Therefore,

$$\frac{\partial T}{\partial x_n} = 0, \quad \frac{\partial k}{\partial x_n} = 0, \quad \text{and} \quad \frac{\partial \varepsilon}{\partial x_n} = 0. \tag{2.38}$$

2.4.4 Initial Conditions

It is rather simple to set the initial values of the variables throughout the domain, but it is also an important part of the modeling process, especially when performing a turbulent model. The initial values for all three velocity components, the mixture concentration and the pressure at every node inside the domain are set to zero. The initial values for the turbulent kinetic energy and the turbulent dissipation are set to a percentage of the inlet values. The initial temperature value is input by the user and changes with the air flow rate. The following table gives the initial temperature values used in the computational models.

TABLE 2.3

INITIAL TEMPERATURE VALUES (°C)

15 ACH	30 ACH	50 ACH	100 ACH
28.5	26.5	25.5	24.75

The above values were obtained from experimental results presented in Spitler's 1990 thesis on page 93.

2.5 Turbulence Models

There are many different types of turbulence models which have been developed by a number of researchers for a wide range of fluid dynamic applications. As mentioned earlier, there is an option in the computer program which allows the user to perform a

laminar simulation, a turbulent k-ε simulation using wall functions or a low-Reynolds number turbulent k-ε simulation. For each of the k-ε turbulent simulations, there exists empirical constants and functions which distinguish the different types of turbulence models.

Equations for the Local Reynolds Number (R_y) and Turbulent Reynolds Number (R_T), which are used with the low-Reynolds number model, are given below.

$$R_y = \frac{\sqrt{k\, y_n}}{\nu} \tag{2.39}$$

$$R_T = \frac{k^2}{\nu\, \varepsilon} \tag{2.40}$$

where y_n = the normal distance to the wall (m).

Constants for the standard, or wall function, k-ε model and the low-Reynolds number model used in this research are given below in Table 2.4.

TABLE 2.4

CONSTANTS USED IN TURBULENCE MODELING

C_μ	C_1	C_2	σ_k	σ_ε
0.09	1.44	1.92	1.0	1.3

The following table gives the empirical functions which have been used in this study for the standard k-ε model and the low Reynolds number k-ε model.

TABLE 2.5

FUNCTIONS USED IN TURBULENCE MODELING

Model Type	$F\mu$	F_1	F_2	E
Standard	1.0	1.0	1.0	0.0
Low-Reynolds Number	$\left(1 - e^{-(A_\mu R_y)}\right)^2 * \left(1 + \frac{A_t}{R_T}\right)$	$1 + \left(\frac{0.05}{F_\mu}\right)^3$	$1 - e^{(-(R_T^2))}$	0.0

As stated earlier, for more information about various turbulent constants and functions which have been used by other researchers, consult Weathers' [1992] thesis.

2.6 Grid Resolution

The uniform grid used in this study is equivalent to the 40 x 24 x 24 "very fine" grid used by Weathers [1992]. The variable grid used in this thesis is 41 x 25 x 25 and is only slightly non-uniform. It expands linearly from the edges to the center. In other words, the largest cell is the center cell, and the smallest cells are the first and the last cells. In the x direction the smallest cell is 10.04 cm. and the center cell is 12.45 cm. The smallest cell in the y and z directions is 10.3 cm. and the center cell is 11.75 cm. Figure 2.5a below shows the non-uniform cell resolution for the x direction in graphical terms. The non-uniform grid resolution in the z and y directions is identical and is displayed in Figure 2.5b.

Ideally, many other variable grids would have been used with a large range of cell sizes, but time limitations did not permit.

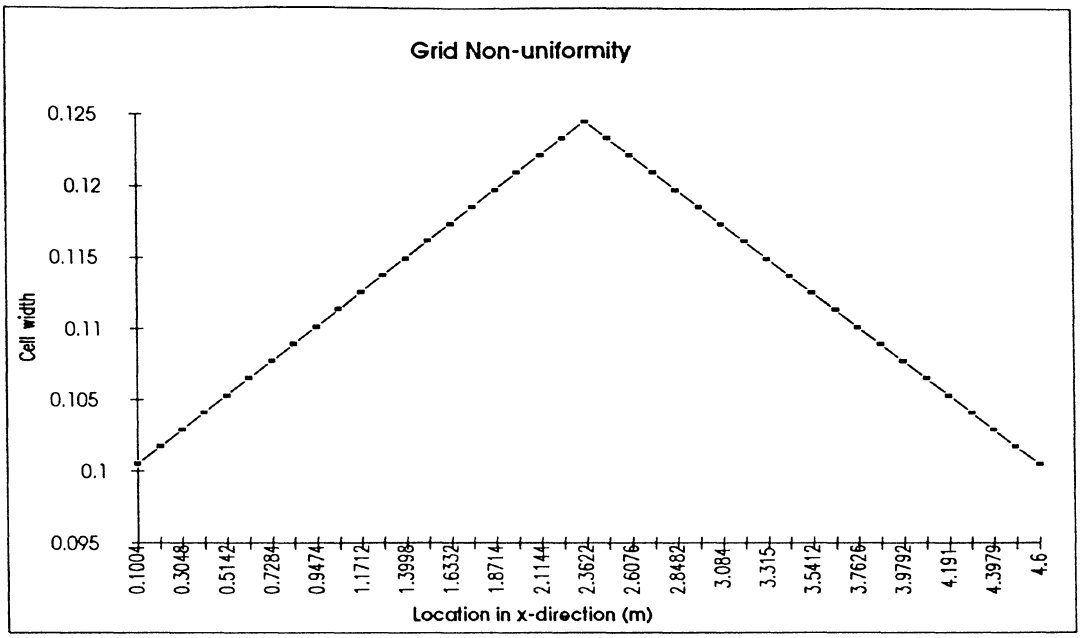

Figure 2.5a Non-Uniform Grid Resolution in the X Direction

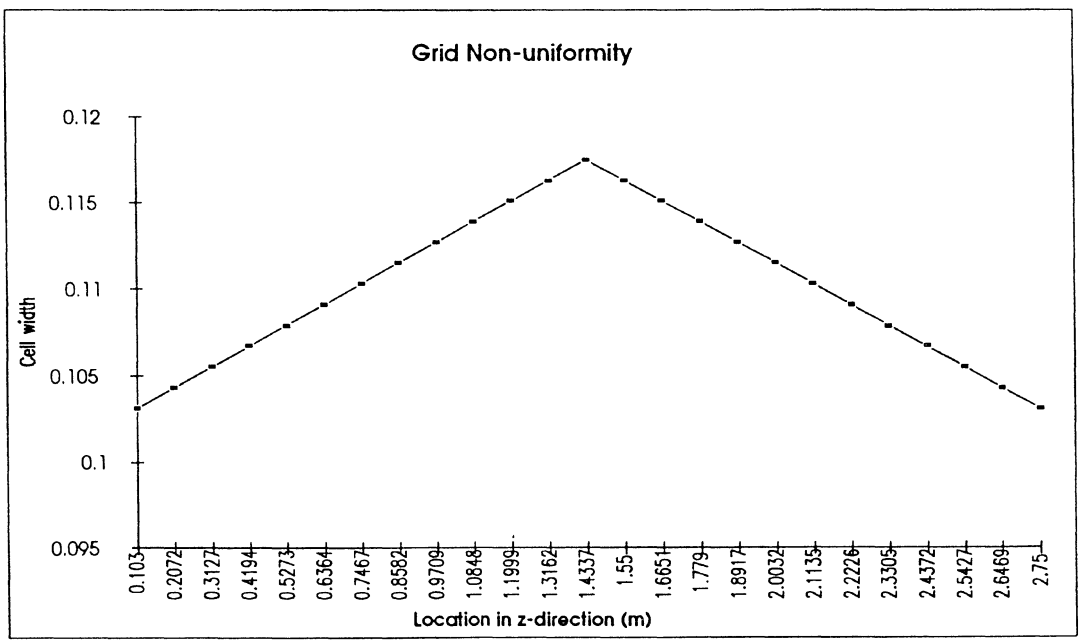

Figure 2.5b Non-Uniform Grid Resolution in the Z (and Y) Directions

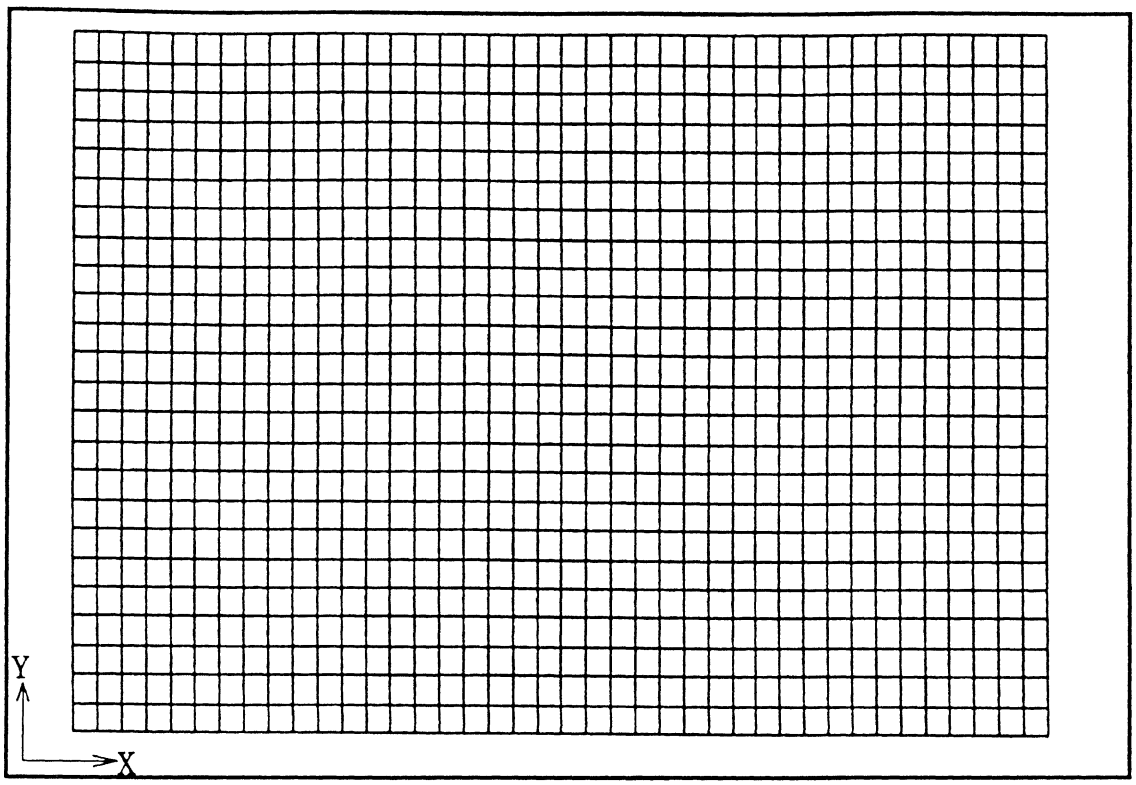

Figure 2.6a Uniform Grid in X and Y Directions

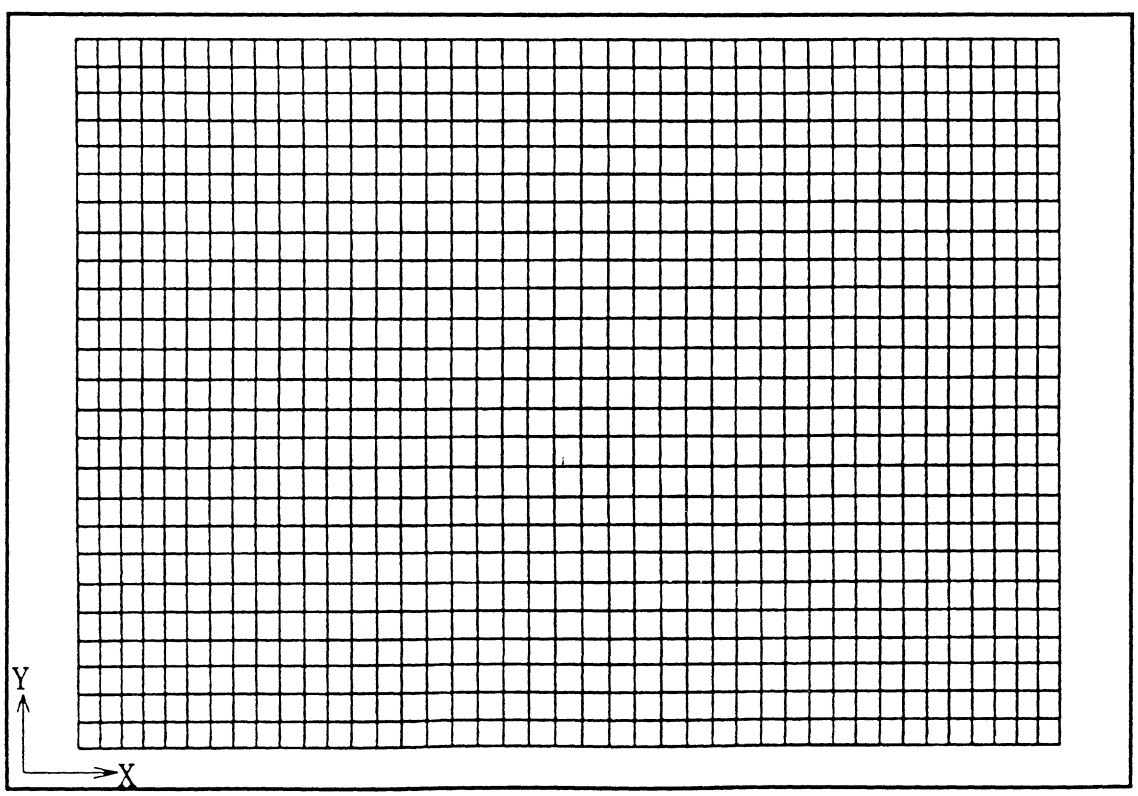

Figure 2.6b Variable Grid in X and Y Directions

Figures 2.6a and 2.6b show uniform and variable grid lines in x and y directions. The third direction (z) is omitted because it is the same as the y direction, as stated previously.

2.7 Error Analysis

Various error numbers were calculated in order to compare the experimental results to the computational results directly and quantitatively. Global velocity, global temperature, and two-dimensional velocity error numbers were used.

2.7.1 Global Error Number

The global error number used in Weathers' study [1992] is also used here for help in quantitatively evaluating the accuracy of the computational velocity results.

$$GEN = \frac{\overline{E}_{abs}}{V_{max}} \tag{2.41}$$

where $\overline{E}_{abs}$ = average absolute error for the velocity.
V_{max} = maximum experimental velocity.

2.7.2 Slice Error Number

A two-dimensional error number was also used in the same manner as the global error number in order to check the accuracy of a specific plane of data. The slice error number can be used to isolate a problem with a "slice" of the domain. The two-dimensional or slice error number is as follows:

$$SEN = \frac{\overline{E}_{abs}}{V_{max}} \tag{2.42}$$

where $\overline{E}_{abs}$ = average absolute error for the velocity.
V_{max} = maximum experimental velocity within the plane being studied.

In this study, the slice error number was mainly used to compare the computational wall jet to the experimental wall jet. Plots at z=0.127 m. and slice error numbers are provided in chapter 3.

2.7.3 Global Temperature Error Number

A quantity similar to the global error number was implemented in this study for the computational temperatures. The global temperature error number is as follows.

$$GTEN = \frac{\overline{E}_{abs}}{(T_{max} - T_{min})} \tag{2.43}$$

where $\overline{E}_{abs}$ = average absolute error for the temperature.
T_{max} = maximum experimental temperature.
T_{min} = minimum experimental temperature.

The global temperature error number was used to determine the appropriate time to make temperature comparisons between the experimental and computational results. An explanation of how the global temperature error number was used is detailed later in chapter 3.

2.7.4 Extrapolation Problem

Weathers encountered a problem in his study because of the statistical package that he used to plot his results, Systat™. Systat™ extrapolated values near the wall for the experimental and numerical results. Because the experimental results are not as dense as the numerical results, the extrapolation problem was magnified in the experimental plots. This extrapolation problem has been eliminated in the present study through the use of a software package which is better suited for displaying transient fluid dynamic data, NCSA Image 3.1.1 [NCSA, 1990]. The NCSA Image software is developed by the National Center for Supercomputing Applications at the University of Illinois at Urbana-Champaign. Weathers' extrapolation problem is most evident with his 15 ACH experimental plot. His plot showed unusually high velocity magnitudes in the center of the plot at the floor which is inconsistent with the experimental data. NCSA Image generates correct velocity magnitudes, as shown through the comparison made with Figure 2.7, and remedies the extrapolation problem.

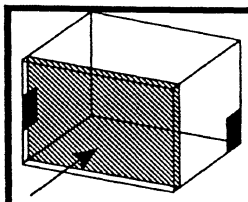

Software Comparison - (Experimental 15 ACH Results)

Section at Z= 0.127m.

Systat™

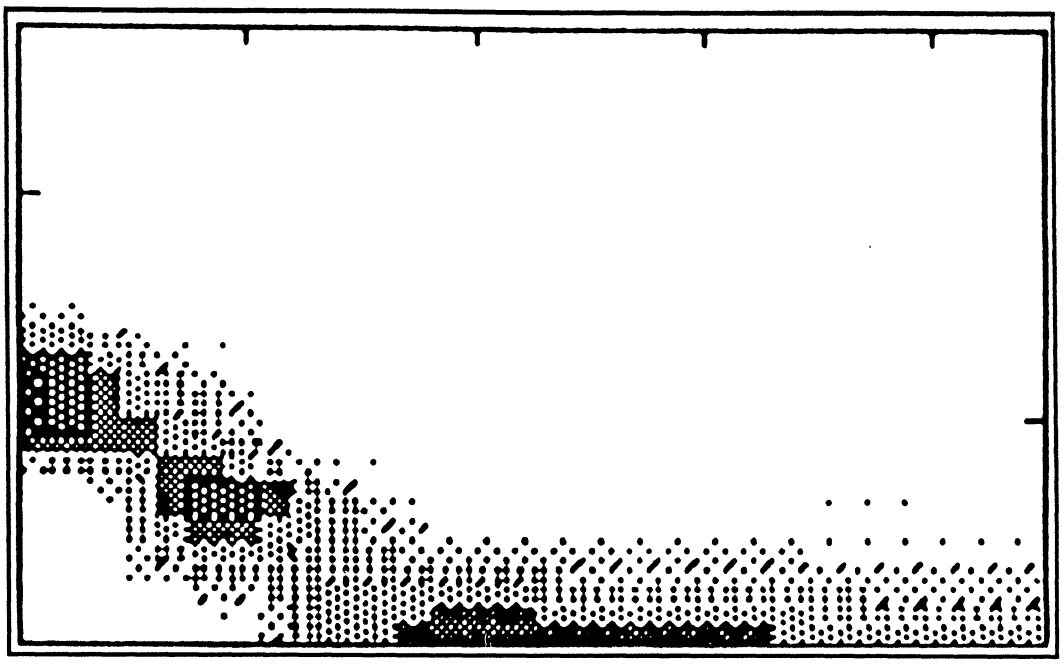

NCSA Image 3.1.1

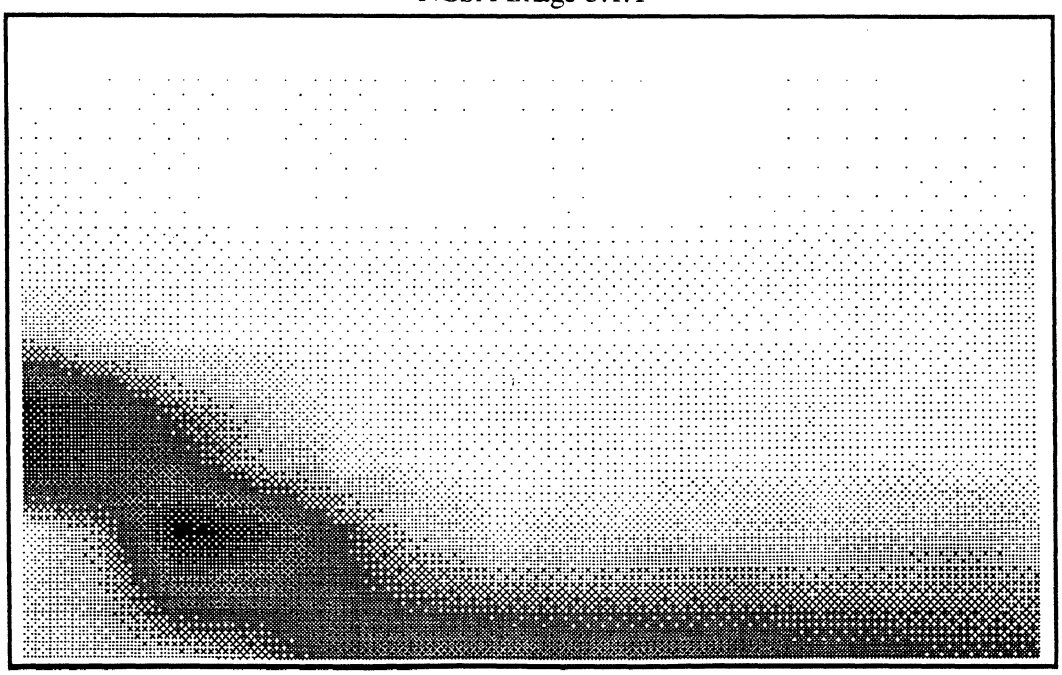

Figure 2.7 Software Comparison: Experimental Velocity Magnitudes at 15 ACH

3.0 RESULTS & DISCUSSION

3.1 Overview of Computational Analysis

Many different computational runs were performed at various air flow rates, the vast majority of which were performed at 15, 50, & 100 ACH. Three different temperature boundary conditions were investigated in order to improve the prediction of heat transfer. A variable grid was implemented in an attempt for better grid coverage and more accuracy at the inlet and outlet.

Section 3.2 discusses the importance of correctly recognizing convergence and stability concerns. In section 3.3, simulations made to investigate the feasibility of predicting convection heat transfer will be presented. Then, in section 3.4 simulation results will be discussed and converged plots will be shown. Finally, sections 3.4.4 and 3.4.5 include quantitative comparisons involving error numbers.

3.2 Convergence & Stability

Before specific, detailed results of this project are provided and discussed, it seems appropriate to discuss the more general concepts of convergence and stability and their importance. During the course of this thesis, it was discovered that convergence should be more carefully considered in each computational case. Prior to this research, the point of convergence probably was not attained. A discussion of convergence follows, and then stability techniques are addressed.

Ideally, the minimum global velocity magnitude error number, the minimum two-dimensional error number, and the minimum global temperature error number would occur simultaneously as the stratification values matched the experimental stratification values and the velocities converge. Unfortunately, most of these indications of convergence occur at different points in the transient solution process. Therefore, for any given computational case, it is difficult to determine the actual point of convergence.

If one bases convergence solely on the point in the computational simulation when velocity magnitudes are no longer changing significantly, then the 100 ACH models converge on average after 100 seconds of simulation. It should be made clear that the times reported here are not CPU times, and that actual run times of the simulations are much, much greater. The velocity components of the 50 ACH models converge at about 250 seconds of simulation, and the 15 ACH models require almost 500 seconds. All simulations were performed out to the times listed above.

The times given above were determined by watching transient, animated, color, computational simulations using NCSA Image 3.1.1 [1990]. The visualization tools were used in this project to help to determine the point of convergence. Prior quantitative techniques failed to require the simulations to run until convergence. With the older and less sophisticated visualization techniques, it was nearly impossible to recognize that convergence had not been achieved. Eventually, one should return to the quantitative techniques once stricter, proven convergence criteria has been defined.

In order to demonstrate the process of convergence, transient plots are included in this section. Discussion is provided in an attempt to present a larger portion of the transient effect, but it is difficult to do the transient color animation, which the plots were taken from, justice. Plots were chosen at the 25, 35, 70 and 100 second intervals of the 50

ACH low Reynolds number variable grid model. The grid resolution is shown in Figures 2.5a and 2.5b. Later in section 3.3, the convergence question is approached from a different angle with the use of the global temperature error number. There the global temperature error number is monitored over time in order to determine when the computational temperatures best match the experimental temperatures.

First in the transient simulation, the effect of buoyancy is demonstrated as the wall jet enters the room and attaches itself to the floor. As the flow hits the opposing wall, it is forced upward towards the ceiling. Once it reaches the ceiling, a small recirculation zone is created. This zone begins to occur at about the 20-25 second mark in the solution process. The 25 second plot, in the top half of Figure 3.1, shows this small recirculation pattern in the upper right hand corner.

As the simulation continues two main things happen. 1.) The overall temperatures in the room are decreasing, and the cold inlet jet does not "see" as large a temperature differential which results in a smaller buoyant effect. Therefore, the jet wants to lift off the floor. 2.) The recirculation pattern continues to move along the ceiling back towards the inlet. These two effects are shown in the lower half of Figure 3.1, the 35 second plot.

While the wall jet continues to attempt to lift off the floor, the recirculation portion of the flow completes the cycle and reaches the inlet jet. When this happens, the wall jet is physically pushed back down to the floor, at about 40-45 seconds. From 45-70 seconds, the wall jet shape does not change drastically. The 70 second plot is shown in the top half of Figure 3.2.

After the 70 second mark, the strength of the recirculation region trails off, and the wall jet begins to lift off the floor once again. The 100 second plot, in Figure 3.2, shows a wall jet which has already detached from the floor. After the 100 second plot, the jet reattaches to the floor, and begins to climb up the wall again. But this time, the effects are not as pronounced. The airflow patterns continue to change between something similar to the 70 second plot with strong recirculation and back to a profile similar to the 100 second plot with no apparent recirculation. The fluid must go through these cycles and the effects must damp out in order for one to conclude that convergence has been achieved.

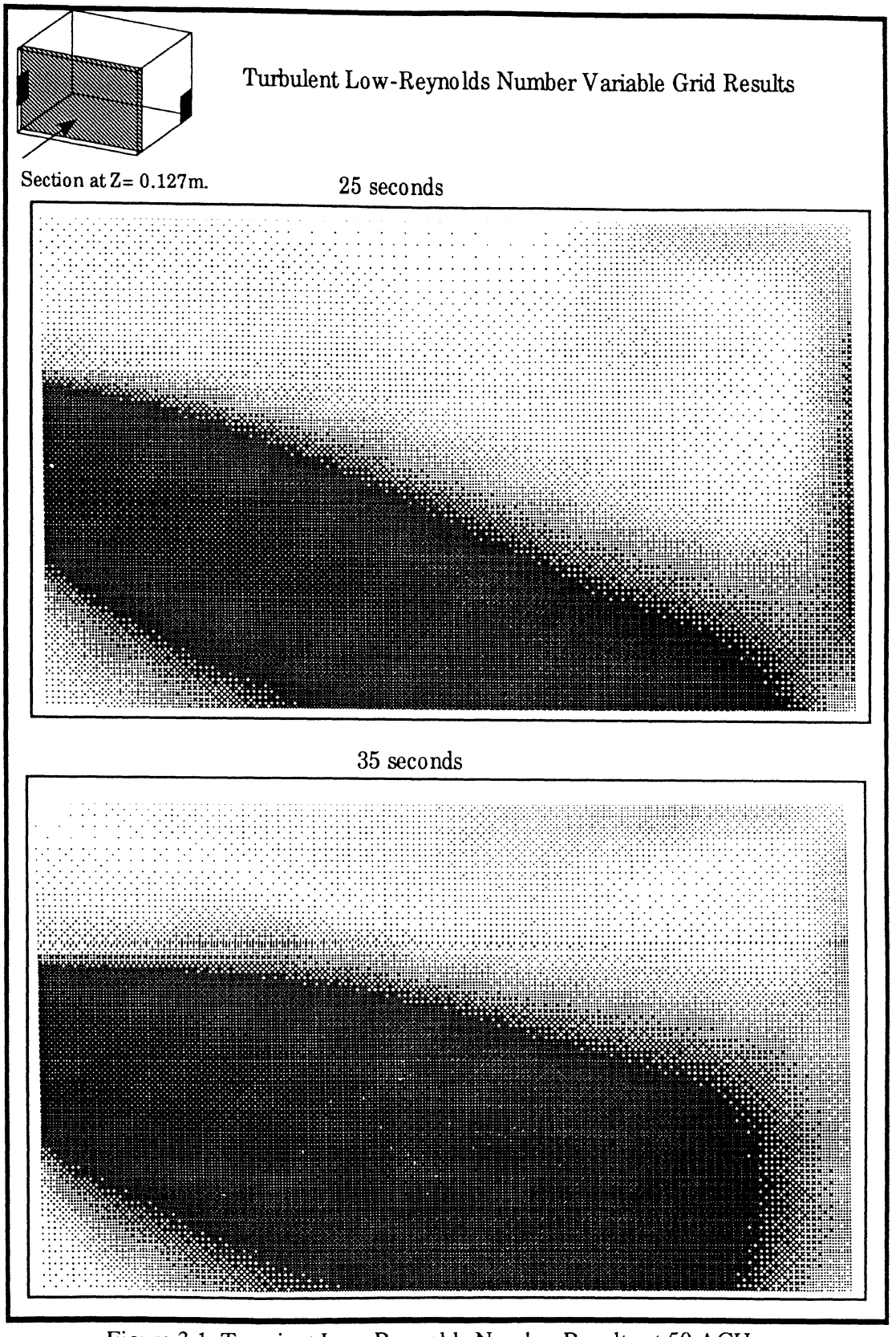

Figure 3.1 Transient Low-Reynolds Number Results at 50 ACH

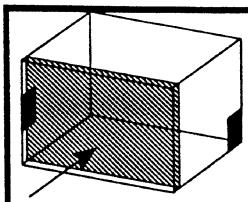

Turbulent Low-Reynolds Number Variable Grid Results

Section at Z= 0.127m.

70 seconds

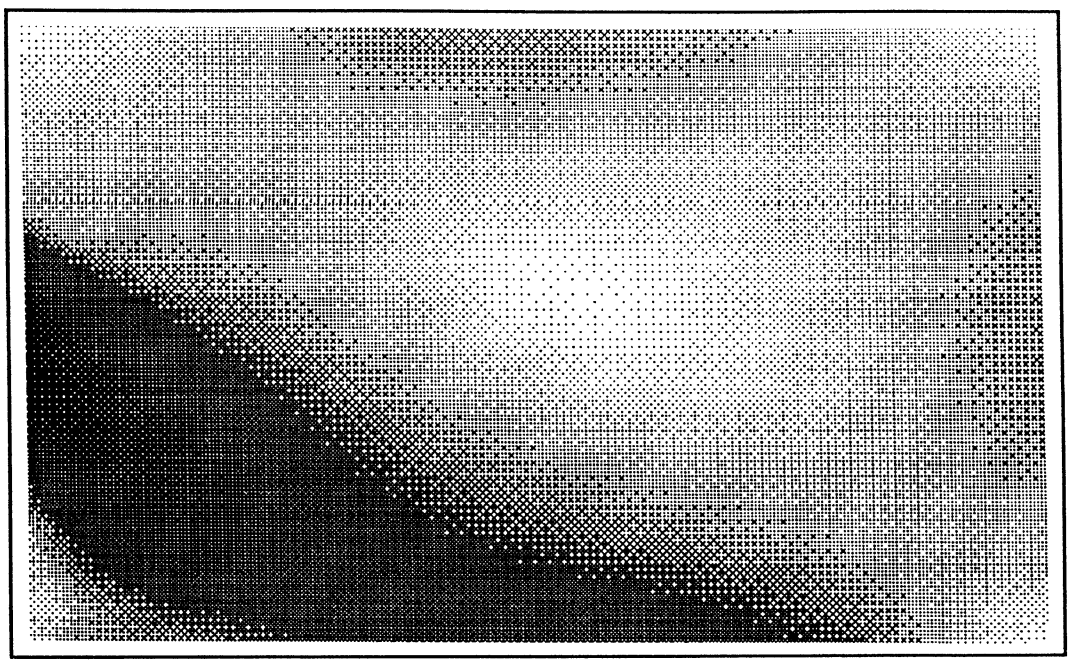

100 seconds

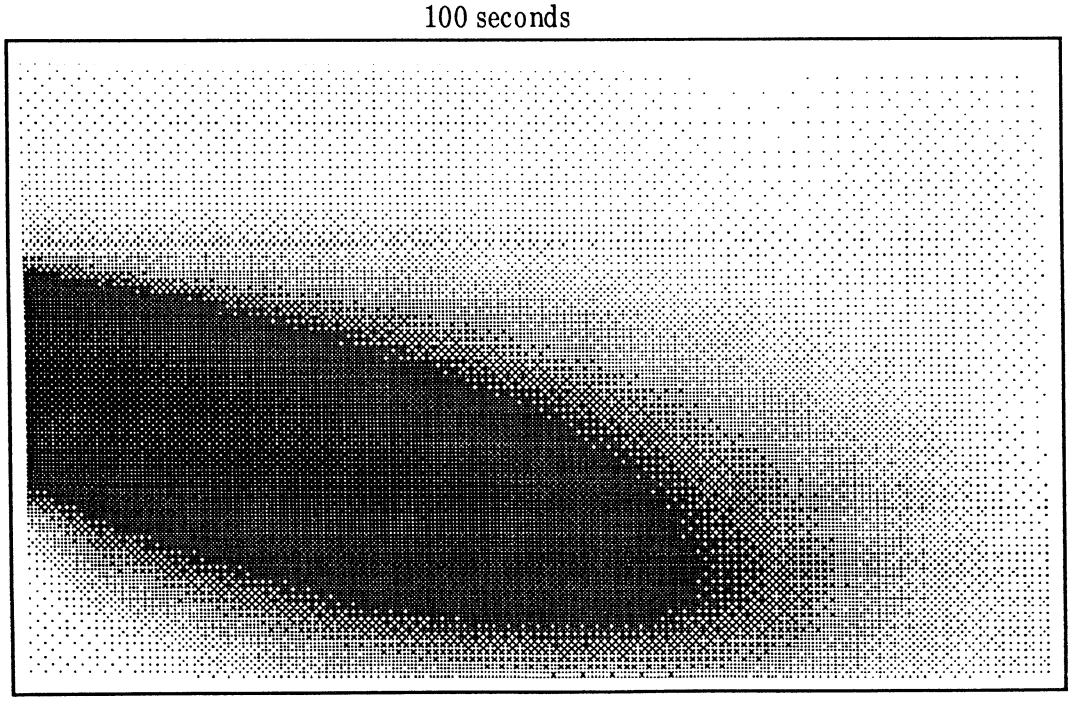

Figure 3.2 Transient Low-Reynolds Number Results at 50 ACH

Stability was a significant problem at the beginning of this study. At the present time, the only model which requires special attention is the 100 ACH low-Reynolds number model. For the 100 ACH low-Reynolds number model, the initial values of turbulent kinetic energy and turbulent dissipation are reduced in order to increase stability and allow the simulation to run. This essentially makes the model less turbulent initially. Awbi [1989] stated that changing the initial or inlet values does not significantly affect the computational results, but changing these values can increase stability. For better stability with the 100 ACH low-Reynolds number model, the initial turbulent dissipation was decreased by 84%, and the turbulent kinetic energy was decreased by 60%.

3.3 Prediction of Temperatures and Convection Coefficients

Different temperature boundary conditions were investigated, as previously discussed. The reason for varying the temperature boundary conditions was to explore the possibility of predicting a convection coefficient which matches the experimental convection coefficient.

Another option was to use the experimentally determined convection coefficients as inputs to the CFD models and monitor the calculated outlet temperature and mean temperatures to see if they matched experimental results.

The results for the laminar simulations made with varying boundary conditions for 50 ACH are shown in Table 3.1. The predicted mean temperatures may be compared to the experimental mean temperature of 25.8°C. The experimental convection coefficient for the wall at z=0.0 m. is 6.249 $W/m^2°C$.

TABLE 3.1

CONVECTION COEFFICIENT AND TEMPERATURE PREDICTION

B. C. Type:	Description	G. E. N.	Mean Temperature	Predicted Convection Coefficient
1	$T_1 = 30°C$	0.06563	21.0° C	17.363
2	$T_1 = 2*T_{wall} - T_2$	0.10234	30.0° C	29.679
3	T_1 uses experimental h_c	0.06559	26.0° C	N/A

Two temperature boundary conditions were used without the experimentally determined convection coefficient. Both are much simpler than the boundary condition which uses experimental convection coefficients. The first temperature boundary condition, referred to as type 1 for clarity, simply sets the temperature just outside the wall equal to the temperature at the wall, 30°C in all CFD cases performed. The global error number for the laminar 50 ACH model using this type 1 boundary condition is slightly higher than the global error number for the laminar 50 ACH model which used the experimental convection coefficient.

The initial temperature throughout the 50 ACH models is 25.5°C, as mentioned earlier. The type 1 boundary condition causes the outlet temperature, and the overall temperature to decrease, and eventually converge at the inlet temperature of 21°C.

The second type of temperature boundary condition used sets the gradient across the boundary such that the temperature at the boundary is held constant at 30°C. The global error number for the laminar 50 ACH model using the type 2 temperature boundary

condition is the highest of the three. This boundary condition causes the temperatures to converge at 30°C, and the high predicted convection coefficient follows.

When one considers the first two temperature boundary conditions, even though the end result is not desirable, the trend is expected. The first temperature boundary condition does not predict enough heat transfer to the room, while the second temperature boundary condition over predicts the heat transfer. Setting the node just outside the boundary equal to the desired temperature at the boundary would actually give the temperature at the boundary a lower temperature than desired. Therefore less heat transfer to the room can be expected in this case. The second temperature boundary condition probably over predicts the heat transferred to the room because if the temperature just inside the wall is not 30°C, then the temperature just outside the boundary is set higher than 30°C. This should set the equivalent temperature at the boundary to 30°C, but the grid size might have hampered its effectiveness. More grid points closer to the wall might help one or both of these two boundary conditions to more accurately predict the convection coefficients.

The temperature boundary condition type 2 is more closely aligned with the physical significance of holding the wall temperature at a constant 30°C throughout the experiment than the type 1 boundary condition which sets the temperature outside the boundary equal to the temperature at the wall. Therefore one might expect that the type 2 boundary condition would produce more favorable results than the type 1 boundary condition. But, the type 2 temperature boundary condition does not produce better results, in terms of global error number analysis or convection coefficient prediction. The higher global error number can be explained when one considers the predicted convection coefficient, predicted outlet temperature, and the stratification plot for the model.

Since temperature boundary condition type 1 caused the temperatures to converge at 21° C and the type 2 boundary condition causes temperature convergence at 30°C, neither is satisfactory. A third type of boundary condition, which uses experimentally determined convection coefficients is preferred. The details of the use of this boundary condition and convection coefficients used were outlined in section 2.4.1.3.

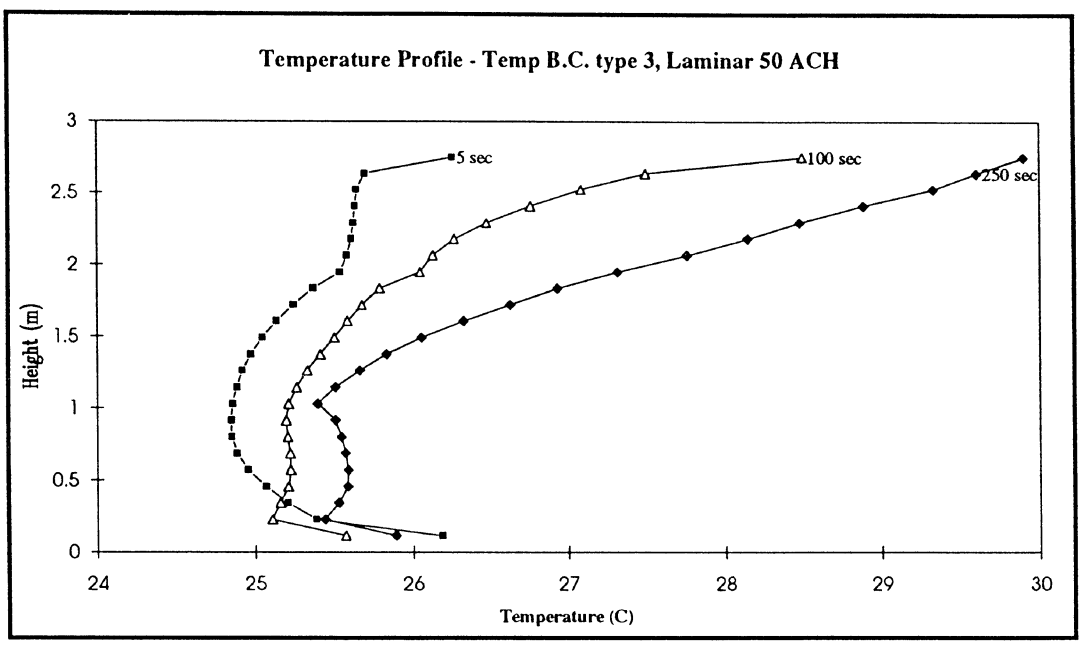

Figure 3.3 Transient Temperature Stratification Values

Each point in Figure 3.3 represents the value calculated by averaging all temperatures at that height in the three-dimensional domain. A comparison to experimental results is shown below. Figure 3.3 shows that the average temperature profile continues to change past 100 seconds, which in the past would have been considered well past the point of convergence. All of the simulations performed included buoyant forces. If the temperatures in these buoyant simulations have not converged, then it is clear that the velocity components also have not converged.

Global temperature error numbers, as opposed to the global velocity magnitude error numbers previously discussed, were calculated for numerous reasons including help in the determination of when to compare the computational and experimental stratification data. The global temperature error numbers for the runs using temperature boundary conditions of type 1 and 2 increased steadily as the transient solution process continued. The global temperature error number for the type 1 temperature boundary condition is 0.333 at 95.0 seconds and continues to increase to 0.497 at 250 seconds. Likewise, the type 2 temperature boundary condition global temperature error number is 0.333 at 64.0 seconds and continues increasing to 250 seconds where the global temperature error number is 0.483.

The global temperature error number for the model using the type 3 temperature boundary condition is more worthy of discussion. Figure 3.4 shows the transient global temperature error number for the laminar 50 ACH model using the type 3 temperature boundary condition.

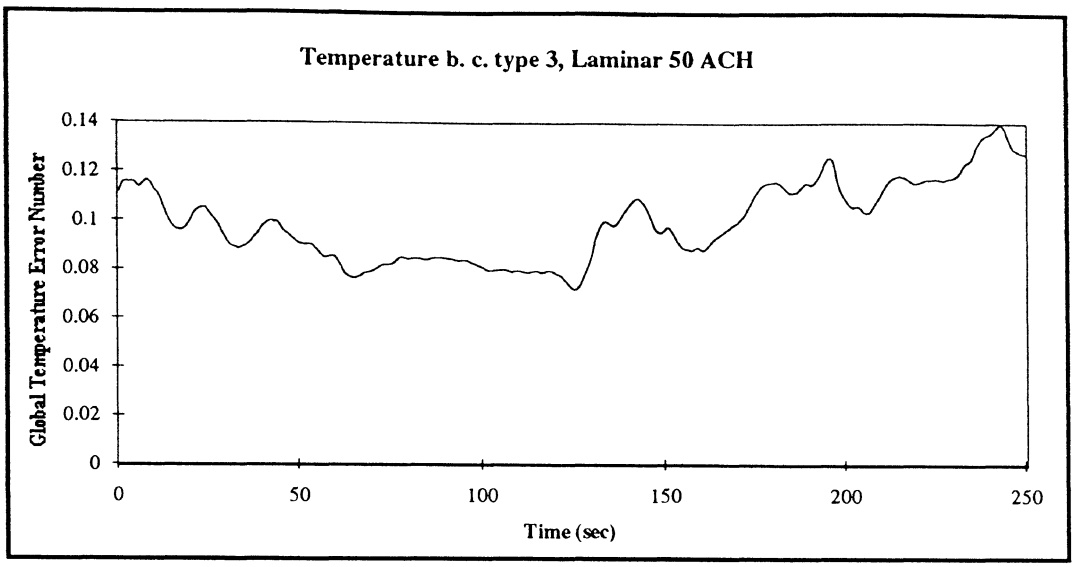

Figure 3.4 Transient Global Temperature Error Number

Note the minimum global temperature error number occurs at 126.0 seconds and is 0.087. Since the minimum global temperature error number in Figure 3.4 occurs at 126 seconds, this time was chosen for comparison of the computational temperatures against the experimental stratification values. Both plots are shown in Figure 3.5.

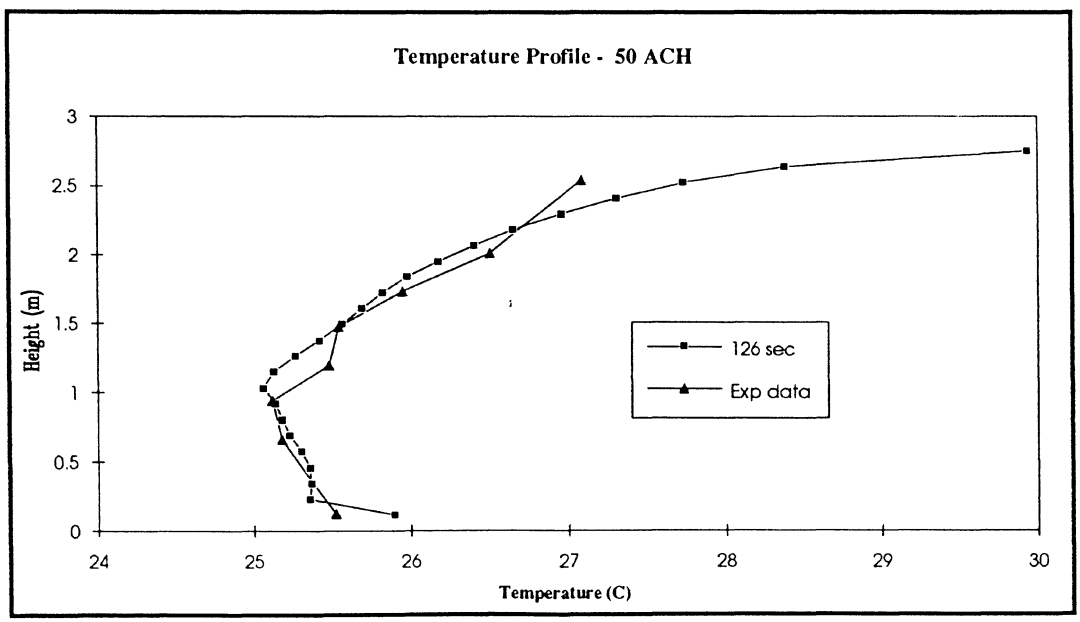

Figure 3.5 Comparison of Computational and Experimental Stratification Values

It was expected that the more complex boundary condition, type 3, which utilized convection coefficients calculated from experimental results, would match those experimental temperatures with greater accuracy than the other two boundary condition types. When one looks at the global error number analysis only, one could conclude that the type 1 boundary condition is a better choice because it produces an adequate global error number without requiring the user to know experimentally determined convection coefficients. But temperature prediction accuracy is also important. The type 3 boundary condition did not converge to either temperature extreme, in fact it matched the experimental stratification with acceptable accuracy as shown in Figure 3.5. It was also a rather good predictor of the temperature at the outlet. Experimental air heat gain values are compared to computational air heat gain values in Figure 3.6. Note that exp designates experimental results, ru designates low Reynolds number unifrom grid results, and rv designates low Reynolds number variable grid results. Figure 3.6 shows that the low Reynolds number model usually predicted air heat gain values lower than the experimental results.

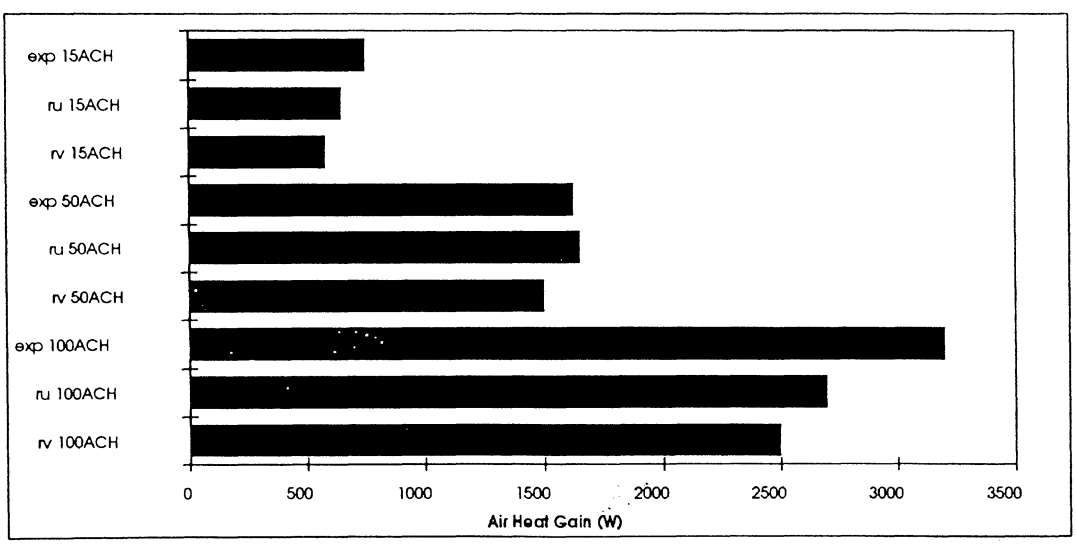

Figure 3.6 Comparison of Air Heat Gain Values

3.4 Simulation Results

Other than the prediction of temperatures and convection coefficients, a main goal of this project was to implement a variable grid. Graphical results are presented below for a single "slice" of the room which contains the inlet jet. In each case, experimental results are presented in the first image; followed by simulation results for each model type (laminar, turbulent with wall functions, turbulent low-Reynolds number) and for uniform and variable grid. In the next section, quantitative results will be presented. In each air flow rate section the velocity magnitude sections have been plotted at the same scale which permits direct wall jet comparisons between the experimental results, different fluid flow models, and grid types. The darker shades designate higher velocity magnitudes, of course. This section also allows one to study the shape of the wall jet and the amount of diffusion involved.

3.4.1 15 ACH Results

Experimental results at 15 ACH are shown in Figure 3.7. Figures 3.8, 3.9, and 3.10 show uniform and variable grid computational data for the laminar, turbulent wall function, and turbulent low-Reynolds number models, respectively.

The laminar sections, Figure 3.8, show that higher magnitudes were predicted with the non-uniform grid than with the uniform grid. The shape and spread of the jet are similar. the uniform plot shows higher velocities "climbing" the opposing wall. The transient analysis of the 15 ACH models showed this climbing effect quite clearly. When the wall

jet moves into the room, it is affected by buoyancy and follows along the floor to the far wall. Air is forced up the wall, moves back towards the inlet along the ceiling, and eventually a full recirculation pattern occurs. This recirculation pattern begins to occur at about the 40 second simulation mark in most of these 15 ACH models. Because this is the slowest velocity studied, the effect of buoyancy on each model is more visible. The recirculation pattern is more likely to occur and is the easiest to view at this lower air flow rate with a greater buoyancy effect.

By the time in the simulation when the recirculating flow moves along the ceiling on its journey back towards the inlet, the temperatures in the domain have decreased due to the 21° C inlet jet. This decreases the effect of buoyancy on the inlet air. As this occurs, the wall jet moves up and attempts to lift off the floor. When the recirculating flow returns to the area of the inlet, it physically knocks the wall jet down towards the floor. This "lifting" and "knocking" repeats as the simulation continues. But, the phenomenon is not as evident further in the transient solution because the temperature domain is closer to convergence and the simulation domain is three-dimensional.

The turbulent wall function model at 15 ACH, Figure 3.9, shows that the uniform grid plot predicts a thinner wall jet than the variable grid section. The effect of buoyancy appears to be greater in the non-uniform plot. The uniform grid profile is a unique 15 ACH plot because the jet is not attached the to the floor. In reality, the wall jet has been attached to the floor during previous time steps but has eventually lifted off the floor.

When considering jet shape and thickness, the wall function model seems to be the poorest match of the experimental results. Both the uniform and variable grid models would need to display greater buoyancy in order to match the experimental data closer.

The two turbulent low-Reynolds number model sections, Figure 3.10, are the closest match for the experimental data within their own grid types. The low-Reynolds number plots show wall jets which are thicker than the wall function plots but are thinner than the laminar plots. As stated earlier, the real test is a velocity magnitude analysis on a point by point basis such as the 2-D error numbers presented later.

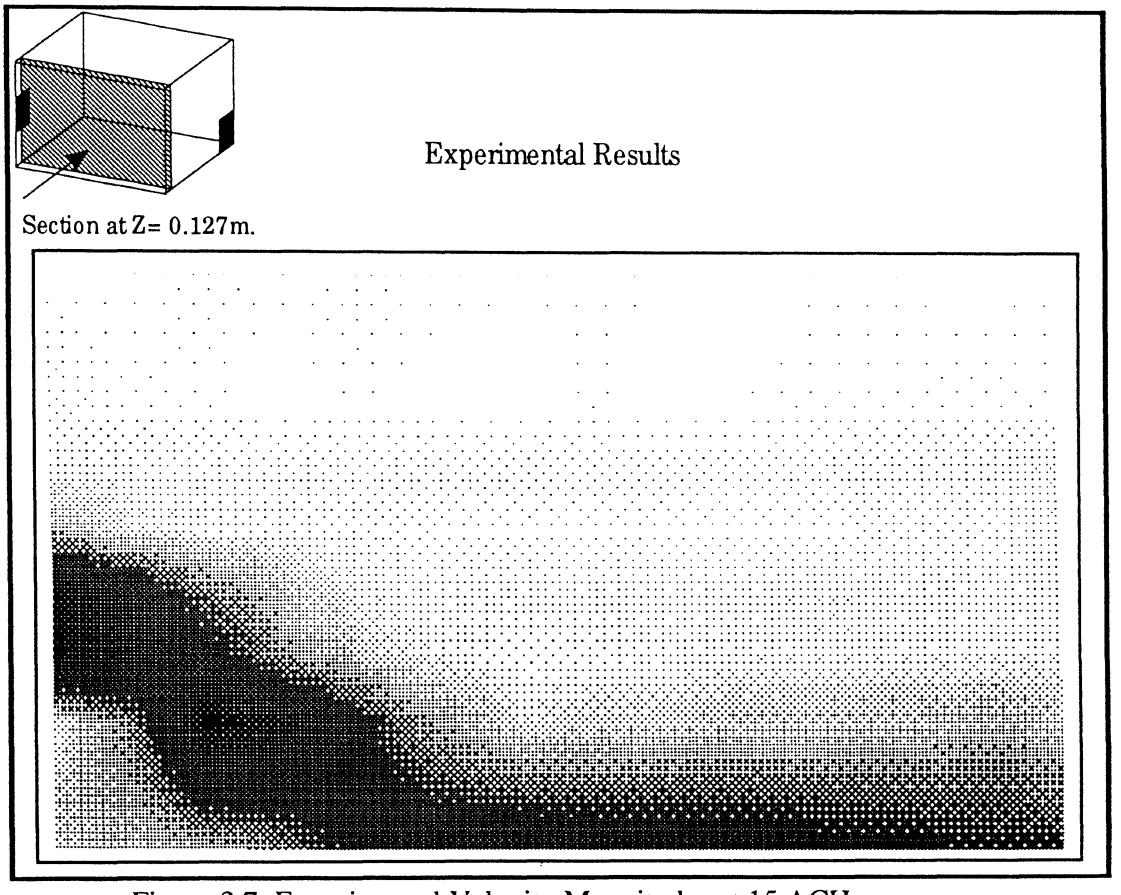

Figure 3.7 Experimental Velocity Magnitudes at 15 ACH

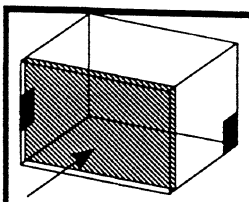

Laminar Results

Section at Z= 0.127m.

Uniform Grid

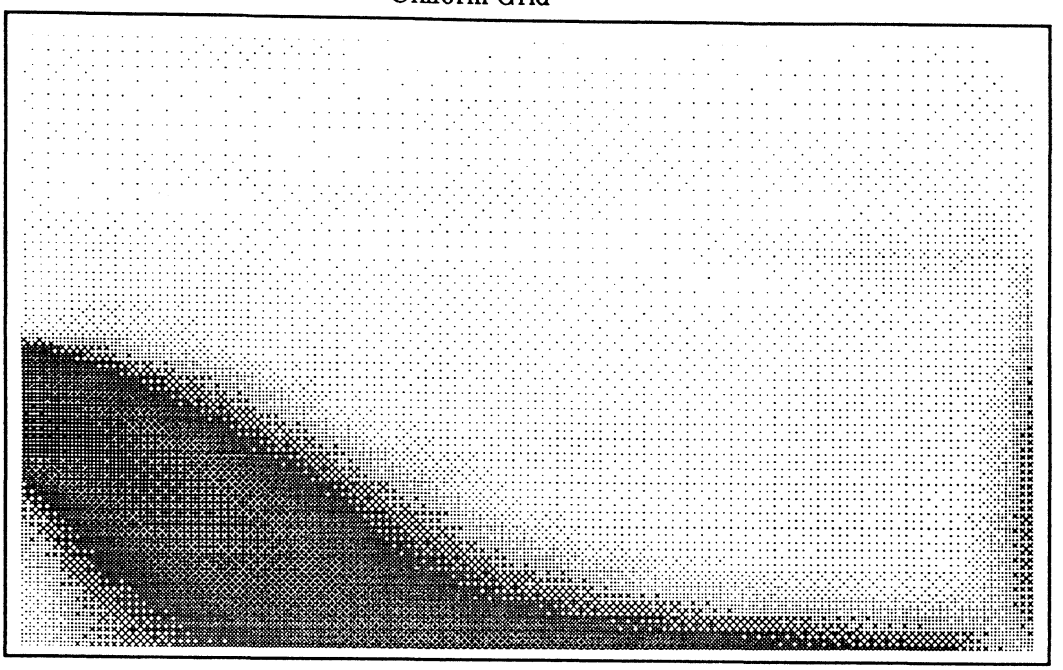

Variable Grid

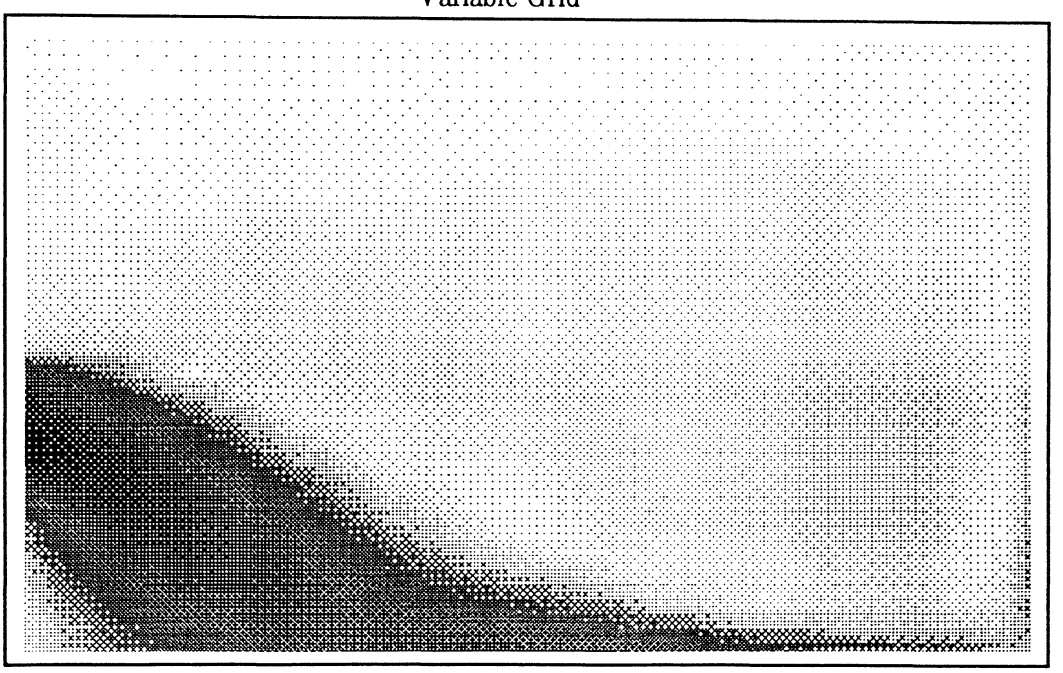

Figure 3.8 Laminar Velocity Magnitudes at 15 ACH

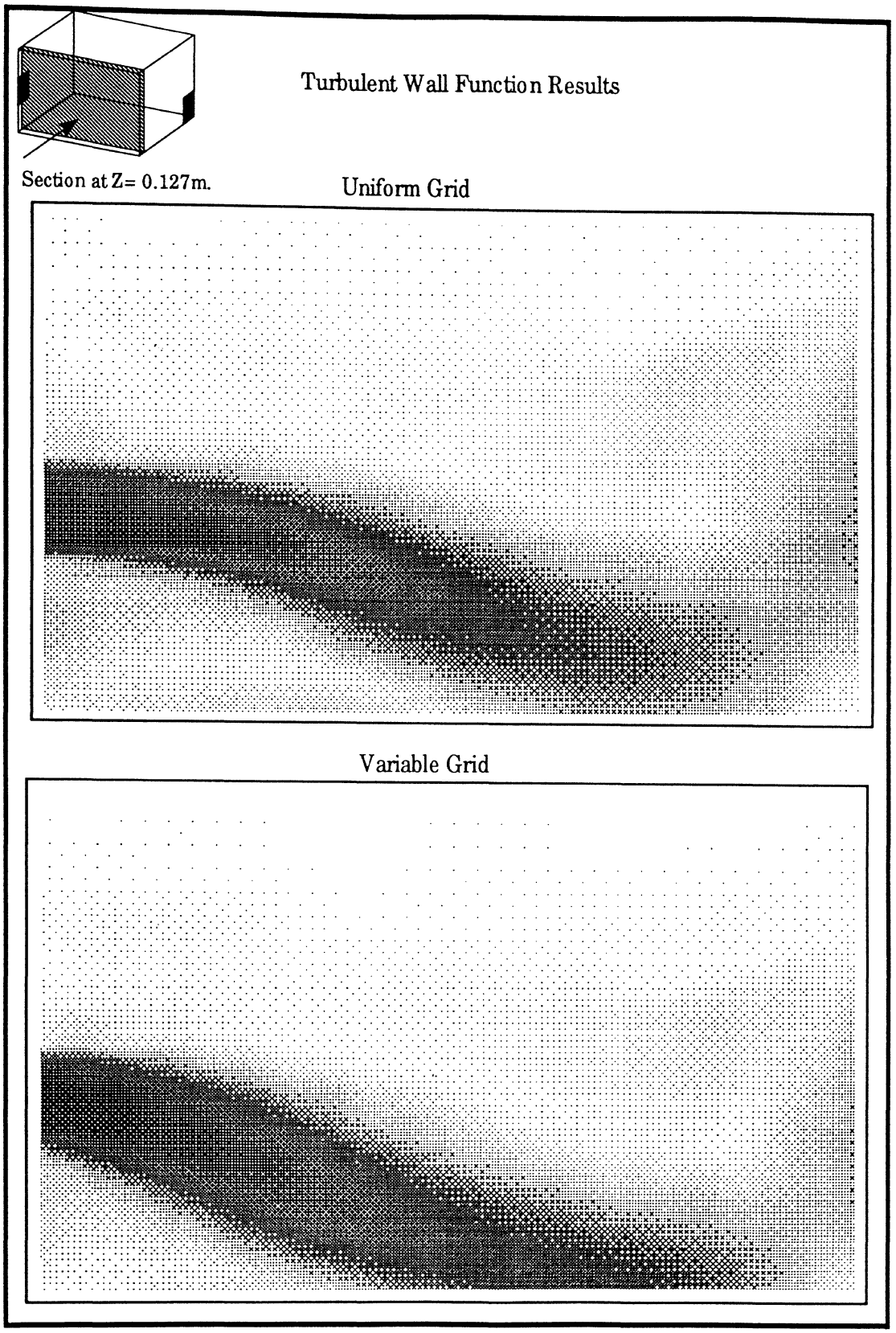

Figure 3.9 Wall Function Velocity Magnitudes at 15 ACH

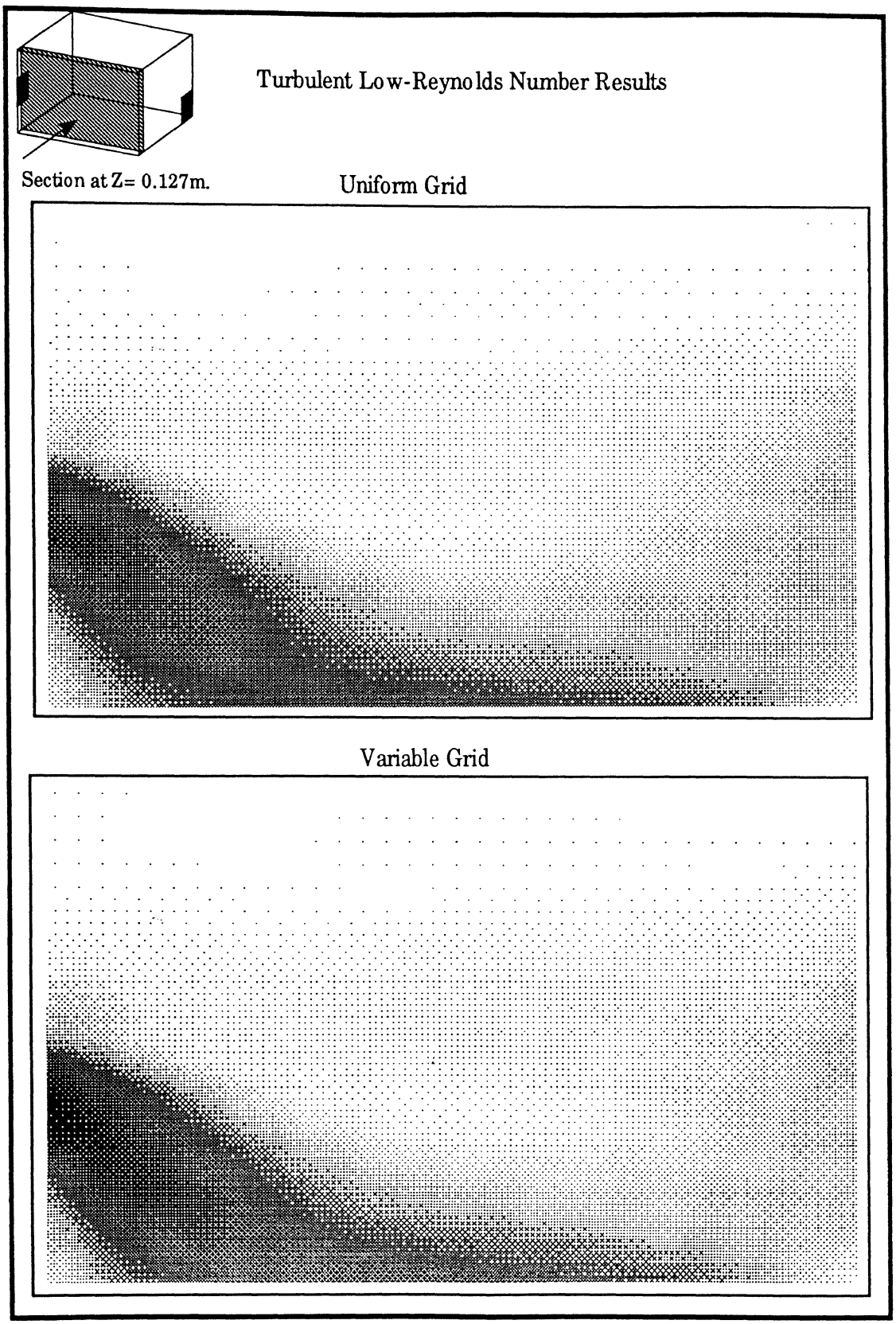

Figure 3.10 Low-Reynolds Number Velocity Magnitudes at 15 ACH

3.4.2 50 ACH Results

Naturally, the 50 ACH plots do not show as much buoyant effect as the slower velocity plots. In the following 50 ACH experimental section at z=0.127 m, Figure 3.11, the highest velocity magnitudes are at the inlet, but there is another pocket of higher velocity airflow in the central region of the bottom half of the plot. Much like the 15 ACH computational results, none of the 50 ACH computational plots, Figures 3.12, 3.13, and 3.14, produce a section of a wall jet with this isolated pocket of higher velocity. In fact, the turbulent wall function model calculates a wall jet which does not include that section of the plot because the spread of the wall jet is not wide enough. In the experimental 50 ACH plot, it even appears as though this region could be an area of recirculation, which is definitely not present in the laminar or low-Reynolds number simulations.

In terms of velocity magnitude matching of the experimental results, the low-Reynolds number variable grid plot is best, with the variable grid laminar plot not far behind. The uniform low-Reynolds number and laminar plots follow, respectively, and the variable and uniform grid wall function plots are the worst velocity magnitude predictors, for reasons mentioned earlier.

In each of the computational figures, the effect of gravity is obviously present. In other words, the right half of the plot or tip of the wall jet has dipped down towards the floor. This visible buoyant effect is an improvement over Weathers' 50 ACH simulations. Weathers' 50 ACH data displays almost no buoyant effects. With each of his simulation types a wall jet is calculated which has completely separated from the floor. Wall jet profiles which more closely match the shape of the experimental wall jet have been produced with this study. The experimental data, Figure 3.11, shows a jet that has separated only slightly from the floor. Especially figures 3.12 and 3.13 display jets which

appear to be in the process of lifting off the floor or have just done so. The present results also have produced more pronounced wall jet differences between the model types than Weathers' results.

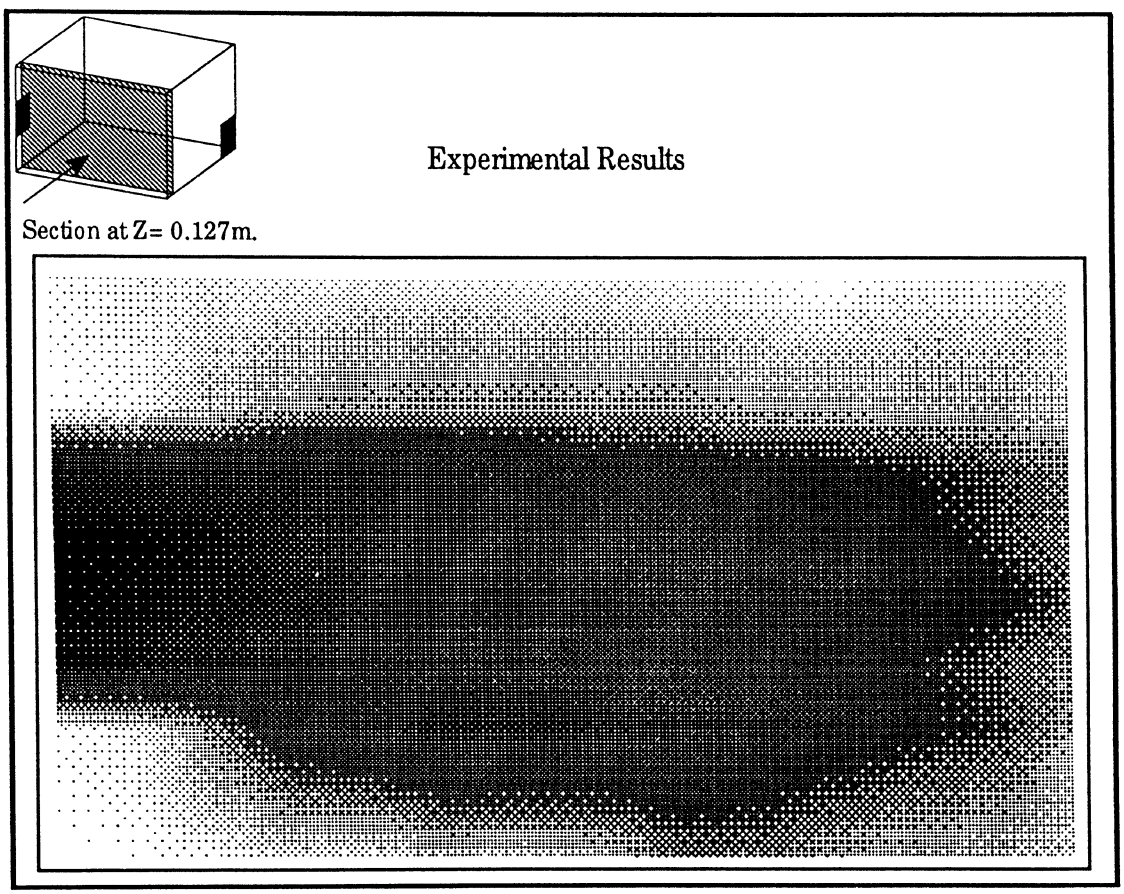

Figure 3.11 Experimental Velocity Magnitudes at 50 ACH

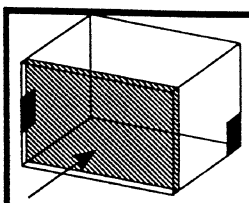

Laminar Results

Section at Z= 0.127m.

Uniform Grid

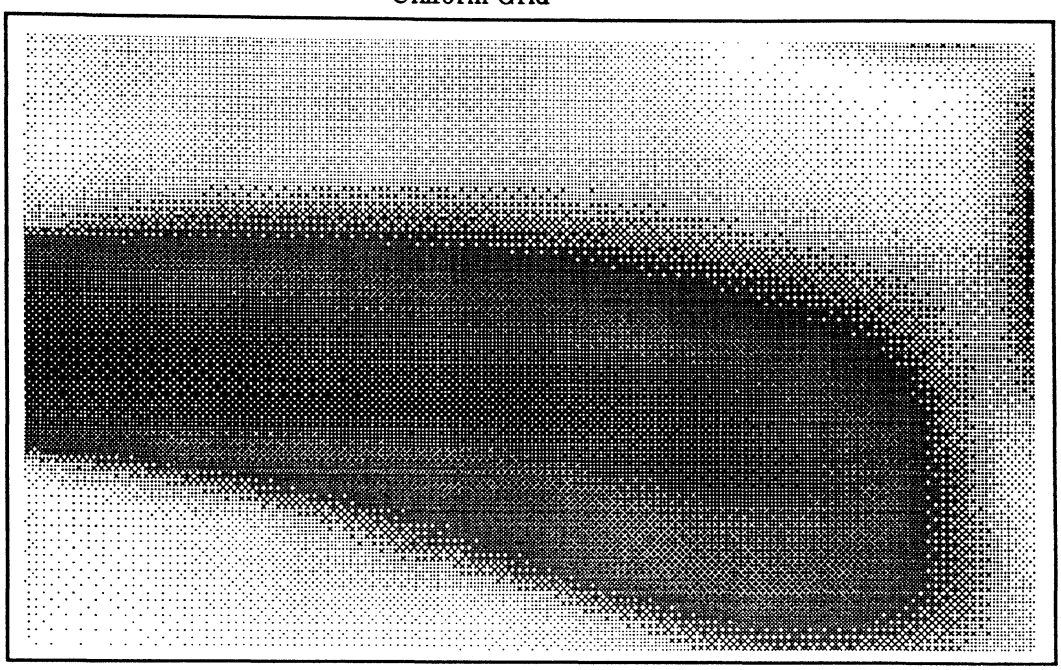

Variable Grid

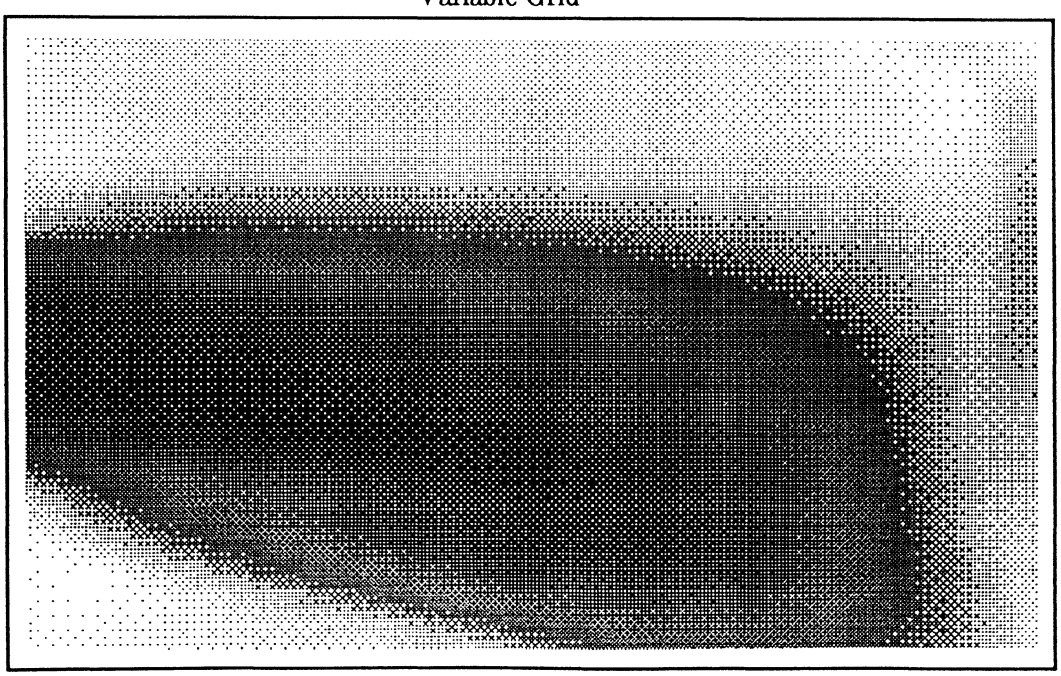

Figure 3.12 Laminar Velocity Magnitudes at 50 ACH

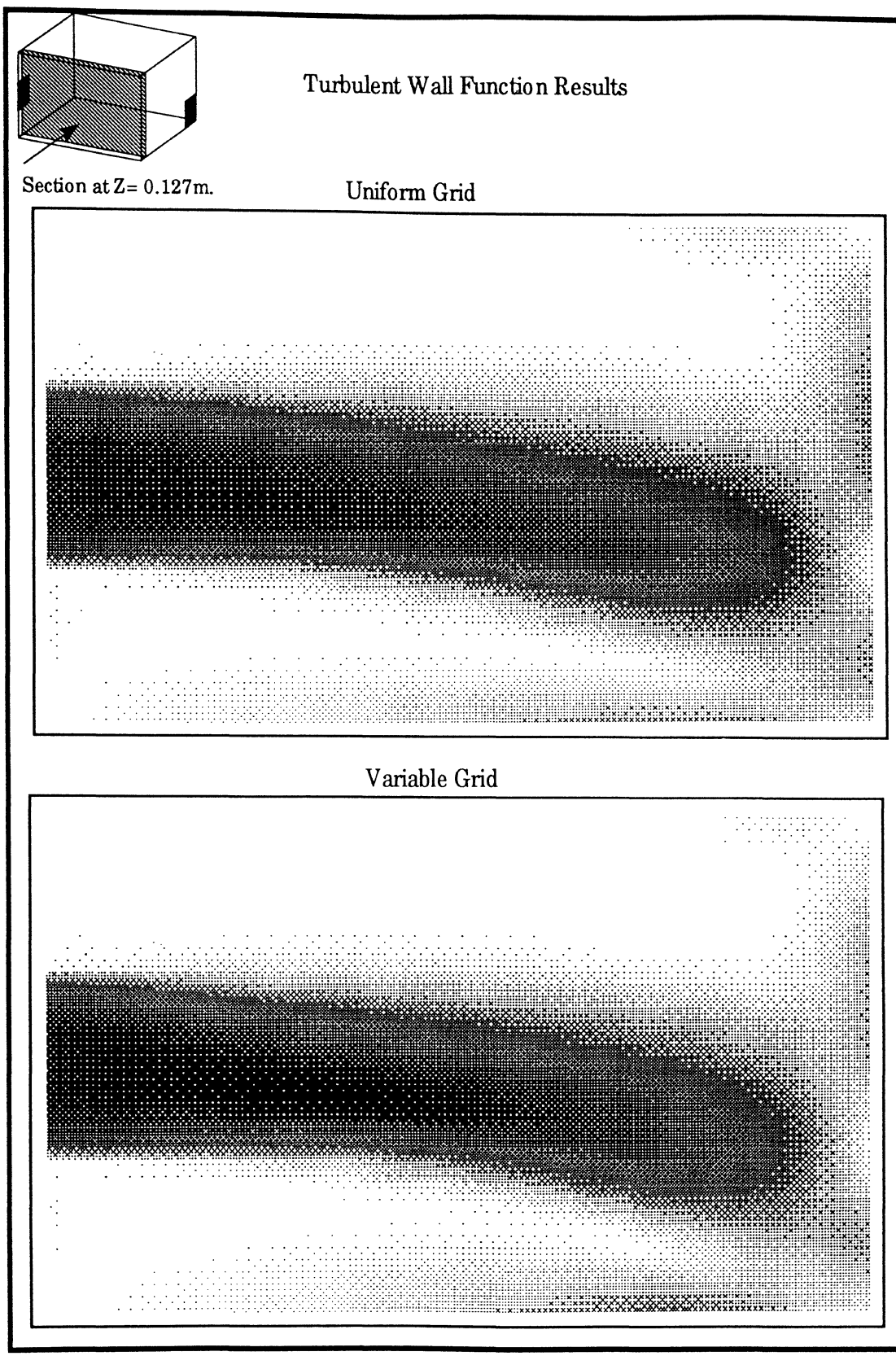

Figure 3.13 Wall Function Velocity Magnitudes at 50 ACH

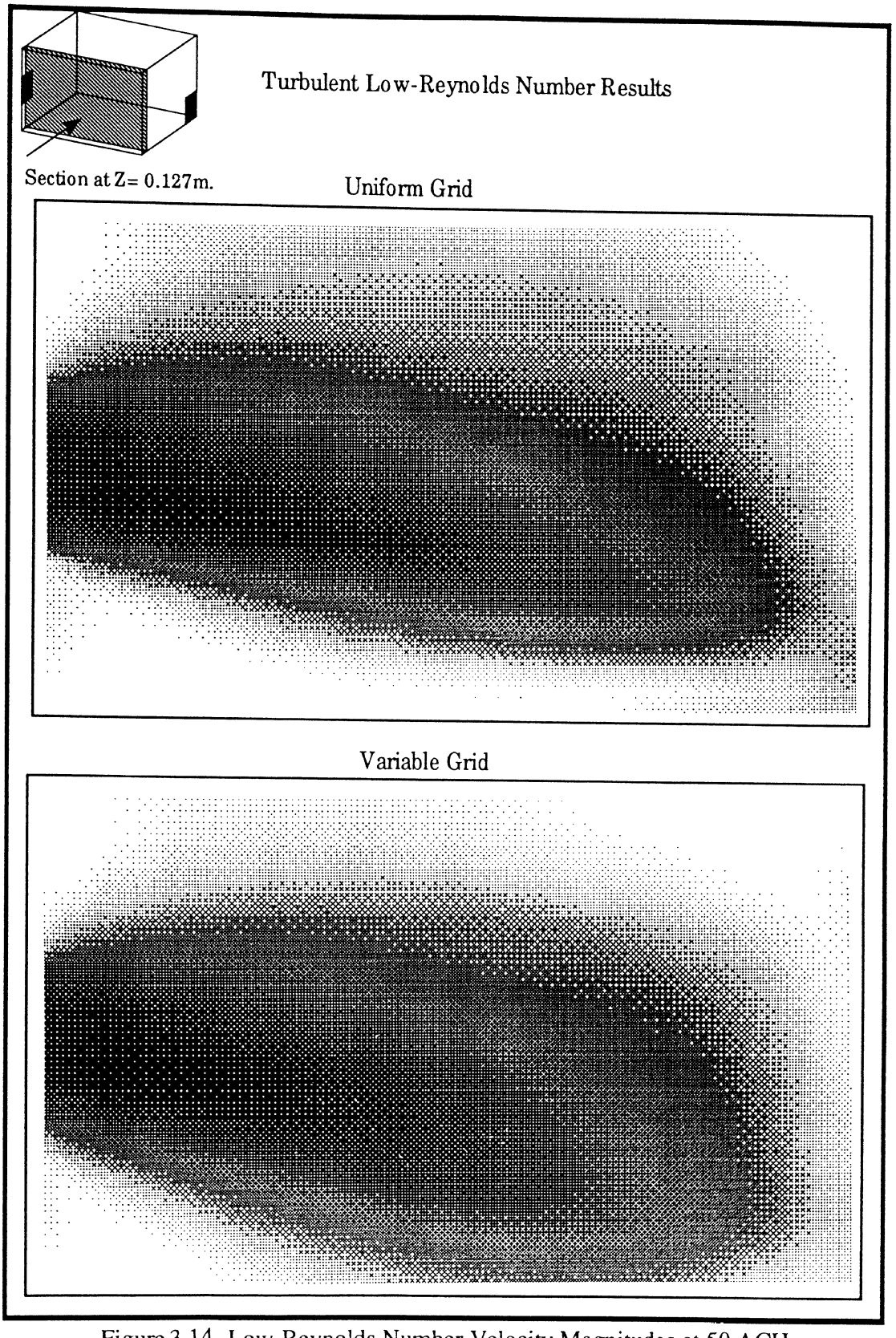

Figure 3.14 Low-Reynolds Number Velocity Magnitudes at 50 ACH

3.4.3 100 ACH Results

Many of the comments which were made about the 50 ACH results could also be made about the 100 ACH results. Again, Weathers' results showed little or no effect of gravity. The low-Reynolds number results, Figure 3.18, and the laminar variable grid results of Figure 3.16 still display definite buoyant effects. The turbulent wall function model, Figure 3.17, has not predicted enough jet diffusion. The laminar results in Figure 3.16 showed much more jet diffusion than Weather's results.

The flow pattern of the 100 ACH experimental plot is interesting. Notice in Figure 3.15 that there is no immediate change of the incoming flow until the jet spreads both up and down in an S-shaped pattern This S-shaped spreading begins to occur at about 1 meter into the room. It is possible that better experimental resolution might alter the shape of the spread. None of the 100 ACH computational data in this study has predicted an S-shaped spread. Either the jet starts to spread immediately like in Figures 3.16 and 3.17 or the jet doesn't really spread at all as in Figure 3.18.

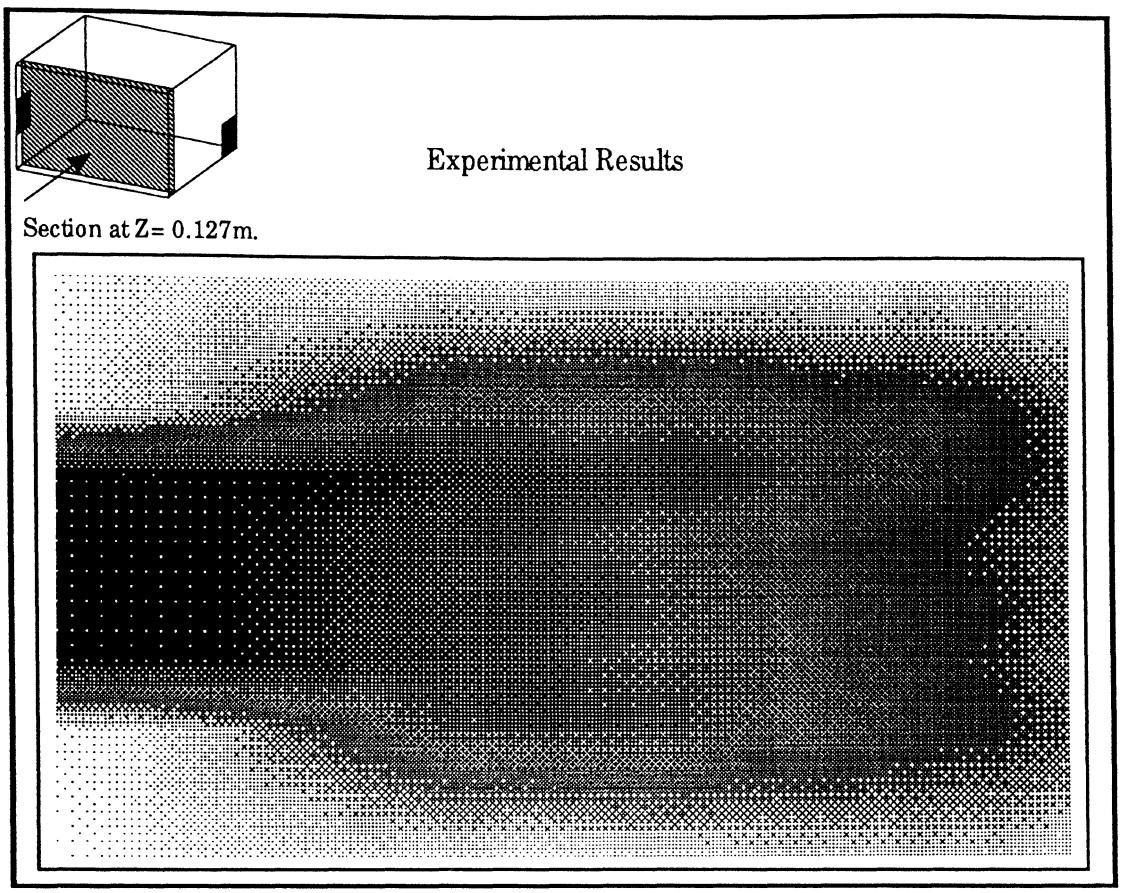

Figure 3.15 Experimental Velocity Magnitudes at 100 ACH

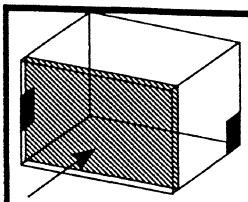

Laminar Results

Section at Z= 0.127m.

Uniform Grid

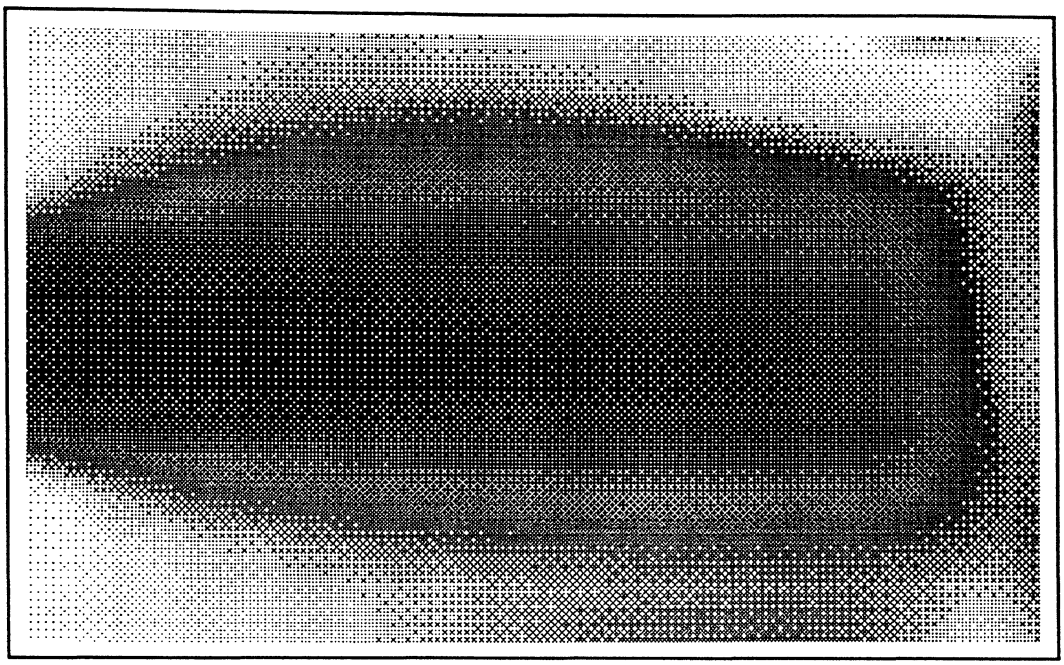

Variable Grid

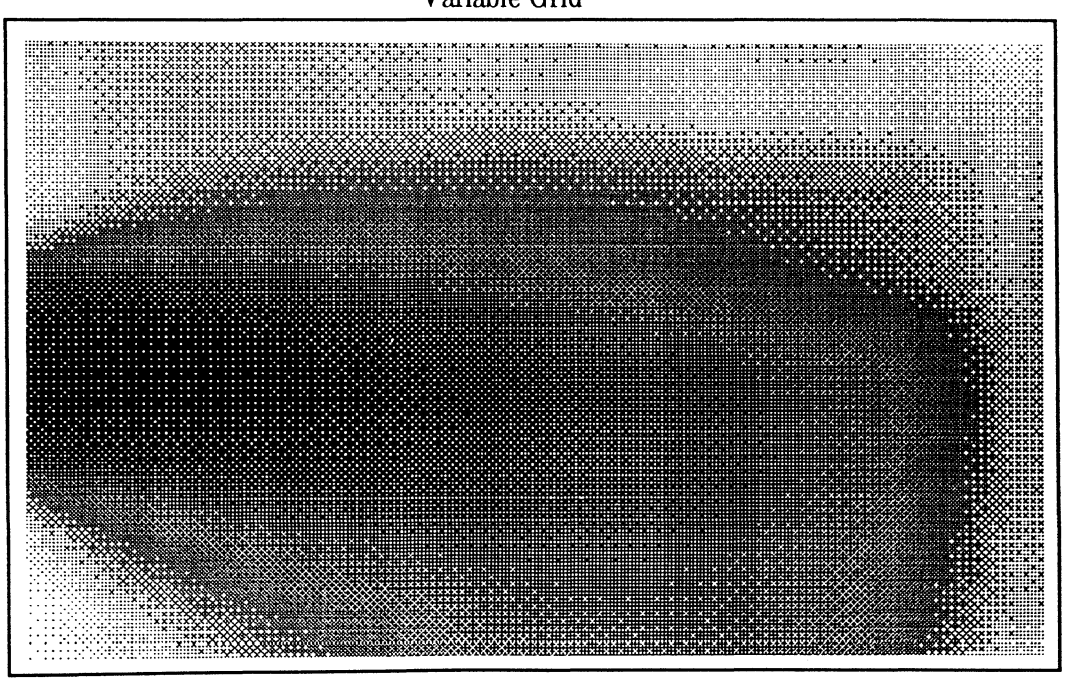

Figure 3.16 Laminar Velocity Magnitudes at 100 ACH

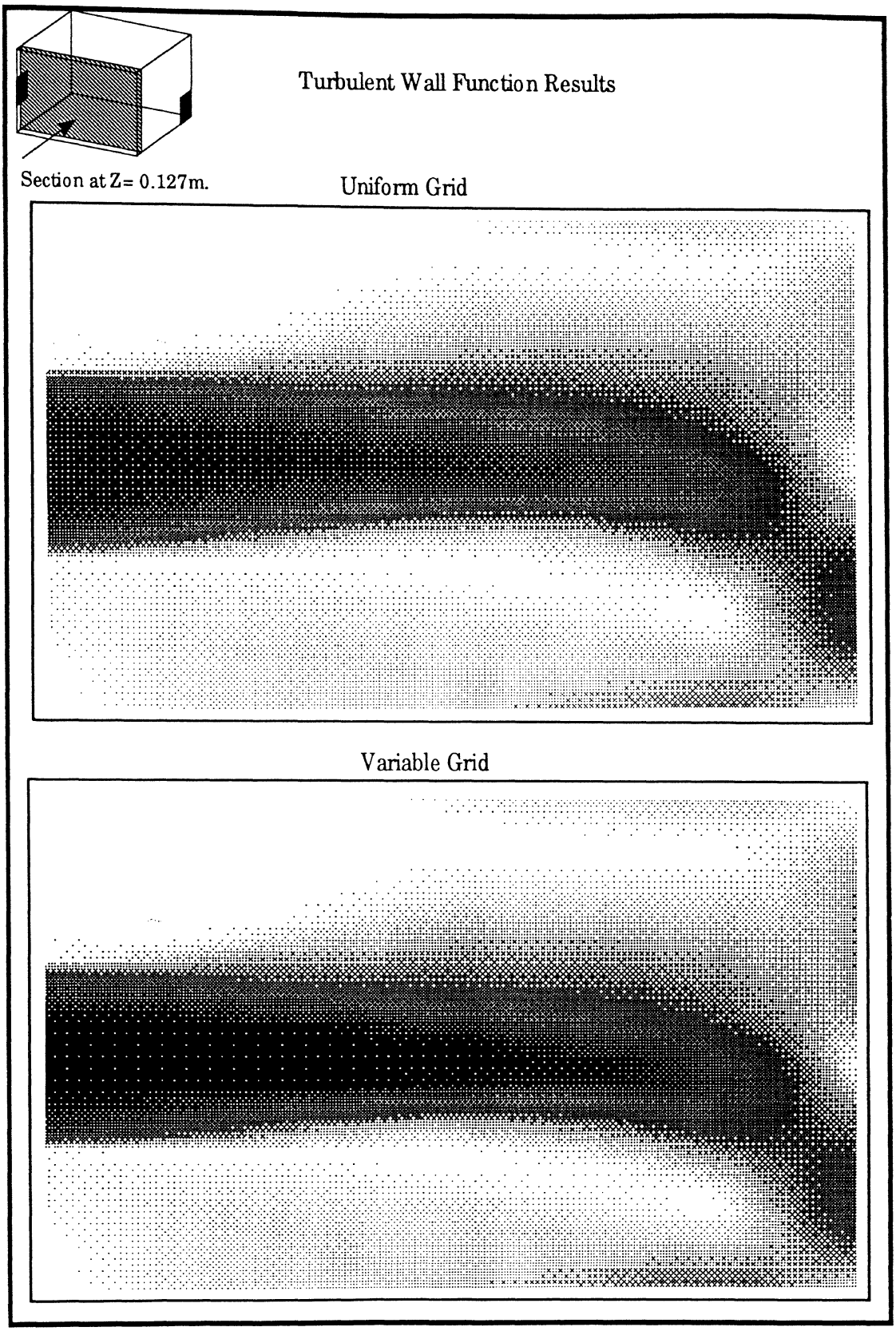

Figure 3.17 Wall Function Velocity Magnitudes at 100 ACH

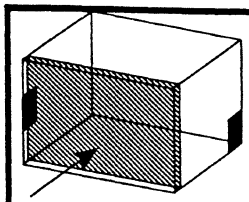

Turbulent Low-Reynolds Number Results

Section at Z= 0.127m.

Uniform Grid

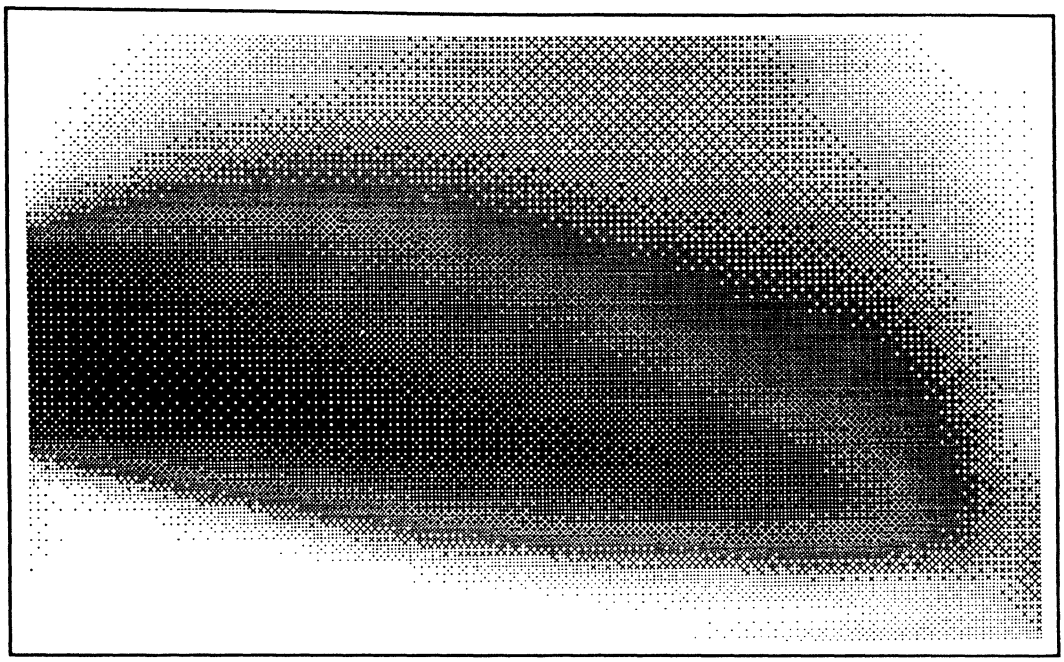

Variable Grid

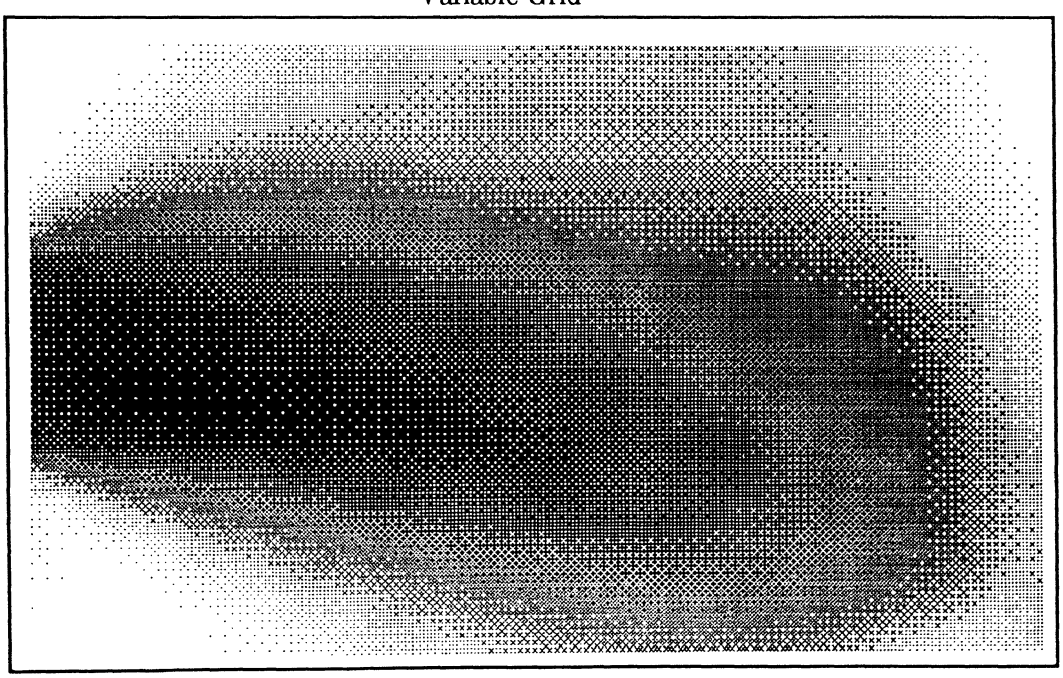

Figure 3.18 Low-Reynolds Number Velocity Magnitudes at 100 ACH

3.4.4 Global Velocity Magnitude Error Summary

A summary of velocity magnitude global error numbers is provided in Table 3.2 for direct comparison between the uniform grid the variable grid simulations. The global error number gives one a quantitative analysis of the how well the entire computational domain matches the experimental domain. The equation for the global error number has been presented earlier as equation (3.1).

Check marks note cases where the variable grid has shown improvements over the uniform grid simulations. The table below shows that over the entire domain the variable grid matches the experimental results about as well as the uniform grid. Using the variable grid seems to be more beneficial at the higher airflows.

TABLE 3.2

GLOBAL ERROR NUMBERS

Model Type and Airflow Rate:	Uniform Grid	Variable Grid	
Laminar 15 ACH:	0.0371	0.0503	
Wall Function 15 ACH:	0.0352	0.0378	
Low-Reynolds 15 ACH:	0.0408	0.0421	
Laminar 50 ACH:	0.0656	0.0633	√
Wall Function 50 ACH:	0.0828	0.0874	
Low-Reynolds 50 ACH:	0.0595	0.0544	√
Laminar 100 ACH:	0.0700	0.0690	√
Wall Function 100 ACH:	0.0820	0.0774	√
Low-Reynolds 100 ACH:	0.0645	0.0639	√

3.4.5 2-D Velocity Magnitude Error Summary

As stated earlier, all two-dimensional, or "slice" error numbers reported here are for the z=0.127 m. section. This gives a measure of how much the variable grid is helping to improve the results at the inlet. As stated in section 3.2, all 15 ACH simulations were run to 500 seconds, all 50 ACH simulations were run to 250 seconds, and all 100 ACH models were run to 100 seconds. The uniform and variable grid slice error numbers are presented below in Table 3.3.

TABLE 3.3

SLICE ERROR NUMBERS AT Z=0.127 m.

Model Type and Airflow Rate:	Uniform Grid	Variable Grid	
Laminar 15 ACH:	0.1276	0.0767	√
Wall Function 15 ACH:	0.1276	0.0736	√
Low-Reynolds 15 ACH:	0.1098	0.0644	√
Laminar 50 ACH:	0.1254	0.0979	√
Wall Function 50 ACH:	0.2144	0.1735	√
Low-Reynolds 50 ACH:	0.1090	0.0843	√
Laminar 100 ACH:	0.1520	0.1299	√
Wall Function 100 ACH:	0.2447	0.2055	√
Low-Reynolds 100 ACH:	0.0990	0.0934	√

The slice error numbers show slight improvement when the variable grid is used. Ideally, the variable grid would show improvement in every case of both the global error and slice error analysis. Improvement in the slice error number is more desirable because the reasons for using the variable grid are to improve resolution through the inlet, outlet, and near the wall.

4.0 CONCLUSIONS & RECOMMENDATIONS

4.1 Conclusions

The following conclusions were reached during this investigation:

1. The convergence of a computational model is often based on an arbitrary quantitative indicator and therefore convergence is sometimes assumed, when in fact it has not actually occurred. For this project, the convergence of each model was carefully analyzed in order to avoid past mistakes such as stopping the simulation early and assuming convergence. Many quantitative and qualitative indicators were studied to insure that convergence had been achieved and that the entire transient process was simulated and understood.

   The animated visualization of velocity and temperature values was the key to discovering that convergence had not been previously reached with the quantitative indicator. Further, the visualization techniques used in this project allowed the user to check that convergence of the velocity magnitudes had been reached, which was not previously possible with the quantitative indicator used.

2. Improvements have been made in the prediction of temperature and heat transfer with this project. The prediction of temperatures is relatively easy and accurate as long as one uses the experimental convection coefficients available. Accurate convection coefficient predictions are not yet possible using the wall temperature boundary conditions implemented in the experiments for this study.

3. Temperature predictions need to be as accurate as possible when modeling buoyancy. One also needs to verify that the temperatures have converged. Questions about convergence were investigated in this project. One should keep in mind that if the temperature field has not converged, then the velocity field has not converged either.

4. This 3-D turbulent code has the capacity to utilize a variable grid for better grid coverage and more accuracy at the inlet and outlet of the model. Using the 2-D error numbers as a gage for the experiments performed in this thesis, the variable grid matched the experimental results somewhat better than the uniform grid at the z=0.127 m. section.

5. For Weathers' uniform grid study, the global error analysis was a valid quantitative technique for directly comparing the accuracy of the models. One purpose of using a variable grid is to improve the prediction of a model near the wall. The slice error number is more sensitive to the error at the wall and is therefore a preferable choice for comparing models and grids.

4.2 Recommendations

1. Ideally, numerous non-uniform grids with different degrees of non-uniformity would have been used in this thesis. For further studies, one should increase the degree of non-uniformity of the grid. Use the 2-dimensional or "slice" error number to gage one's progress. Hold tight constraints on the computational models and show with one case how the degree of grid non-uniformity effects the results. Note the

convergence rate to observe whether one converges faster. Once the grid is chosen and proven, expand the experiment to include other model types and airflow rates.

2. Continued investigation of convergence issues might be aimed at improving automatic convergence criteria. Another quantitative indicator could be an inlet jet monitor. The direction of the inlet jet could be calculated at each time step based on the velocity magnitudes. Constraints on how much the direction of the inlet jet is allowed to change might aid in determining convergence. The constraints would have to be designed such that very small changes in the inlet jet direction do not declare convergence, such as during the 70-100 second time period shown in Figure 3.1 and discussed in section 3.2.

3. Expand the analysis to include other inlet and outlet configurations. Furniture or other obstructions could also be modeled.

4. More detailed experimental results would help the computational results in many different respects. More experimental information near the walls is needed. Also detailed experimental results might help to improve boundary conditions, at the outlet for example. The computational analysis could be coordinated with experimental research that will soon be performed in the school of Mechanical and Aerospace Engineering at Oklahoma State University.

5.0 REFERENCES

Aboosaidi, F., M. J. Warfield and D. Choudhury. 1991. Numerical Analysis Airflow in Aircraft Cabins. SAE Transactions, Vol. 100, pp. 1294-1304.

Alamdari, F. 1991a. Thermo-fluid Analysis in the Built Environment: Expectations and Limitations. Computational Fluid Dynamics for the Environmental and Building Services Engineer - Tool or Toy?, London: Mechanical Engineering Publications. pp. 5-12.

Alamdari, F., S. C. Edwards and S. P. Hammond. 1991b. Microclimate Performance of an Open Atrium Office Building: A Case Study in Thermo-fluid Modelling. Computational Fluid Dynamics for the Environmental and Building Services Engineer - Tool or Toy?, London: Mechanical Engineering Publications. pp. 81-92.

Anderson, R., V. Hassani, A. Kirkpatrick, K. Knappmiller and D. Hittle. 1991. Visualizing the Air Flow from Cold Air Ceiling Jets. ASHRAE Journal, pp. 30, 32-35.

Awbi, H. B. 1989a. Application of Computational Fluid Dynamics in Room Ventilation. Building and Environment, Vol. 24, pp. 73-84.

Awbi, H. B. and M. M. Nemri. 1990. Scale Effect in Room Airflow Studies. Energy and Buildings, Vol. 14, pp. 207-210.

Awbi, H. B. and A. A. Setrak. 1989b. Numerical Solution of Wall Jets. ASHRAE Building Systems: Room Air and Air Contaminant Distribution, Atlanta, GA 30329. pp. 136-141.

Awbi, H. B. and G. Gan. 1991. Computational Fluid Dynamics in Ventilation. Computational Fluid Dynamics for the Environmental and Building Services Engineer - Tool or Toy?, London: Mechanical Engineering Publications. pp. 67-79.

Awolesi, S. T., H. B. Awbi, M. J. Seymour and R. A. Hiley. 1991. The Use of CFD Techniques for the Assessment and Improvement of a Workshop Ventilation System. Computational Fluid Dynamics for the Environmental and Building Services Engineer - Tool or Toy?, London: Mechanical Engineering Publications. pp. 39-46.

Baker, A. J. and R. M. Kelso. 1990. On Validation of Computational Fluid Dynamics Procedures for Room Air Motion Prediction. ASHRAE Transactions, Vol. 96, Pt. 2, pp. 760-774.

Baker, A. J., R. M. Kelso, W. P. Noronha and J. B. Woods. 1989. On the Maturing of Computational Fluid Dynamics in Design of Room Air Ventilation Systems. ASHRAE Building Systems, pp. 149-152.

Chandrasekhara Swamy, N. V. and P. Bandyopadhyay. 1975. Mean and Turbulence Characteristics of Three-Dimensional Wall Jets. Journal of Fluid Mechanics, Vol. 71, pp. 541-562.

Chen, Q. and Z. Jiang. 1992a. Significant Questions in Predicting Room Air Motion. ASHRAE Transactions, Vol. 98, Pt. 1, pp. 929-939.

Chen, Q. and Z. Jiang. 1992b. Air Supply Method and Indoor Environment. Indoor Environment, Vol. 1, pp. 88-102.

Chen, Q. and J. van der Kooi. 1987. Experiments and 2D Approximated Computations of 3D Air Movement, Heat and Concentration Transfer in a Room. Air Distribution in Ventilated Spaces, Stockholm, Sweden. pp. 1-14.

Chen, Q. and J. van der Kooi. 1990a. A Methodology for Indoor Airflow Computations and Energy Analysis for a Displacement Ventilation System. Energy and Buildings, Vol. 14, pp. 259-271.

Chen, Q. and J. van der Kooi. 1991a. Transient Heat Transfer Through the Enclosures of a Room with Mixed Convection. Heat and Mass Transfer in Building Materials and Structures, pp. 697-706.

Chen, Q., A. Moser and A. Huber. 1990b. Prediction of Buoyant, Turbulent Flow by a Low-Reynolds-Number k-ε Model. ASHRAE Transactions, Vol. 96, Pt. 2, pp. 564-573.

Chen, Q., A. Moser and P. Suter. 1991b. Interpolation Theory and Influence of Boundary Conditions on Room Air Diffusion. Building and Environment, Vol. 26, No. 4, pp. 433-445.

Chen, Q., A. Moser and P. Suter. 1992c. A Numerical Study of Indoor Air Quality and Thermal Comfort Under Six Kinds of Air Diffusion. ASHRAE Transactions, Vol. 98, Pt. 1, pp. 203-217.

Chen, Q., P. Suter and A. Moser. 1991c. Influence of Air Supply Parameters on Indoor Air Diffusion. Building and Environment, Vol. 26, No. 4, pp. 417-431.

Deardorff, J. W. 1970. A Numerical Study of Three-Dimensional Turbulent Channel Flow at Large Reynolds Numbers. Journal of Fluid Mechanics, Vol. 41, Pt. 2, pp. 453-480.

Ewert, M., U. Renz, N. Vogl and M. Zeller. 1991. Definition of the Flow Parameters at the Room Inlet Device - Measurements and Calculations. 12th AIVC Conference, Ottawa, Canada. pp. 231-237.

Fang, J. B. and R. A. Grot. 1990. Numerical Simulation of the Performance of Building Ventilation Systems. ASHRAE Transactions, Vol. 96, Pt. 2, pp. 361-366.

Fang, J. B., R. A. Grot and T. Kurabuchi. 1988. Application of Mathematical Modeling to the Evaluation of Building Ventilation Systems. 9th AIVC Conference, Gent, Belgium. pp. 327-341.

Fawcett, N. S. J. 1991. Getting Started with CFD. Computational Fluid Dynamics for the Environmental and Building Services Engineer - Tool or Toy?, London: Mechanical Engineering Publications. pp. 1-4.

Gan, G., H. B. Awbi and D. J. Croome. 1991. Simulation of Air Flow in Naturally Ventilated Buildings. Building Simulation '91, Nice, France. pp. 78-84.

Gosman, A. D., P. V. Nielsen, A. Restivo and J. H. Whitelaw. 1980. The Flow Properties of Rooms With Small Ventilation Openings. Transactions of the ASME, Vol. 102, pp. 316-323.

Haghighat, F., Z. Jiang and J. C. Y. Wang. 1989. Natural Convection and Air Flow Pattern in a Partitioned Room with Turbulent Flow. ASHRAE Journal, pp. 600-610.

Haghighat, F., Z. Jiang, J. C. Y. Wang and F. Allard. 1992. Air Movement in Buildings Using Computational Fluid Dynamics. Transactions of the ASME, Vol. 114, pp. 84-92.

Haghighat, F., J. C. Y. Wang and Z. Jiang. 1990. Three-Dimensional Analysis of Airflow Pattern and Contaminant Dispersion in a Ventilated Two-Zone Enclosure. ASHRAE Transactions, Vol. 96, Pt. 1, pp. 831-839.

Harlow, F. H. and J. E. Welch. 1965. Numerical Calculation of Time-Dependent Viscous Incompressible Flow of Fluid with Free Surface. The Physics of Fluids, Vol. 8, No. 12, pp. 2182-2189.

Heikkinen, J. 1991. Modelling of a Supply Air Terminal for Room Air Flow Simulation. 12th AIVC Conference, Ottawa, Canada. pp. 213-230.

Herrero, J., F. X. Grau, J. Grifoll and F. Giralt. 1991. A Near Wall k-ε Formulation for High Prandtl Number Heat Transfer. International Journal of Heat and Mass Transfer, Vol. 34, No. 3, pp. 711-721.

Hinze, J. O. 1987. Turbulence. New York: McGraw-Hill. pp. 790.

Hirt, C. W. and J. L. Cook. 1972. Calculating Three-Dimensional Flows Around Structures and Over Rough Terrain. Journal of Computational Physics, Vol. 10, pp. 324-340.

Hirt, C. W., B. C. Nichols and N. C. Romero 1975. SOLA - A Numerical Solution Algorithm for Transient Fluid Flows. Los Alamos Scientific Laboratory. LA-5852.

Jiang, Z., Q. Chen and A. Moser. 1992. Indoor Airflow with Cooling Panel and Radiative/Convective Heat Source. ASHRAE Transactions, Vol. 98, Pt. 1, pp. 33-42.

Jin, Y. and J. R. Ogilvie. 1992. Isothermal Airflow Characteristics in a Ventilated Room with a Slot Inlet Opening. ASHRAE Transactions, Vol. 98, Pt. 2, pp. 296-306.

Jones, P. J. and G. E. Whittle. 1992. Computational Fluid Dynamics for Building Air Flow Prediction - Current Status and Capabilities. Building and Environment, Vol. 27, No. 3, pp. 321-338.

Kato, S., S. Murakami and S. Nagano. 1992. Numerical Study on Diffusion in a Room with a Locally Balanced Supply-Exhaust Airflow Rate System. ASHRAE Transactions, Vol. 98, Pt. 1, pp. 218-238.

Kelso, R. M., L. E. Wilkening, E. G. Schaub and A. J. Baker. 1992. Computational Simulation of Kitchen Airflows with Commercial Hoods. ASHRAE Transactions, Vol. 98, Pt. 1, pp. 1219-1225.

Kim, J., S. J. Kline and J. P. Johnston. 1980. Investigation of a Reattaching Turbulent Shear Layer: Flow Over a Backward-Facing Step. Transactions of the ASME, Vol. 102, pp. 302-308.

Kurabuchi, T. and T. Kusuda. 1987. Numerical Prediction for Indoor Air Movement. ASHRAE Journal, Vol. 29, No. 12, pp. 26-30.

Kurabuchi, T., Y. Sakamoto and M. Kaizuka. 1989. Numerical Prediction of Indoor Airflows by Means of the k-ε Turbulence Model. Building Systems, University of Illinois. pp. 57-67.

Lam, C. K. G. and K. Bremhorst. 1981. A Modified Form of the k-ε Model for Predicting Wall Turbulence. Transactions of the ASME, Vol. 103, pp. 456-460.

Launder, B. E. and D. B. Spalding. 1974. The Numerical Computation of Turbulent Flows. Computer Methods in Applied Mechanics and Engineering, Vol. 3, pp. 269-289.

Launder, B. E. and W. Rodi. 1983. The Turbulent Wall Jet - Measurements and Modeling. Annual Review of Fluid Mechanics, Vol. 15, pp. 429-459.

Li, Y., L. Fuchs and X. Bai. 1991a. Accurate Numerical Simulation of Air Flows in Ventilated Multi-Rooms. Building Simulation '91, Nice, France. pp. 85-91.

Li, Y., L. Fuchs and S. Holmberg. 1991b. An Evaluation of a Computer Code for Predicting Indoor Airflow and Heat Transfer. 12th AIVC Conference, Ottawa, Canada. pp. 123-136.

Liddament, M. W. 1991. A Review of Building Air Flow Simulation. Air Infiltration and Ventilation Centre. AIVC 33.

Lilley, D. G. 1988. Three-Dimensional Flow Prediction for Industrial Mixing. ASME International Computers in Engineering Conference, San Francisco, CA.

Lilley, D. G. 1993. Personal Communications.

Mansour, N. N., J. Kim and P. Moin. 1989. Near-Wall k-ε Turbulence Modeling. AIAA Journal, Vol. 27, No. 8, pp. 1068-1073.

Morel, R., A. Laassibi, E. Alcaraz, R. Zegadi, G. Brun and D. Jeandel. 1992. Validation of a k-ε Model Based on Experimental Results in a Thermally Stable Stratified Turbulent Boundary Layer. International Journal of Heat and Mass Transfer, Vol. 35, No. 10, pp. 2717-2724.

Murakami, S. and S. Kato. 1989a. Current Status of Numerical and Experimental Methods for Analyzing Flow Field and Diffusion Field in a Room. Building Systems, University of Illinois. pp. 39-56.

Murakami, S. and S. Kato. 1989b. Numerical and Experimental Study on Room Airflow- 3-D Predictions using the k-ε Turbulence Model. Building and Environment, Vol. 24, No. 1, pp. 85-97.

Murakami, S., S. Kato and Y. Ishida. 1989d. 3-D Numerical Simulation of Turbulent Air Flow In and Around Buildings Based on the k-ε Model with Generalized Curvilinear Coordinates. ASHRAE Transactions, Vol. 95, Pt. 2, pp. 30-57.

Murakami, S., S. Kato, S. Nagano and Y. Tanaka. 1992a. Diffusion Characteristics of Airborne Particles with Gravitational Settling in a Convection-Dominant Indoor Flow Field. ASHRAE Transactions, Vol. 98, Pt. 1, pp. 82-97.

Murakami, S., S. Kato and Y. Suyama. 1987. Three-Dimensional Numerical Simulation of Turbulent Airflow in a Ventilated Room by Means of a Two-Equation Model. ASHRAE Transactions, Vol. 93, Pt. 2, pp. 621-641.

Murakami, S., S. Kato and Y. Suyama. 1989c. Numerical Study on Diffusion Field as Affected by Arrangement of Supply and Exhaust Openings in Conventional Flow Type Clean Room. ASHRAE Transactions, Vol. 95, Pt. 2, pp. 113-127.

Murakami, S., S. Kato and Y. Suyama. 1990. Numerical Study of Flow and Contaminant Diffusion Fields as Affected by Flow Obstacles in Conventional-Flow-Type Clean Room. ASHRAE Transactions, Vol. 96, Pt. 1, pp. 343-355.

Murakami, S., S. Kato, T. Tanaka, D. H. Choi and T. Kitazawa. 1992b. The Influence of Supply and Exhaust Openings on Ventilation Efficiency in an Air-Conditioned Room with a Raised Floor. ASHRAE Transactions, Vol. 98, Pt. 1, pp. 738-755.

Murakami, S., T. Toshihiko and S. Kato. 1983. Numerical Simulation of Air Flow and Gas Diffusion in Room Model - Correspondence between Numerical Simulation and Model Experiment. The Fourth International Symposium on The Use of Computers for Environmental Engineering Related to Buildings, Tokyo, Japan. pp. 90-95.

Myong, H. K. and N. Kasagi. 1990. Prediction of Anisotrophy of the Near-Wall Turbulence with an Anisotropic Low-Reynolds-Number k-ε Turbulence Method. Journal of Fluids Engineering, Vol. 112, pp. 521-524.

Myong, H. K. and T. Kobayashi. 1991. Prediction of Three-Dimensional Developing Turbulent Flow in a Square Duct with an Anisotropic Low-Reynolds-Number k-ε Model. Transactions of the ASME, Vol. 113, pp. 608-615.

NCSA Image for the Macintosh® Version 3.0. December 1990. University of Illinois at Urbana-Champaign.

Nielsen, P. V. 1989. Numerical Prediction of Air Distribution in Rooms - Status and Potentials. Building Systems, University of Illinois. pp. 31-38.

Nielsen, P. V. 1991. Models for the Prediction of Room Air Distribution. 12th AIVC Conference, Ottawa, Canada. pp. 55-71.

Nielsen, P. V. 1992. Description of Supply Openings in Numerical Models for Room Air Distribution. ASHRAE Transactions, Vol. 98, Pt. 1, pp. 963-971.

Nielsen, P. V. and A. T. A. Moller. 1982. New Developments in Room Air Distribution. Construction Industry Conference, University of Nottingham.

Nielsen, P. V. and A. T. A. Moller. 1987. Measurements of Buoyant Wall Jet Flows in Air-Conditioned Rooms. ROOMVENT 87, Stockholm, Sweden. pp. 1-12.

Nielsen, P. V., A. Restivo and J. H. Whitelaw. 1978. The Velocity Characteristics of Ventilated Rooms. Journal of Fluids Engineering, Vol. 100, pp. 291-298.

Nielsen, P. V., A. Restivo and J. H. Whitelaw. 1979. Buoyancy-Affected Flows in Ventilated Rooms. Numerical Heat Transfer, Vol. 2, pp. 115-127.

Patel, V. C., W. Rodi and G. Scheuerer. 1985. Turbulence Models for Near-Wall and Low Reynolds Number Flows: A Review. AIAA Journal, Vol. 23, No. 9, pp. 1308-1318.

Paullay, A. J., R. E. Melnik, A. Rubel, S. Rudman and M. J. Siclari. 1985. Similarity Solutions for Plane and Radial Jets Using a k-ε Turbulence Model. Journal of Fluids Engineering, Vol. 107, pp. 79-85.

Rodi, W. 1980. Turbulence Models for Environmental Problems in Prediction Methods for Turbulent Flows. New York: Hemisphere/McGraw-Hill. pp. 259-349.

Rodi, W. and N. N. Mansour. 1993. Low Reynolds Number k-ε Modelling with the Aid of Direct Simulation Data. Journal of Fluid Mechanics, Vol. 250, pp. 509-529.

Rodi, W. and G. Scheuerer. 1986. Scrutinizing the k-ε Turbulence Model Under Adverse Pressure Gradient Conditions. Transactions of the ASME, Vol. 108, pp. 174-179.

Sakamoto, Y. and Y. Matsuo. 1980. Numerical Predictions of Three-Dimensional Flow in a Ventilated Room Using Turbulence Models. Applied Mathematical Modelling, Vol. 4, pp. 67-72.

Schachenmann, A., D. Wiss and G. Metzen. 1990. Numerical Calculation of Room Air Currents and Comparison with LDA Measurements Under Free and Forced Convection. Sulzer Technical Review, Vol. 72, pp. 30-35.

Schaelin, A., J. van der Maas and A. Moser. 1992. Simulation of Airflow Through Large Openings in Buildings. ASHRAE Transactions, Vol. 98, Pt. 2, pp. 319-328.

Setrakian, A. and D. McLean. 1991b. Building Simulations Using Thermal and CFD Models. Building Simulation '91, Nice, France. pp. 235-240.

Setrakian, A. A. and D. A. Morgan. 1991a. Applications of Computational Fluid Dynamics in Building Services Engineering. Computational Fluid Dynamics for the Environmental and Building Services Engineer - Tool or Toy?, London: Mechanical Engineering Publications. pp. 33-37.

Skovgaard, M. and P. V. Nielsen. 1991a. Numerical Investigation of Transient Flow Over a Backward Facing Step Using Low Reynolds Number k-ε Model. 12th AIVC Conference, Ottawa, Canada. pp. 201-212.

Skovgaard, M. and P. V. Nielsen. 1991b. Modelling Complex Inlet Geometries in CFD-Applied to Air Flow in Ventilated Rooms. 12th AIVC Conference, Ottawa, Canada. pp. 184-198.

So, R. M. C. and H. S. Zhang. 1991. Near-Wall Modeling of the Dissipation Rate Equation. AIAA Journal, Vol. 29, No. 12, pp. 2069-2076.

Speziale, C. G. 1987. On Nonlinear k-l and k-ε Models of Turbulence. Journal of Fluid Mechanics, Vol. 178, pp. 450-475.

Speziale, C. G., R. Abid and E. C. Anderson. 1992. Critical Evaluation of Two-Equation Models for Near-Wall Turbulence. AIAA Journal, Vol. 30, No. 2, pp. 324-331.

Spitler, J. D. 1990. An Experimental Investigation of Air Flow and Convective Heat Transfer in Enclosures Having Large Ventilative Rates. Ph.D. Thesis. University of Illinois at Urbana-Champaign.

Spitler, J. D., C. O. Pedersen and R. J. Bunkofske. 1987. Experimental Study of Interior Convective and Radiative Heat Transfer in Buildings. 24th National Heat Transfer Conference and Exhibition, Pittsburgh, PA. pp. 67-76.

Spitler, J. D., C. O. Pedersen and D. E. Fisher. 1991b. Interior Convective Heat Transfer in Buildings with Large Ventilative Flow Rates. ASHRAE Transactions, Vol. 97, Pt. 1, pp. 505-515.

Spitler, J. D., C. O. Pedersen, D. E. Fisher, P. F. Menne and J. Cantillo. 1991a. An Experimental Facility for Investigation of Interior Convective Heat Transfer. ASHRAE Transactions, Vol. 97, Pt. 1, pp. 497-504.

Takemitsu, N. 1990. An Analytical Study of the Standard k-ε Model. Transactions of the ASME, Vol. 112, pp. 192-198.

Timmons, M. B., L. D. Albright, R. B. Furry and K. E. Torrance. 1980. Experimental and Numerical Study of Air Movement in Slot-Ventilated Enclosures. ASHRAE Transactions, Vol. 86, Pt. 1, pp. 221-240.

Tsuchiya, T. 1976. Numerical Calculation of Room Air Movement - Isothermal Turbulent Two-Dimensional Case. Building Research Institute. No. 62.

Tsutsumi, J., T. Katayama, T. Hayashi, Q. Zhang and H. Yoshimizu. 1988. Numerical Simulation of Indoor Turbulent Air Flows Caused by Cross-Ventilation and its Model Experiments. 9th AIVC Conference, Gent, Belgium. pp. 141-156.

Vazquez, B., D. Samano and M. Yianneskis. 1991. The Effect of Air Inlet Location on the Ventilation of an Auditorium. Computational Fluid Dynamics for the Environmental and Building Services Engineer - Tool or Toy?, London: Mechanical Engineering Publications. pp. 56-66.

Wang, J. C. Y., Z. Jiang and F. Haghighat. 1991. Influence of Air Infiltration on Airflow in a Ventilated Isothermal Two-Zone Enclosure. Energy and Buildings, Vol. 17, pp. 43-54.

Weathers, J. W. 1992. A Study of Computational Fluid Dynamics Applied to Room Airflow. M. S. Thesis. Oklahoma State University.

Weathers, J. W. and J. D. Spitler. 1993. A Comparative Study of Room Airflow: Numerical Prediction Using Computational Fluid Dynamics and Full-Scale Experimental Measurements. ASHRAE Transactions, Vol. 99, Pt. 2, pp. 144-156.

Whittle, G. E. 1986. Computation of Air Movement and Convective Heat Transfer Within Buildings. International Journal of Ambient Energy, Vol. 7, No. 3, pp. 151-165.

Wilcox, D. C. 1993. Turbulence Modeling for CFD. La Canada, California: DCW Industries, Inc. pp. 460.

Williams, P. T., A. J. Baker and R. M. Kelso. 1994. Numerical Calculation of Room Air Motion - Part 3: Three-Dimensional CFD Simulation of a Full-Scale Room Air Experiment. ASHRAE Transactions, Vol. 100, Pt. 1.

Yamamoto, T., D. S. Ensor and L. E. Sparks. 1991. Two-Dimensional Turbulence Flow Model for a Personal Computer. IAQ '91 Healthy Buildings, Washington, D.C. pp. 175-178.

Yamazaki, K., M. Komatsu and M. Otsubo. 1987. Application of Numerical Simulation for Residential Room Air Conditioning. ASHRAE Transactions, Vol. 93, Pt. 1, pp. 210-225.

Yau, R. H. and G. E. Whittle. 1991. Air Flow Analysis for Large Spaces in an Airport Terminal Building: Computational Fluid Dynamics and Reduced-Scale Physical Model Tests. Computational Fluid Dynamics for the Environmental and Building Services Engineer - Tool or Toy?, London: Mechanical Engineering Publications. pp. 47-55.

Zhang, H., M. Reggio, J. Y. Trepanier and R. Camarero. 1993. Discrete Form of the GCL for Moving Meshes and its Implementation in CFD Schemes. Computers & Fluids, Vol. 22, No. 1, pp. 9-23.

Zhang, J. S., L. L. Christianson, G. J. Wu and G. L. Riskowski. 1992a. Detailed Measurements of Room Air Distribution for Evaluating Numerical Simulation Models. ASHRAE Transactions, Vol. 98, Pt. 1, pp. 58-65.

Zhang, J. S., G. J. Wu and L. L. Christianson. 1992b. Full-Scale Experimental Results on the Mean and Turbulent Behavior of Room Ventilation Flows. ASHRAE Transactions, Vol. 98, Pt. 2, pp. 307-318.

APPENDIX

Finite Difference Equations for U Velocity Components

$$U_{i,j,k}^{new} = U_{i,j,k}^{old} + \Delta t\left[\frac{P_{i,j,k} - P_{i+1,j,k}}{\Delta x_i} + g_x + VISX - FUX - FUY - FUZ\right]$$

The viscous flux term in expanded finite difference form is given below.

$$VISX = \nu\left[\left(\frac{U_{i+1,j,k} - U_{i,j,k}}{\Delta x_{ci+1}} - \frac{U_{i,j,k} - U_{i-1,j,k}}{\Delta x_{ci}}\right)\Big/\Delta x_i + \left(\frac{U_{i,j+1,k} - U_{i,j,k}}{\Delta y_j} - \frac{U_{i,j,k} - U_{i,j-1,k}}{\Delta y_{j-1}}\right)\Big/\Delta y_{cj} + \left(\frac{U_{i,j,k+1} - U_{i,j,k}}{\Delta z_k} - \frac{U_{i,j,k} - U_{i,j,k-1}}{\Delta z_{k-1}}\right)\Big/\Delta z_{ck}\right]$$

The convective flux terms are as follows.

$$FUX = \frac{1}{4}\left\{\left[(U_{i,j,k}+U_{i+1,j,k})^2 + \overline{\alpha}\ |U_{i,j,k}+U_{i+1,j,k}|*(U_{i,j,k}-U_{i+1,j,k})\right]/\Delta x_{ci+1} - \left[(U_{i-1,j,k}+U_{i,j,k})^2 + \overline{\alpha}\ |U_{i-1,j,k}+U_{i,j,k}|*(U_{i-1,j,k}-U_{i,j,k})\right]/\Delta x_{ci}\right\}$$

$$FUY = \frac{1}{4}\left\{\left[(V_{i,j,k}+V_{i+1,j,k})*(U_{i,j,k}+U_{i,j+1,k}) + \overline{\alpha}\,|V_{i,j,k}+V_{i+1,j,k}|*(U_{i,j,k}-U_{i,j+1,k})\right]/\Delta y_j - \left[(V_{i,j-1,k}+V_{i+1,j-1,k})*(U_{i,j-1,k}+U_{i,j,k}) + \overline{\alpha}\,|V_{i,j-1,k}+V_{i+1,j-1,k}|*(U_{i,j-1,k}-U_{i,j,k})\right]/\Delta y_{j-1}\right\}$$

$$FUZ = \frac{1}{4}\left\{\left[(W_{i,j,k}+W_{i+1,j,k})*(U_{i,j,k}+U_{i,j,k+1}) + \overline{\alpha}\ |W_{i,j,k}+W_{i+1,j,k}|*(U_{i,j,k}-U_{i,j,k+1})\right]/\Delta z_k - \left[(W_{i,j,k-1}+W_{i+1,j,k-1})*(U_{i,j,k-1}+U_{i,j,k}) + \overline{\alpha}\ |W_{i,j,k-1}+W_{i+1,j,k-1}|*(U_{i,j,k-1}-U_{i,j,k})\right]/\Delta z_{k-1}\right\}$$

Finite Difference Equations for V Velocity Components

$$V_{i,j,k}^{new} = V_{i,j,k}^{old} + \Delta t\left[\frac{P_{i,j,k} - P_{i,j+1,k}}{\Delta y_j} + g_y + VISY - FVX - FVY - FVZ\right]$$

The viscous flux term in expanded finite difference form is given below.

$$VISY = \nu\left[\left(\frac{V_{i+1,j,k} - V_{i,j,k}}{\Delta x_i} - \frac{V_{i,j,k} - V_{i-1,j,k}}{\Delta x_{i-1}}\right)\Big/\Delta x_{ci}\right.$$

$$+\left(\frac{V_{i,j+1,k} - V_{i,j,k}}{\Delta y_{cj+1}} - \frac{V_{i,j,k} - V_{i,j-1,k}}{\Delta y_{cj}}\right)\Big/\Delta y_j$$

$$\left.+\left(\frac{V_{i,j,k+1} - V_{i,j,k}}{\Delta z_k} - \frac{V_{i,j,k} - V_{i,j,k-1}}{\Delta z_{k-1}}\right)\Big/\Delta z_{ck}\right]$$

The convective flux terms are as follows.

$$FVX = \frac{1}{4}\left\{[(U_{i,j,k}+U_{i,j+1,k})*(V_{i,j,k}+V_{i+1,j,k}) + \overline{\alpha}\ |U_{i,j,k}+U_{i,j+1,k}|*(V_{i,j,k}-V_{i+1,j,k})]/\Delta x_i\right.$$

$$\left.-[(U_{i-1,j,k}+U_{i-1,j+1,k})*(V_{i-1,j,k}+V_{i,j,k}) + \overline{\alpha}\ |U_{i-1,j,k}+U_{i-1,j+1,k}|*(V_{i-1,j,k}-V_{i,j,k})]/\Delta x_{i-1}\right\}$$

$$FVY = \frac{1}{4}\left\{[(V_{i,j,k}+V_{i,j+1,k})^2 + \overline{\alpha}\ |V_{i,j,k}+V_{i,j+1,k}|*(V_{i,j,k}-V_{i,j+1,k})]/\Delta y_{cj+1}\right.$$

$$\left.-[(V_{i,j-1,k}+V_{i,j,k})^2 + \overline{\alpha}\ |V_{i,j-1,k}+V_{i,j,k}|*(V_{i,j-1,k}-V_{i,j,k})]/\Delta y_{cj}\right\}$$

$$FVZ = \frac{1}{4}\left\{[(W_{i,j,k}+W_{i,j+1,k})*(V_{i,j,k}+V_{i,j,k+1}) + \overline{\alpha}\ |W_{i,j,k}+W_{i,j+1,k}|*(V_{i,j,k}-V_{i,j,k+1})]/\Delta z_k\right.$$

$$\left.-[(W_{i,j,k-1}+W_{i,j+1,k-1})*(V_{i,j,k-1}+V_{i,j,k}) + \overline{\alpha}\ |W_{i,j,k-1}+W_{i,j+1,k-1}|*(V_{i,j,k-1}-V_{i,j,k})]/\Delta z_{k-1}\right\}$$

Finite Difference Equations for W Velocity Components

$$W_{i,j,k}^{new} = W_{i,j,k}^{old} + \Delta t\left[\frac{P_{i,j,k} - P_{i,j,k+1}}{\Delta z_k} + g_z + VISZ - FWX - FWY - FWZ\right]$$

The viscous flux term in expanded finite difference form is given below.

$$VISZ = \nu\left[\left(\frac{W_{i+1,j,k} - W_{i,j,k}}{\Delta x_i} - \frac{W_{i,j,k} - W_{i-1,j,k}}{\Delta x_{i-1}}\right)\Big/\Delta x_{ci}\right.$$

$$+\left(\frac{W_{i,j+1,k} - W_{i,j,k}}{\Delta y_j} - \frac{W_{i,j,k} - W_{i,j-1,k}}{\Delta y_{j-1}}\right)\Big/\Delta y_{cj}$$

$$\left.+\left(\frac{W_{i,j,k+1} - W_{i,j,k}}{\Delta z_{ck+1}} - \frac{W_{i,j,k} - W_{i,j,k-1}}{\Delta z_{ck}}\right)\Big/\Delta z_k\right]$$

The convective flux terms are as follows.

$$FWX = \frac{1}{4}\left\{[(U_{i,j,k}+U_{i,j,k+1})*(W_{i,j,k}+W_{i+1,j,k}) + \overline{\alpha}\ |U_{i,j,k}+U_{i,j,k+1}|*(W_{i,j,k}-W_{i+1,j,k})]/\Delta x_i\right.$$

$$\left.-[(U_{i-1,j,k}+U_{i-1,j,k+1})*(W_{i-1,j,k}+W_{i,j,k}) + \overline{\alpha}\ |U_{i-1,j,k}+U_{i-1,j,k+1}|*(W_{i-1,j,k}-W_{i,j,k})]/\Delta x_{i-1}\right\}$$

$$FWY = \frac{1}{4}\left\{[(W_{i,j,k}+W_{i,j+1,k})*(V_{i,j,k}+V_{i,j,k+1}) + \overline{\alpha}\ |V_{i,j,k}+V_{i,j,k+1}|*(W_{i,j,k}-W_{i,j+1,k})]/\Delta y_j\right.$$

$$\left.-[(V_{i,j-1,k}+V_{i,j-1,k+1})*(W_{i,j-1,k}+W_{i,j,k}) + \overline{\alpha}\ |V_{i,j-1,k}+V_{i,j-1,k+1}|*(W_{i,j-1,k}-W_{i,j,k})]/\Delta y_{j-1}\right\}$$

$$FWZ = \frac{1}{4}\left\{[(W_{i,j,k}+W_{i,j,k+1})^2 + \overline{\alpha}\ |W_{i,j,k}+W_{i,j,k+1}|*(W_{i,j,k}-W_{i,j,k+1})]/\Delta z_{ck+1}\right.$$

$$\left.-[(W_{i,j,k-1}+W_{i,j,k})^2 + \overline{\alpha}\ |W_{i,j,k-1}+W_{i,j,k}|*(W_{i,j,k-1}-W_{i,j,k})]/\Delta z_{ck}\right\}$$

Finite Difference Turbulent Velocity Equations

$$U_{i,j,k}^{new} = U_{i,j,k}^{old} + \Delta t\left[\frac{P_{i,j,k} - P_{i+1,j,k}}{\Delta x_i} + g_x + GAMMAX - FUX - FUY - FUZ\right]$$

$$\Gamma_x = \nu_t\left[2\frac{\partial^2 U}{\partial x^2} + \frac{\partial^2 U}{\partial y^2} + \frac{\partial^2 U}{\partial z^2} + \frac{\partial^2 V}{\partial x \partial y} + \frac{\partial^2 W}{\partial x \partial z}\right] + 2\frac{\partial \nu_t}{\partial x}\left[\frac{\partial U}{\partial x}\right]$$

$$+ \frac{\partial \nu_t}{\partial y}\left[\frac{\partial U}{\partial y} + \frac{\partial V}{\partial x}\right] + \frac{\partial \nu_t}{\partial z}\left[\frac{\partial U}{\partial z} + \frac{\partial W}{\partial x}\right] - \frac{2}{3}\frac{\partial k}{\partial x}$$

$$V_{i,j,k}^{new} = V_{i,j,k}^{old} + \Delta t\left[\frac{P_{i,j,k} - P_{i,j+1,k}}{\Delta y_j} + g_y + GAMMAY - FVX - FVY - FVZ\right]$$

$$\Gamma_y = \nu_t\left[2\frac{\partial^2 V}{\partial y^2} + \frac{\partial^2 V}{\partial x^2} + \frac{\partial^2 V}{\partial z^2} + \frac{\partial^2 U}{\partial x \partial y} + \frac{\partial^2 W}{\partial z \partial y}\right] + 2\frac{\partial \nu_t}{\partial y}\left[\frac{\partial V}{\partial y}\right]$$

$$+ \frac{\partial \nu_t}{\partial x}\left[\frac{\partial V}{\partial x} + \frac{\partial U}{\partial y}\right] + \frac{\partial \nu_t}{\partial z}\left[\frac{\partial V}{\partial z} + \frac{\partial W}{\partial y}\right] - \frac{2}{3}\frac{\partial k}{\partial y}$$

$$W_{i,j,k}^{new} = W_{i,j,k}^{old} + \Delta t\left[\frac{P_{i,j,k} - P_{i,j,k+1}}{\Delta z_k} + g_z + GAMMAZ - FWX - FWY - FWZ\right]$$

$$\Gamma_z = \nu_t\left[2\frac{\partial^2 W}{\partial z^2} + \frac{\partial^2 W}{\partial x^2} + \frac{\partial^2 W}{\partial z^2} + \frac{\partial^2 U}{\partial x \partial z} + \frac{\partial^2 V}{\partial z \partial y}\right] + 2\frac{\partial \nu_t}{\partial z}\left[\frac{\partial W}{\partial z}\right]$$

$$+ \frac{\partial \nu_t}{\partial x}\left[\frac{\partial W}{\partial x} + \frac{\partial U}{\partial z}\right] + \frac{\partial \nu_t}{\partial y}\left[\frac{\partial V}{\partial z} + \frac{\partial W}{\partial y}\right] - \frac{2}{3}\frac{\partial k}{\partial z}$$

Finite Difference Mixture Fraction Equations

$$S_{i,j,k}^{new} = S_{i,j,k}^{old} + \Delta t\left[\, VISS - FSX - FSY - FSZ \,\right]$$

$$VISS = \alpha \left[\left(\frac{S_{i+1,j,k} - S_{i,j,k}}{\Delta x_i} - \frac{S_{i,j,k} - S_{i-1,j,k}}{\Delta x_{i-1}} \right) \Big/ \Delta x_{ci} \right.$$

$$+ \left(\frac{S_{i,j+1,k} - S_{i,j,k}}{\Delta y_j} - \frac{S_{i,j,k} - S_{i,j-1,k}}{\Delta y_{j-1}} \right) \Big/ \Delta y_{cj}$$

$$\left. + \left(\frac{S_{i,j,k+1} - S_{i,j,k}}{\Delta z_k} - \frac{S_{i,j,k} - S_{i,j,k-1}}{\Delta z_{k-1}} \right) \Big/ \Delta z_{ck} \right]$$

$$FSX = \frac{1}{2}\left\{ [U_{i,j,k}(S_{i,j,k}+S_{i+1,j,k}) + \overline{\alpha}\ |U_{i,j,k}|*(S_{i,j,k}-S_{i+1,j,k})]/\Delta x_i \right.$$

$$\left. -[(U_{i-1,j,k}(S_{i-1,j,k}+S_{i,j,k}) + \overline{\alpha}\ |U_{i-1,j,k}|*(S_{i-1,j,k}-S_{i,j,k})]/\Delta x_{i-1} \right\}$$

$$FSY = \frac{1}{2}\left\{ [V_{i,j,k}(S_{i,j,k}+S_{i,j+1,k}) + \overline{\alpha}\ |V_{i,j,k}|*(S_{i,j,k}-S_{i,j+1,k})]/\Delta y_j \right.$$

$$\left. -[(V_{i,j-1,k}(S_{i,j-1,k}+S_{i,j,k}) + \overline{\alpha}\ |V_{i,j-1,k}|*(S_{i,j-1,k}-S_{i,j,k})]/\Delta y_{j-1} \right\}$$

$$FSZ = \frac{1}{2}\left\{ [W_{i,j,k}(S_{i,j,k}+S_{i,j,k+1}) + \overline{\alpha}\ |W_{i,j,k}|*(S_{i,j,k}-S_{i,j,k+1})]/\Delta z_k \right.$$

$$\left. -[(W_{i,j,k-1}(S_{i,j,k-1}+S_{i,j,k}) + \overline{\alpha}\ |W_{i,j,k-1}|*(S_{i,j,k-1}-S_{i,j,k})]/\Delta z_{k-1} \right\}$$

k and ε Finite Difference Convective Flux Equations

$$FKX = \frac{1}{2}\left\{\left[U_{i,j,k}(k_{i,j,k}+k_{i+1,j,k}) + \overline{\alpha}\ |U_{i,j,k}|*(k_{i,j,k}-k_{i+1,j,k})\right]/\Delta x_i \right.$$
$$\left. -\left[(U_{i-1,j,k}(k_{i-1,j,k}+k_{i,j,k}) + \overline{\alpha}\ |U_{i-1,j,k}|*(k_{i-1,j,k}-k_{i,j,k})\right]/\Delta x_{i-1}\right\}$$

$$FKY = \frac{1}{2}\left\{\left[V_{i,j,k}(k_{i,j,k}+k_{i,j+1,k}) + \overline{\alpha}\ |V_{i,j,k}|*(k_{i,j,k}-k_{i,j+1,k})\right]/\Delta y_j \right.$$
$$\left. -\left[(V_{i,j-1,k}(k_{i,j-1,k}+k_{i,j,k}) + \overline{\alpha}\ |V_{i,j-1,k}|*(k_{i,j-1,k}-k_{i,j,k})\right]/\Delta y_{j-1}\right\}$$

$$FKZ = \frac{1}{2}\left\{\left[W_{i,j,k}(k_{i,j,k}+k_{i,j,k+1}) + \overline{\alpha}\ |W_{i,j,k}|*(k_{i,j,k}-k_{i,j,k+1})\right]/\Delta z_k \right.$$
$$\left. -\left[(W_{i,j,k-1}(k_{i,j,k-1}+k_{i,j,k}) + \overline{\alpha}\ |W_{i,j,k-1}|*(k_{i,j,k-1}-k_{i,j,k})\right]/\Delta z_{k-1}\right\}$$

$$FEX = \frac{1}{2}\left\{\left[U_{i,j,k}(\varepsilon_{i,j,k}+\varepsilon_{i+1,j,k}) + \overline{\alpha}\ |U_{i,j,k}|*(\varepsilon_{i,j,k}-\varepsilon_{i+1,j,k})\right]/\Delta x_i \right.$$
$$\left. -\left[(U_{i-1,j,k}(\varepsilon_{i-1,j,k}+\varepsilon_{i,j,k}) + \overline{\alpha}\ |U_{i-1,j,k}|*(\varepsilon_{i-1,j,k}-\varepsilon_{i,j,k})\right]/\Delta x_{i-1}\right\}$$

$$FEY = \frac{1}{2}\left\{\left[V_{i,j,k}(\varepsilon_{i,j,k}+\varepsilon_{i,j+1,k}) + \overline{\alpha}\ |V_{i,j,k}|*(\varepsilon_{i,j,k}-\varepsilon_{i,j+1,k})\right]/\Delta y_j \right.$$
$$\left. -\left[(V_{i,j-1,k}(\varepsilon_{i,j-1,k}+\varepsilon_{i,j,k}) + \overline{\alpha}\ |V_{i,j-1,k}|*(\varepsilon_{i,j-1,k}-\varepsilon_{i,j,k})\right]/\Delta y_{j-1}\right\}$$

$$FEZ = \frac{1}{2}\left\{\left[W_{i,j,k}(\varepsilon_{i,j,k}+\varepsilon_{i,j,k+1}) + \overline{\alpha}\ |W_{i,j,k}|*(\varepsilon_{i,j,k}-\varepsilon_{i,j,k+1})\right]/\Delta z_k \right.$$
$$\left. -\left[(W_{i,j,k-1}(\varepsilon_{i,j,k-1}+\varepsilon_{i,j,k}) + \overline{\alpha}\ |W_{i,j,k-1}|*(\varepsilon_{i,j,k-1}-\varepsilon_{i,j,k})\right]/\Delta z_{k-1}\right\}$$

Finite Difference Equations for Theta Function and Pi

$$\Theta(k) = \frac{\nu_t}{\sigma_k}\left(\frac{\partial^2 k}{\partial x^2} + \frac{\partial^2 k}{\partial y^2} + \frac{\partial^2 k}{\partial z^2}\right) + \frac{1}{\sigma_k}\left(\frac{\partial \nu_t \partial k}{\partial x \partial x} + \frac{\partial \nu_t \partial k}{\partial y \partial y} + \frac{\partial \nu_t \partial k}{\partial z \partial z}\right)$$

$$\Theta(\varepsilon) = \frac{\nu_t}{\sigma_\varepsilon}\left(\frac{\partial^2 \varepsilon}{\partial x^2} + \frac{\partial^2 \varepsilon}{\partial y^2} + \frac{\partial^2 \varepsilon}{\partial z^2}\right) + \frac{1}{\sigma_\varepsilon}\left(\frac{\partial \nu_t \partial \varepsilon}{\partial x \partial x} + \frac{\partial \nu_t \partial \varepsilon}{\partial y \partial y} + \frac{\partial \nu_t \partial \varepsilon}{\partial z \partial z}\right)$$

$$\begin{aligned}\Pi = \quad & 2\left(\frac{\partial U}{\partial x}\right)^2 + \frac{\partial U}{\partial y}\left(\frac{\partial U}{\partial y} + \frac{\partial V}{\partial x}\right) + \frac{\partial U}{\partial z}\left(\frac{\partial U}{\partial z} + \frac{\partial W}{\partial x}\right) \\ & + 2\left(\frac{\partial V}{\partial y}\right)^2 + \frac{\partial V}{\partial x}\left(\frac{\partial V}{\partial x} + \frac{\partial U}{\partial y}\right) + \frac{\partial V}{\partial z}\left(\frac{\partial V}{\partial z} + \frac{\partial W}{\partial y}\right) \\ & + 2\left(\frac{\partial W}{\partial z}\right)^2 + \frac{\partial W}{\partial x}\left(\frac{\partial W}{\partial x} + \frac{\partial U}{\partial z}\right) + \frac{\partial W}{\partial y}\left(\frac{\partial W}{\partial y} + \frac{\partial V}{\partial z}\right)\end{aligned}$$

VITA

Michael R. Ramey

Candidate for the Degree of

Master of Science

Thesis: APPLICATION OF COMPUTATIONAL FLUID DYNAMICS TO INDOOR ROOM AIRFLOW

Major Field: Mechanical Engineering

Biographical:

Personal Data: Born in Troy, Ohio, February 24, 1969, the son of Eddie R. and Judith R. Ramey. Married Lisa K. Williams, September 24, 1994.

Education: Graduated from Granite City Senior High School, Granite City, Illinois, in June, 1987; received Bachelor of Science degree in Mechanical Engineering from Oklahoma Christian University of Science and Arts, Oklahoma City, Oklahoma, in December, 1991; completed requirements for the Master of Science degree at Oklahoma State University in December, 1994.

Professional Experience: Employed as a draftsman during the summers of 1989 and 1990. Employed as an Engineering Intern at Texas Instruments during the summers of 1991 & 1992. Teaching Assistant, Oklahoma State University, August 1992 to December 1993.